UNIVERSITÀ DEGLI STUDI DI MILANO

Physics Department

PhD School in Physics, Astrophysics and Applied Physics

XXXIV Cycle

Optical characterization of mineral dust content in snow and ice cores with digital in-line holography

Scientific Disciplinary Sector: FIS/03

Supervisor: Professor Marco A. C. Potenza

Co-supervisor: Professor Barbara Delmonte

Director of the School: Professor Matteo Paris

Candidate:

Claudia Ravasio

A. Y. 2021/2022

Febbraio 2022, Betty

Contents

List of Figures

List of Tables

Introduction

Atmospheric aerosol is an active component of the climate system and is known to impact the Earth's radiative energy balance by interacting with both solar and terrestrial radiation (Stocker, 2014). Particles deposited on mid-latitude glaciers, polar snow, and sea ice affects the albedo, altering the ability of such surfaces to scatter light, and increasing significantly the absorption (Hansen and Nazarenko (2004), Mauro et al. (2021)). Moreover, mineral dust acts as cloud condensation nuclei affecting the formation of clouds and the occurring of precipitation (Haywood and Boucher, 2000, Mahowald et al., 2009). Not only dust plays an important role in the climate system, but it is also strongly affected by anthropogenic activities: both deforestation and agriculture increase the area of bare soil that can act as a source of dust storms (McTainsh et al., 1990). The quantitative estimation of these impacts has considerable uncertainty in climate models, so further research is needed for better predicting future climate change. The physics of dust entrainment, transport, and deposition is complex, and model parameters are hard to estimate. Moreover, to date, there is a critical lack of calibrated samples. In this respect, models could benefit from systematic data collection.
Ice cores provide one of the most important proxies for paleoclimate research; records from the past reveal dust deposition under different climates (Wolff et al., 2010). They store air bubbles, sea salts, volcanic ash, soot, dust, sands, and other pollutants, characterized by different sizes and morphologies that define the deposition times and the susceptibility to long-range transport. The effect of mineral dust on the atmospheric system is tightly related to their optical properties. These depend on the morphological and chemical properties of dust; indeed deviations from ideal spheres have an appreciable impact on the radiative forcing component from dust. For example, plate particles cause a lower extinction of the incoming light compared to spheres for any given cross-sectional area (Dubovik et al., 2002). Deriving information about dust particle shapes is critical to determine the intrinsic optical properties of dust, which are of environmental relevance to improve the

modelization of their radiative properties and reduce the associated uncertainties (Ellis et al., 2016). State-of-the-art models acknowledge mineral dust, as well as the need for a refined description of aerosol morphologies, as an essential component of the climate system. Because of the extremely low number of particles in ice core samples, an analysis on a particle-by-particle is preferable when investigating grains already deposited, enhancing the use of the optical techniques, as a versatile and non-invasive probe.

In the present work, we focus on the study of new optical methods for a single-particle characterization of mineral dust and micrometric particles, focusing on the analysis of airborne particles in meltwater samples from the cryosphere, like Alpine and Antarctic snow and ice core samples. The aim is to obtain information on the effects of the particle shape on the optical parameters of interest for the radiative transfer of sunlight through the atmosphere.

Methods for extracting quantitative information from microscopy images typically rely on heuristic models intended to emulate the perception of vision. These identify regions of contrast as features of interest and employ various image analysis techniques to estimate the position, shape, and cross-sectional area of objects in the field of view (Jähne, 1995). However, recently the field of quantitative microscopy has advanced with the introduction of techniques that model the physics of image formation to extract quantitative information from microscopic images (Bierbaum et al., 2017, Lee and Grier, 2007). With digital microscopic holography, it is possible to analyze water suspensions of micrometric mineral dust particles polydisperse in size and simultaneously provide information about the morphological and optical properties of each measured particle. In particular, this thesis describes advances in holographic particle characterization, obtaining the three-dimensional position, cross-sectional area, and extinction cross-section of particles. Holography, as an optical method, is versatile, fast, and non-invasive. The advantage of holography with respect to traditional imaging relies on the capability of recovering images and optical information from objects within volumes much thicker than the limited depth of focus of traditional imaging. Moreover, it naturally deals with sample polydispersity and under strong dilution, hence it is particularly suited for polar ice cores and snow samples. As a particle-by-particle optical technique contributes significantly to an all-around characterization of mineral dust by giving direct access to their optical properties. Finally, it is suitable for continuous flow analysis systems typically used in ice core characterization. This work develops a formal foundation for the technique explaining the theory of image formation in holographic microscopy by reporting a suite of validation measurements with calibrated particles, which set the limits of precision and accuracy that can be obtained with it, and providing

an overview of the experimental results from Antarctic and Alpine ice core.

Thesis aim and overview

This thesis describes two main scientific results. First, we have developed a method for performing rapid and accurate imaging of particles using a technique called digital holographic microscopy. Secondly, we have applied for the first time this technique to perform an optical characterization of meltwater samples from the cryosphere, with a dedicated apparatus and flow system designed for this purpose.

The first part is devoted to introducing the scientific framework of mineral dust and their relevance. We begin by giving an overview of their relevant radiative effects and morphological characteristics in Chapter 1. Next, we explain the importance of studying mineral dust embedded in ice core in Section 1.3. The optical properties of mineral dust and the description of scattering theory are given in Section 1.4. Chapter 2 provides an extensive theoretical and practical introduction to holographic particle characterization. The chapter starts with a brief historically-driven overview of digital holography, followed by the features of the holographic patterns from different morphological particles in Section 2.2. In Section 2.3, 2.5 and 2.6 the theoretical mainstay for the experimental techniques used for this work is explained exhaustively, in particular the object reconstruction method and the optical characteristics embedded in a holographic pattern.

The second part illustrates the experimental setup, procedures, and analysis. We describe the details of our implementation of digital holography and image analysis for detection, localization, reconstruction, and characterization in Chapter 3, Sect. 3.1. From the detection of an holographic feature, we can obtain the three-dimensional position and the estimation of the particle size, cross-sectional area, aspect ratio, and extinction cross-section. Follows a series of experimental studies that describe the effectiveness of digital holography for characterizing compact non-spherical particles as mineral dust. The samples chosen for the analysis are mineral dust from Antarctic snowpits in Sect. 3.2. Here the effect of shape on the extinction cross-section of micrometric particles is highlighted. We found similar results in Alpine snow cores from Router Glacier, and we report a recent three-year historical series from 2015 to 2019 in Subsect. 3.2.1. In Sect. 3.3 we turn to mineral dust samples in deep ice cores, sampling in a way to describe the Holocene age of the West Antarctic Ice Sheet.
We conclude in Sect. 3.4 with a custom-made implementation of the technique over a bright-field microscope, by providing the few and simple modifications needed,

and the preliminary experimental analysis with polystyrene beads of different sizes. We summarize our results and discuss the outlook of digital holography in the Conclusion. In Appendix A we provide the explanations and the results of the calibration test both for the holographic technique and the reconstruction algorithm through the use of calibrated polystyrene beads. In Appendix A.1 we show an example of absorbing particles from carbon smoke soot aggregates, whereby we can differentiate from non-absorbing ones. Finally, in Appendix B we describe the Lorents-Mie models based on single sphere scattering solutions, which has been vastly cited in the work.

Chapter 1

Mineral dust

The atmosphere is a multiphase system consisting of both gas molecules and liquid or solid phase aerosol particles (Seinfeld and Pandis, 2016). Among aerosols, such as the soot from natural fires and sulfates from the industrial exhaust, or ash from volcanic eruptions and sea salt from the marine ecosystem, mineral dust is the most important aerosol by (dry) mass (Fig. 1.1, Prospero et al. (2002), Bond et al. (2013)). Airborne dust is released into the atmosphere by wind erosion

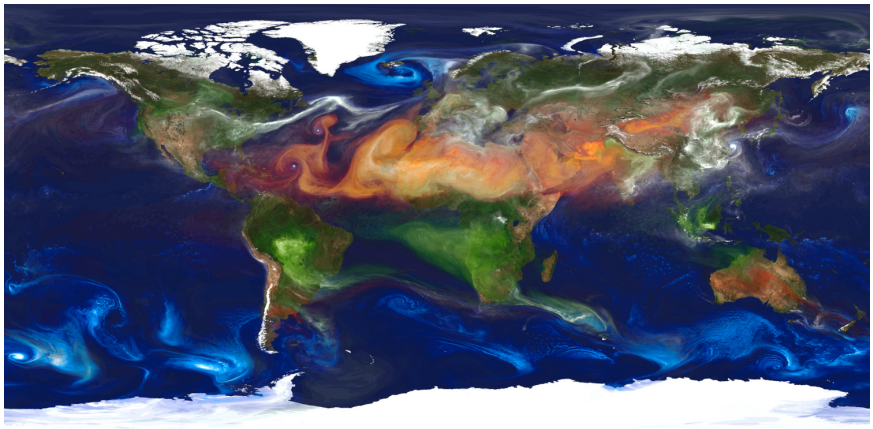

Figure 1.1: NASA's GEOS-5 simulation. The four main aerosols are color-coded: mineral dust from deserts (red), sea salt from spray (blue), soot and smoke from fires (green), and sulphate particles from fossil fuel combustion and volcanoes (white). Credit: `http://geos5.org`.

processes, saltation, and sandblasting, at a rate of $1 - 3 \cdot 10^3$ kg/a (Field et al., 2010, Shao, 2001), from soils in arid and semi-arid regions, with sporadic contributions from volcanoes and from extraterrestrial sources. It may be present as fine-grained particles or in a dissolved form within water droplets or ice crystals. They can be transported thousands of kilometers from their source region, thereby

affecting weather and climate, ecosystem productivity, the hydrological cycle, and various other components of the Earth system. For example, they contribute to the deterioration of air quality and visibility, which can affect air traffic and road transportation, and have a critical impact on agriculture due to the aerial erosion of soils (McTainsh et al., 1990). Similarly, the wind is responsible for the release into the atmosphere of ions, phosphorus, and other corpuscles found in soil and seawater such as microalgae (Marks, 1987, Tesson et al., 2016). They become a source of micronutrients for continental and maritime ecosystems, regions of dust settlement, by fertilizing and impacting the biogeochemical cycles of oceans and seas (Babin and Stramski, 2002, Mahowald et al., 2009, Martínez-Garcia et al., 2011). Dust can also serve as a reaction surface for gases in the atmosphere and can moderate photochemical processes (Prospero et al., 2002). Moreover, their interaction with solar and terrestrial radiation directly by absorption and scattering of radiation and indirectly by influencing the life cycle of clouds makes them an important term appearing in the radiative budget of the Earth (Textor et al., 2006, Tegen and Schepanski, 2009, Booth et al., 2012, Ito and Wagai, 2017). This can result either in positive or negative feedback depending on the surface reflectance of the land or water underneath (Haywood and Boucher, 2000). Finally, mineral dust particles enhance melting in glaciers and snowpacks when deposited on the cryosphere (Kok et al., 2012, Mauro et al., 2019). However, the role of dust in climate change still represents an important source of uncertainty in climate models and many open questions remain (Claquin et al., 1998, Stocker, 2014).

All the aforementioned impacts are tightly related both to mineral dust optical properties, and to their chemical and mineralogical composition, morphology, and shape. In the present work, our focus is on the interaction with solar and terrestrial radiation which impacts the Earth's radiative energy balance and the local temperature in the atmosphere.

1.1 Source and composition of mineral dust

Mineral dust from both natural and anthropogenic sources constitutes the second most abundant aerosol after sea salt and has the highest average optical thickness. Wind erosion may take place on soils that are unprotected by vegetation and sufficiently dry. Major sources are desert regions of Northern Africa and the Middle East, Australia, and parts of Southern Asia. Estimates of annual dust emissions range from 800 to 2000 Tg/y (Zender et al., 2004), which exceeds 50% of aerosol total dry mass (Miller et al., 2006), a large portion of which ($\sim 60\%$) originates from northern Africa (low-latitude deserts). Interestingly, the average dust

load during the Last Glacial Maximum used to be much higher than the present one. During a dust storm, particles are moved horizontally and trigger the basic mechanisms which underlie the particle emission into the atmosphere and the dust generation: the collisions of saltating (fine) particles with the surface (Shao et al., 1993), the sandblasting (Lawrence and Neff, 2009), and the suspension. The efficiency of such processes and the size distribution of the resulting products depend on the mineralogy of the soil as well as on its tendency to liberate smaller particles. The suspension involves the long-range transport—which makes seemingly regional sources grow in importance and have tangible effects on a global scale (Balkanski et al., 2007)—by advection and atmospheric circulation of $\sim 1\%$ of the total mass. Travel distance is related to atmospheric lifetime, which in turn depends on the size of the particle and ranges between one day and one week approximately. Close to the major dust source regions deflation includes all size ranges up to coarse silt and fine sand (Rea and Hovan, 1995), however, only clays and very fine silt are involved in long-range transport (Schulz et al., 1998, Moosmüller et al., 2012)). During transport, they are exposed to removal processes by wet (related to precipitation) and dry (sedimentation or impaction) deposition.

Most mineral particles that compose the dust fraction are dominated by (alumino) silicates such as quartz, plagioclase, feldspar, salts, volcanic materials, and clay minerals with varying amounts of carbonates, sulfates, and iron-bearing minerals (Paleari et al., 2019, Tsoar and Pye, 1987). Mineral dust aerosol exhibits the largest size distribution variability among aerosols from a few nanometres to several tens of microns (Mahowald et al., 2014). In central East Antarctica, where dust is transported from Southern Hemisphere continents and the mean transit time is in the order of $3 - 4$ weeks (Petit and Delmonte, 2009), the modal value of the volume (mass) dust size distribution is around 2 µm, with small variations mainly related to the altitude and type of transport, while the modal density is 2.5 g/cm^3 (Delmonte et al., 2017). Generally, particles are known to follow a log-normal distribution, but actually, an "average" mineral size is an oversimplified parameter due to the morphological complexity of dust, which shows a predominant non-spherical shape and an internally mixed composition. In addition, the composition of aerosol may evolve rapidly over time, altered by chemical reactions during transport: dust can collect many smaller constituents and acquire correspondingly diverse scattering and absorption cross-sections (Pöschl, 2005). Moreover, deviations from ideal spheres have an appreciable impact on the radiative forcing from aerosols (Dubovik et al., 2006) and on aerosol optical depth (Potenza et al., 2016, Mariani et al., 2017). Therefore, characterizing the optical properties of mineral dust—and aerosol particles in general—can be challenging since they are affected by morphology, impurities, and coatings (Ellis et al., 2016).

1.2 Radiative effects of mineral dust

Atmospheric aerosols influence global climate both (1) directly, by changing the radiative properties of the atmosphere through scattering and absorption of solar (shortwave) and terrestrial (longwave) radiation, and (2) indirectly, by impacting on cloud formation and properties (Tegen and Lacis, 1996, Carslaw et al., 2010). Generally, an increase of dust results in an increase in solar radiation scattered back to space, partially offset by dust absorption. This can result in either positive or negative feedback depending strongly on the underlying surface: the highly scattering dust present over an ocean will have more impact on radiation balance than that over a desert surface. Conversely, in the long-wave part of the spectrum, dust can absorb the infrared terrestrial radiation and re-emit this radiation in all directions. Moreover, aerosol particles affect the hydro-geological cycle by serving as condensation nuclei in clouds (CCN) or ice nuclei (IN) (Stocker et al., 2013, Kärcher et al., 2007), on which cloud droplets and ice particles can form. In the presence of more aerosol particles, clouds of liquid water droplets tend to have higher droplet concentrations, but a decrease in their sizes, which causes these clouds to reflect more solar radiation. This is an example of how aerosol particles affect the microphysical properties of clouds—such as their lifetime, vertical extent, and precipitation efficiency (Lohmann and Feichter, 2005). In turn, clouds interact with light to the extent of their optical thickness, albedo, and lifetime, yielding either a cooling or warming effect in the short-wave and long-wave range respectively (Ebert and Curry, 1992, Haywood and Boucher, 2000). Aerosol composition, size, shape, surface, and physical-chemical and optical properties are continuously modified in the atmosphere by the mixing of aerosol particles and their aging through interactions with clouds.

In general, the feedback due to aerosol has been found to contribute to the temperature increase in the Arctic regions, which are experiencing a trend twice as fast as the rest of the globe, up to $\sim 1.5\,^{\circ}\mathrm{C}$ in the Arctic (Ferrero et al. (2019), Kylling et al. (2018)). Moreover, while dielectric particles have mostly a cooling effect, strongly absorbing particles, as anthropogenic aerosol and pollutants, have the potential to counteract this contribution (Stocker et al., 2013, Ghan and Zaveri, 2007). Indeed, because of its extraordinary absorption properties (Kahnert et al., 2012, Vecchi et al., 2014, Massabò et al., 2015), the contribution of black carbon direct radiative forcing is calculated to be about 70% of that of CO_2 (Chung and Seinfeld, 2005, Stocker, 2014). As thoroughly discussed in the 2013 Intergovernmental Panel on Climate Change (IPCC), the direct and indirect impact of mineral dust and other types of aerosols on the energy balance of the Earth system is, to date, far from being well characterized, mostly because of the large uncertainties affecting current estimations. Aerosols remain one of the greatest sources of uncertainty in

the interpretation and projection of past and future climate change on a synoptic scale. Moreover, because of their short lifetime, the abundance of aerosols—and their climate effects—suffer from a large spatial and temporal variability (Prospero et al., 2002, Kaufman and Koren, 2006). As the first step to understanding and quantifying the impact of dust on weather and climate, detailed knowledge of the optical properties of mineral dust is needed to clarify the mechanisms of aerosol radiative forcing. Besides the underlying environment, to model the radiative balance we must be able to describe the optical properties as a function of wavelength (for example, the extinction coefficient, the single-scattering albedo, and the phase function)—these are dependent on the size, shape, complex refractive index, composition of the dust, and the effective scattering cross-section, that are in turn dependent on the dust source and transport processes (Dubovik et al., 2002). One of the main reasons for the uncertainties affecting the impact of aerosols stems from the spherical shape approximation in the state-of-the-art numerical climate models (Potenza et al., 2016, Huang et al., 2020), whereby they would benefit from more accurate modeling of the aerosol components. Oversimplified composition and physical parameters in radiative modeling will lead to inaccurate or even erroneous results. Having detailed and reliable information available about the optical properties of particles suspended in the atmosphere is therefore essential.

1.3 Ice core archives of mineral dust

For the purpose of this work, we focus our attention on retrieving from ice cores the airborne particles transported and subsequently deposited on the surface of glaciers, and in time brought deeper, layer after layer, far from sources of pollution and contamination (Alloway et al., 2007, Wolff et al., 2010). The interest in ice cores arises from the fact they provide one of the most important proxies for paleoclimate research. They host a footprint of the aerosol content of the atmosphere of the past that would otherwise be lost—air bubbles, dust, sea salts, volcanic ash, soot, and other pollutants—that can end up trapped in glacial ice for thousands of years, as a library that stores in chronological order the story about how our planet's climate and atmosphere evolved (Delmonte et al., 2017, Lambert et al., 2012). A remarkable variety of sources and mineralogical compositions involve the particles that can be found in any glacier. Two Scanning Electron Microscope images of a set of mineral dust particles found in an Antarctic ice core is shown in Figure 1.2. Deep ice core drilling of polar ice caps can be up to 4 km long and have produced climate records covering the past 800 ky (thousands of years) allowing for accurate dating of samples and retrieving of high-resolution paleoclimate records over up to geologic time spans (Ruth et al., 2008, Rasmussen et al., 2014, Maffezzoli et al., 2017,

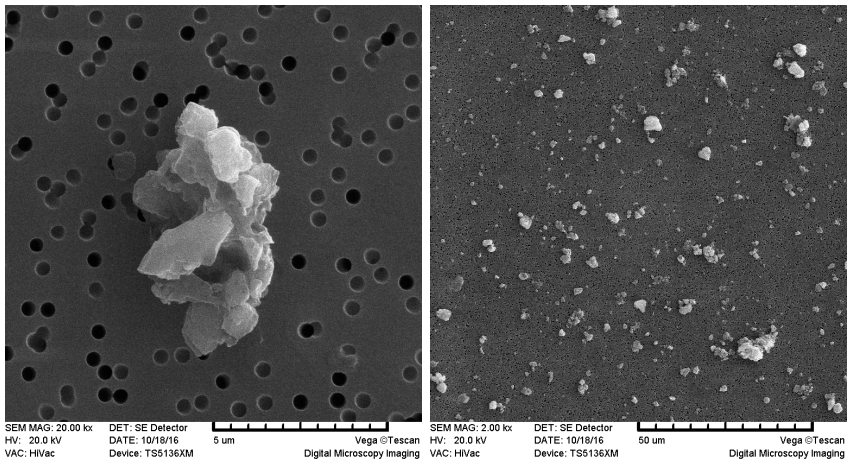

*Figure 1.2: Scanning Electron Microscope images of mineral dust particles from Dome C, Antarctica with different bar-scale (*5 µm *on the left,* 50 µm *on the right). Shape and size variability is well visible, moreover, some particles result from in-situ aggregation of smaller grains. The images were acquired by Dr. Delmonte (University of Milano-Bicocca) with a Scanning Electron Microscope at the EuroCold laboratory at the University of Milano-Bicocca.*

Potenza et al., 2017, Bertler et al., 2018). Provenance studies of aeolian dust can be based on particle mineralogy and isotopic composition. For example, strontium and neodymium isotopic fingerprinting identify the East Asian and Patagonian deserts respectively as the most probable source areas for dust carried to Greenland and Antarctica.

Dust concentration and composition in ice cores can be related to abrupt climatic fluctuations and glacial-interglacial transitions (Delmonte et al., 2002, Albani et al., 2018, Lunga et al., 2017) and provide a detailed record of the manner in which climate variability influences the combined processes of dust deflation, transport, and deposition processes. Indeed, the glacial-interglacial climate changes are correlated with sequences of high and low dust concentrations ranging from 800 to 15 $\mu g\,kg^{-1}$ over the past climate cycles, with different particle size distribution in different sites over the same climatic period (Delmonte et al., 2004). On a global scale, last glacial maximum dust deposition rates were 2–4 times higher than during the Holocene (Maher et al., 2010, Kohfeld and Harrison, 2001, Ruth et al., 2003). The EPICA-Dome C and Vostok Antarctic ice cores provide evidence of this significant increase that is inversely correlated with temperature, global sea level, and atmospheric CO_2 concentration (Lambert et al., 2008, Petit et al., 1999).

Despite the well-recognized importance of past changes in mineral dust aerosol dis-

tribution and content for the estimates of climate sensitivity (Stocker et al., 2013, Carslaw et al., 2017), and although the extensive research carried out on this topic, significant uncertainties still affect current estimations. Moreover, dust plays an important role in glacial-interglacial cycles (Lambert et al., 2008, 2013), but model simulations show that dust can both dampen or reinforce glacial-interglacial climate changes depending on its optical parameters (Bauer and Ganopolski, 2014). This uncertainty is related to the poor knowledge of dust optical properties and the way they can change within a given climate period (Formenti et al., 2011, Mahowald et al., 2014).

Retrieving the information within an ice core brings the optical properties of dust and the optical techniques to the foreground. Because of the shallow concentration and the size polydispersity of the dust, particle-by-particle techniques usually better fulfill the requirements of investigating grains already deposited, whereas the application of traditional light scattering approaches is limited. One of the most powerful approaches capable of characterizing the size and shape of mineral dust, or aerosol, is based on microscopy technique, like the SEM (*Scanning Electron Microscopy*) and the TEM (*Transmission Electron Microscopy*), although they are strongly time demanding and often need specific sample preparation (Villa et al., 2016). By contrast, optical methods such OPC (*Optical Particle Counter*) and SPOS (*Single Particle Obscuration Sensor*) are non-invasive and easy to be operated in line. The former measures the size from the scattering cross-section, the latter from extinction, following a Lorentz-Mie approximation (Simonsen et al., 2018). However, obtaining the size indirectly passing throw the optical signals may bring inaccurate values, and represent the limit of these optical approaches. An appreciated and widely applied technique in ice core measurements is the Coulter Counter, because of its accurate size measurement and sensitivity even to low concentrations. It measures the volume-size distributions of equivalent spherical particles immersed in an electrolyte from a variation of impedance. Also in this case, the particle size is obtained only from one parameter, thus any other feature affecting light scattering (composition, internal structure, shape, and orientation of each grain) remains unknown (Hinds, 1999). This causes discrepancies between the size distributions retrieved by such different strategies (Kahn, 1957), and calls for a multiparametric characterization where possible. For example, the Single Particle Extinction and Scattering (SPES) technique can obtain a simultaneous measurement of the real and imaginary parts of the field scattered by single mineral dust in meltwater sample illuminated by a laser beam, retrieving so at the same time the extinction coefficients and optical thickness (Potenza et al., 2016, 2017, Cremonesi et al., 2019, Cremonesi, 2021).

The present work presents the results obtained from the analysis of liquid samples, specifically, melted ice cores containing mineral dust particles, with a single-particle optical method and a multiparametric characterization.

1.4 Optical properties of dust - scattering fundamental

Micrometric or sub-micrometric particles as mineral dust, which have a complex internal structure with composite materials, are able to interact with both solar and terrestrial electromagnetic radiation by scattering the radiation and absorbing it, acting as a non-spherical polarizable obstacle. Hardly ever the light is observed directly from its source. The scattering of light may be thought of as the redirection of light that takes place when an electromagnetic (EM) wave (i.e. an incident light ray) encounters an obstacle or non-homogeneity in the medium in which it is propagating, in our case the scattering particle (Bohren and Huffman, 2008). If light traverses a perfectly homogeneous medium, it is not scattered. Only inhomogeneities (due to variations in density or refractive index) cause scattering (Van de Hulst, 1981) and they depend on the wavelength of the radiation, which determines the relevant length scale of the phenomenon (Born and Wolf, 2013). Frequently, the inhomogeneities are *alien* bodies embedded in the medium. Clear examples are water drops and dust grains in atmospheric air and bubbles in water or in opal glass. As the EM wave interacts with the discrete particle, the electron orbits within the particle's constituent molecules are perturbed periodically with the same frequency as the electric field of the incident wave. The oscillation or perturbation of the electron cloud results in a periodic separation of charge within the molecule, which is called an induced dipole moment. The oscillating induced dipole moment is manifest as a source of EM radiation, thereby resulting in scattered light radiated in many directions other than the direction of incidence—in particular the angular aperture of the forward scattering lobe depends on the size of the particles. The majority of light scattered by the particle is emitted at the identical frequency of the incident light, a process referred to as elastic scattering. In summary, the above comments describe the process of light scattering as a complex interaction between the incident EM wave and the molecular/atomic structure of the scattering object. What follows is a brief review of an essential set of theoretical tools, aiming at discussing some important properties and results.

1.4.1 Scattering amplitude

Let us consider a particle of arbitrary shape and composition illuminated by a monochromatic light source at a large distance from the particle. We will assume the laboratory system to consist of a fixed set of axes, with z being the direction

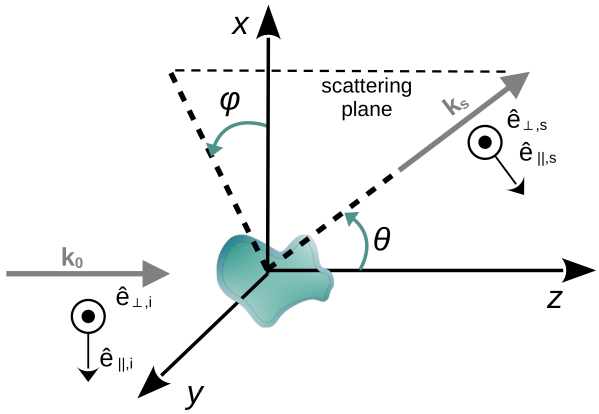

Figure 1.3: Geometry of scattering plane of an arbitrary particle showing the incident and scattered wavevectors $\boldsymbol{k}_0$ and $\boldsymbol{k}_s$. The arrows represent the direction of propagation of the fields which is parallel to the wave vector and to which the fields are orthogonal. This defines the positive direction of the z-axis, while the incident and scattering direction together define the scattering plane. $\theta = 0$ corresponds to forward scattering, while $\theta = \pi$ to backward scattering.

of propagation of the incident wave. The origin of the coordinates is chosen somewhere in the particle, as illustrated in Figure 1.3. Most scattering experiments are performed in the far-field, where $kr \gg 1$, so it can possibly treat the incoming field locally as a plane, scalar wave of infinite extent propagating in a homogeneous non-absorbing medium like air. The particle in the origin of the reference frame is exposed to an incoming field $\mathbf{E}_0 \sim e^{ikz-i\omega t}$, where $k = \frac{2\pi}{\lambda}$ and λ is the wavelength relative to the surrounding medium and scatters light at all angles. In far field approximation, one may write the incident and scattered fields in terms of a complex 4 x 4 amplitude scattering matrix (Van de Hulst, 1981)[1]:

$$\begin{pmatrix} E_{s\,\parallel} \\ E_{s\,\perp} \end{pmatrix} = \frac{e^{ik(z-r)}}{ikr} \begin{pmatrix} S_2 & S_3 \\ S_4 & S_1 \end{pmatrix} \begin{pmatrix} E_{0\,\parallel} \\ E_{0\,\perp} \end{pmatrix} \tag{1.1}$$

where i is the imaginary unit. S_1 gives the amplitude of the perpendicular component of the incident field in $E_{s\,\perp}$. Similarly, S_2 gives the amplitude of the parallel component of the incident field in $E_{s\,\parallel}$, while S_3 and S_4 give the corresponding depolarised terms. For the Lorenz-Mie problem symmetry requires the off-diagonal terms of S_3 and S_4 to be 0, and S_1 and S_2 to be almost the same (Fig. 1.4). In this case, at a distance r from the origin, we can write the scattered wave $\mathbf{E}_\mathrm{s}$ as a

[1] for simplicity, we drop the time dependence.

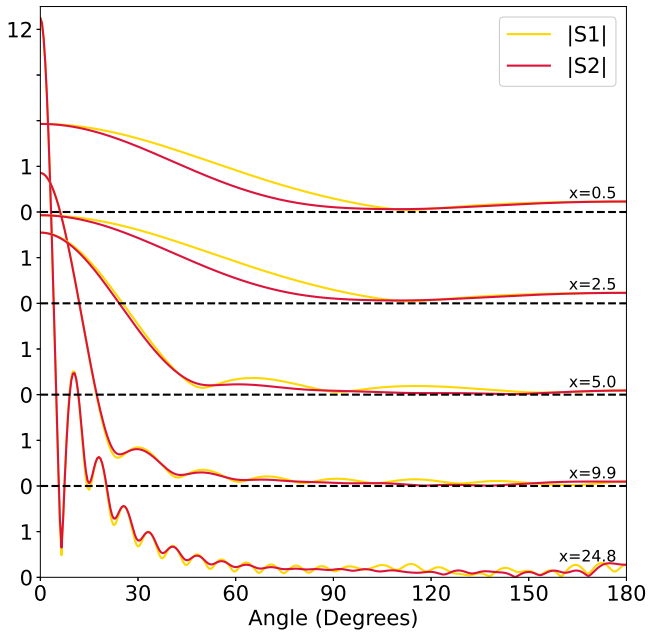

Figure 1.4: Scattering diagrams for non-absorbing micron-nanometer spheres, with $m = 1.14$ and size parameter from $x = 0.5$ to $x = 24.8$, where $x = rk$. The ordinates are proportional to the amplitudes of the scattered light in polarizations S_1 (golden lines) and S_2 (red lines). Mie calculations were conducted using the open-source package Holopy (`https://github.com/manoharan-lab/holopy`).

spherical wave modulated and dephased as follows:

$$\mathbf{E}_s(\theta, \varphi) = S(\theta, \varphi) \frac{e^{ik(z-r)}}{ikr} \mathbf{E}_0 \tag{1.2}$$

where θ is the *scattering angle* with respect to the direction of propagation of the incoming light, while ϕ is the *azimuth* angle as defined in Figure 1.3. This equation defines the *scattering amplitude*, $S(\theta, \varphi)$, a complex dimensionless quantity which links the incoming field to the scattered field, and completely determines the scattering by an arbitrary particle of finite size. A striking illustration of the change in the scattering pattern is shown in Fig. 1.4, where we have plotted the ratios $|S_1(\theta)|/x$ and $|S_2(\theta)|/x$ as a function of θ for the size parameter $x = rk$ ranging from 0.5 to 24.8. $S(\theta, \phi)$ does not depend upon the distance r at which

the particle is observed, but it does depend on its orientation with respect to the incident (plane) wave and the state of polarization of the latter.
The amplitude function may also written as:

$$S(\theta, \varphi) = s \cdot e^{i\sigma} \tag{1.3}$$

where s is positive and σ is real, and both are functions of θ and ϕ. A negative $\sigma - (\pi/2)$ denotes a phase lag of the scattered wave—usually, the scattered field is not in phase with the incident field.
However in general, the equation (1.1) is not symmetric. First particle non-sphericity contributes increasingly to the anisotropy of $S(\theta, \varphi)$ with respect to φ (Horvath, 2009). Moreover, also the polarization of the incoming light breaks this symmetry. In this work, we used linearly polarised light and investigated non-spherical particles. We should therefore consider the more general form of $S(\theta, \phi)$.
Finally, we have to note that any point of space is traversed both by the incident and scattered wave, within the extension of the $\mathbf{E}_0$, that interfere (either constructively or destructively depending on the phase of $S(\theta, \varphi)$). This is particularly relevant at small θ, where the incident field cannot be avoided by a detector. The amplitude at $\theta = 0$ is of particular significance since it is related to the total scattering cross-section, as will be detailed later on Section 2.5. Holographic technique—the principal method of this study—is based right on this interference. Otherwise, in a laboratory, a detector placed at large θ or with a large objective and at a very large distance has sufficiently resolving power to separate the two contributions.

The intensity of the scattered light is proportional to the square of the amplitude of $S(\theta, \varphi)$, so we have

$$I_\mathrm{s}(\theta, \varphi) = \frac{|S(\theta, \phi)|^2}{k^2 r^2} I_0 = \frac{s(\theta, \phi)^2}{k^2 r^2} I_0 \tag{1.4}$$

The quantity $s(\theta, \phi)^2$ reflects the internal structure of the particle (Debye and Bueche, 1949, Debye et al., 1957). Usually, one drops the dependence on ϕ by taking a rotational average, whereas its trend as a function of the scattering angle θ gives the structure factor.

1.4.2 Extinction, scattering, absorption

We imagine surrounding a particle with a large imaginary surface a (such that we are in the far-field) embedded in a non-absorbing medium and integrating the Poynting vector due to the external fields (incident and scattered) over this surface (Fig. 1.5). The rate at which energy is lost inside the surface is:

$$W_a = \int \mathbf{S} \, \mathrm{d}a \tag{1.5}$$

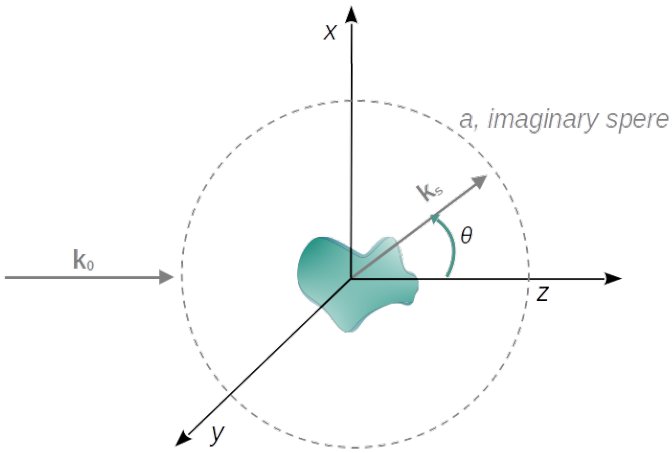

Figure 1.5: Absorption by a single arbitrary particle embedded in a non-absorbing medium and illuminated by a plane wave. To obtain the absorption cross-section, we calculate the rate at which energy is lost inside the imaginary surface "a" around the particle. This is equivalent for scattering and extinction.

If $W_a > 0$, (if W_a is negative, energy is being created within the sphere, a possibility we exclude from consideration), energy is absorbed within the sphere. But the medium is non-absorbing, which implies that W_a is the rate at which energy is absorbed by the particle. If we divide this by the incident irradiance I_i, which for a z-propagating incident field is the z component of its Poynting vector, we get something with units of area. This is the so-called absorption cross-section, C_{abs}. In a similar way, considering the scattered power, we can define the scattering cross-section:

$$C_{\text{sca}} = \frac{1}{I_i} \int \mathbf{S}_{\text{sca}} \, \mathrm{d}a \tag{1.6}$$

where $\mathbf{S}_{\text{sca}}$ is calculated with the scattered field.
If we get the dimensionless vector scattering amplitude $S(\theta, \varphi)$ as defined in Eq. (1.2), then it can be shown that an integral over 4π of solid angle gives the scattering cross-section:

$$C_{\text{sca}} = \frac{1}{k^2} \int_{4\pi} |S(\theta, \varphi)|^2 \, \mathrm{d}\Omega. \tag{1.7}$$

where $\mathrm{d}\Omega = \mathrm{d}\varphi \, \mathrm{d}(\cos\theta)$ is the element of solid angle. Consequently $|S(\theta, \varphi)|^2 / k^2 C_{\text{sca}}$ is normalized with respect to integration over solid angle.
The quantity $|S(\theta, \varphi)|^2 / k^2$ is sometimes called the *differential scattering cross-section*, defined as the cross-section per unit solid angle and denoted symbolically

by $C_{\mathrm{sca}}/\,\mathrm{d}\Omega$, so that

$$C_{\mathrm{sca}} = \int_{4\pi} \frac{\mathrm{d}C_{\mathrm{sca}}}{\mathrm{d}\Omega}\,\mathrm{d}\Omega \tag{1.8}$$

Physically, $C_{\mathrm{sca}}/\,\mathrm{d}\Omega$ specifies the angular distribution of the scattered light: the amount of light scattered into a unit solid angle about a given direction (Fig. 1.6). Comparing Eq. (1.8) with the definition in Eq. (1.7) it follows that

$$\frac{\mathrm{d}C_{\mathrm{sca}}}{\mathrm{d}\Omega} = \frac{1}{k^2}|S(\theta,\varphi)|^2 \tag{1.9}$$

This physical quantity bears essential information about the internal structure of the scatterer. For example, in Fig. 1.6 we show the differential scattering cross-section as a function of the scattering angle for three particles of different sizes. The angular dependence of the scattering cross-section is precisely what distinguishes a sphere from an amorphous particle having the same geometrical cross section or the same volume. We can define the *phase function*[2] as the angular distribution of light intensity scattered by a particle normalised by its integral

$$p = \frac{|S(\theta,\varphi)|^2}{k^2 C_{\mathrm{sca}}} = \frac{\frac{\mathrm{d}C_{\mathrm{sca}}}{\mathrm{d}\Omega}}{C_{\mathrm{sca}}} = \frac{|S(\theta,\varphi)|^2}{\int_{4\pi} |S(\theta,\varphi)|^2\,\mathrm{d}\Omega} \tag{1.10}$$

that is so normalized $\int_{4\pi} p\,\mathrm{d}\Omega = 1$. The phase function is the most complete description of the scattering pattern (Mishchenko et al., 1995, Bond et al., 2013). A major concern has been the differential scattering cross-section of mineral dust, and therefore the extinction cross-section, which is found to vary substantially from those of equivalent spheres based on Lorenz–Mie theory suited for homogeneous or spherical core-shell particles, as extensively reported in Nousiainen (2009). By definition, such approach fails to account for the particle shape, which has been acknowledged as a determining factor for the response to electromagnetic waves in the visible and near-infrared spectrum especially for micron-sized particles (Kahnert et al., 2007).

From the phase function, we can also characterize how homogeneously a sphere scatters light. The electric field radiated from a point dipole scatterer is (for polarization perpendicular to the scattering plane) independent of θ. A large particle, by contrast, tends to scatter most strongly in the forward direction. We can quantify this with the asymmetry parameter γ, defined as the intensity-weighted average of

[2]The word *phase* has come into this expression via astronomy (lunar phases) and has nothing to do with the phase of a wave.

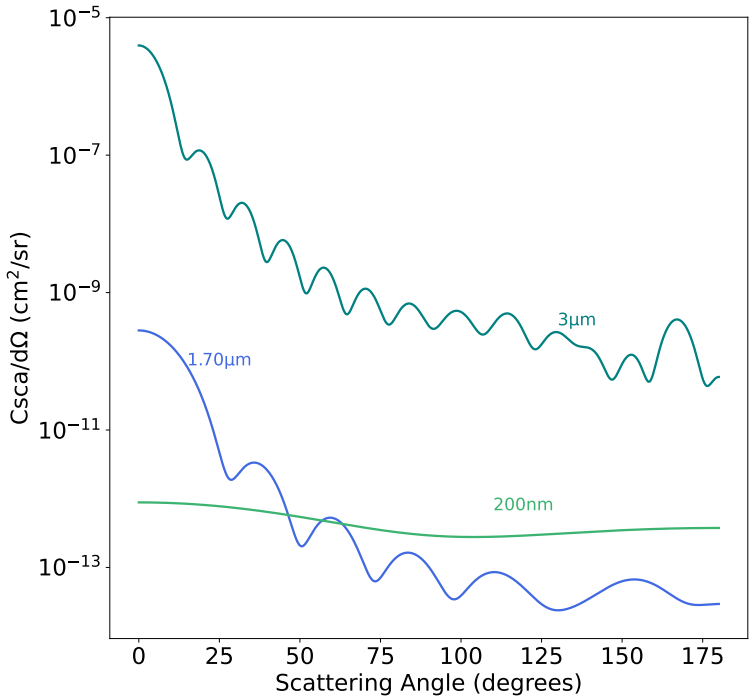

Figure 1.6: Differential scattering cross-section in function of the scattering angle for polystyrene beads of 200 nm, 1.70 µm *and* 3 µm *size-diameter. Mie calculations were conducted using the open-source package MiePython (`https://miepython.readthedocs.io/en/latest/`).*

the cosine of the scattering angle, such that

$$\gamma = \frac{1}{k^2} \int_{4\pi} |S(\theta, \varphi)|^2 \cos\theta \, \mathrm{d}\Omega. \tag{1.11}$$

Isometric scattering would ideally give $\gamma = 0$, a value to which small particles come close. Whereas, non-absorbing particles of increasing size scatter mainly in the forward direction so that γ approaches 1. A reflecting (metallic) particle would give negative values of the asymmetry parameter instead, up to the limiting case of a perfect mirror where $\gamma = -1$ (purely forward scattering).

The law of conservation of energy requires that the extinction cross-section C_{ext} is given by the sum of the scattering and absorption cross sections:

$$C_{\text{ext}} = C_{\text{sca}} + C_{\text{abs}}; \tag{1.12}$$

which might be phrased as *extinction = scattering + absorption*. C_{ext} is related to the total energy removed from the incident beam, by absorption and scattering. Therefore, for non-absorbing particles, the extinction is entirely due to scattering, and they mostly have a cooling effect on the atmosphere. The quantities $C_{\text{ext}}, C_{\text{sca}}, C_{\text{abs}}$ have the dimensions of an area and generally are functions of the orientation of the particle, the wavelength and the state of polarization of the incident light.

One also frequently encounters these cross-sections non-dimensionalized as efficiencies Q, where the non-dimensionalization comes from the ratio of the optical cross-sections to the geometric cross-section of the sphere of equivalent volume, $G = \pi r_{eq}^2$:

$$Q_{\text{ext}} = \frac{C_{\text{ext}}}{G} \tag{1.13}$$

The same definitions are for scattering and absorption efficiency factors (Van de Hulst, 1981, Bohren and Huffman, 2008). The word *efficiency* might lead us to think that extinction efficiencies can never be greater than unity. Indeed, all rays incident on a particle should either be absorbed or deflected by reflection and refraction. Really, there are very many particles that can scatter and absorb more light, than is geometrically incident upon them, and this is depending on their polarizability. Moreover, a large particle removes from the incident beam exactly twice in the far-field (see Fig. 1.7). This is known as the extinction paradox (Van de Hulst, 1981).

Another important result related to radiometry is the Optical Theorem (Newton, 1976, Van de Hulst, 1981, Bohren and Huffman, 2008), which directly follows from the conservation of energy. It relates C_{ext} to the real part of the far-field scattering amplitude in the forward direction. For the case of Lorenz-Mie scattering

$$C_{\text{ext}} = \frac{4\pi}{k^2}\mathfrak{Re}S(0) \tag{1.14}$$

where S is either non-zero element of the amplitude scattering matrix $\mathbf{S}$, which are identical at $\theta = 0$. Hence the power removed from the incident beam, which includes the integration of the power radiated at all angles, is related to the phase of the forward scattered field. We remark that by equation 1.12, $S(0)$ is then related to absorption as well. However small $\mathfrak{Re}S(0)$ might be compared to $\mathfrak{Im}S(0)$, it cannot be zero: the forward scattered field is not in phase with the incident field and must destructively interfere with it to some degree.

1.4.3 A cloud of many particles

Let us consider a collection of many independent scattering particles, far apart from each other—we can assume the inter-particle distances much larger than both

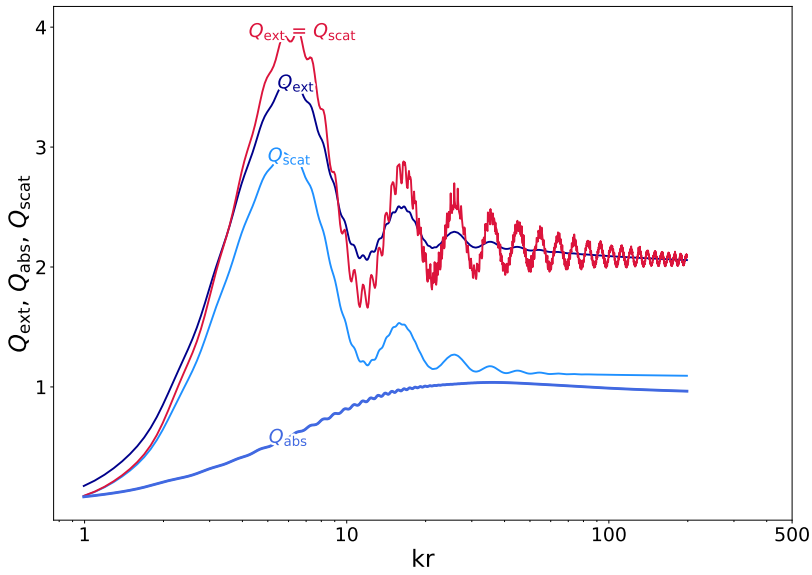

Figure 1.7: Mie calculations of the extinction efficiency of spherical water droplets as a function of the dimensionless size parameter $x = kr$ (in log scale). The red curve refers to $m = 1.33$, whereas the blue curves refer to absorbing spheres with $m = 1.33 + 0.03i$. The two lower curves refer to the scattering and absorption cross sections which add to Q_{ext}. The limit for Rayleigh scattering can be set to $x \sim 1$. Mie calculations were conducted using the Holopy open-source package.

the wavelength and the sizes of the particle—each of them characterizing by their amplitude function $S_i(\theta, \phi)$, where the index i denotes any individual particles. This ensures that the field incident on each particle is essentially given by the incoming wave, and multiple scattering is negligible. However, the differential scattering cross-section still depends on the positions of the scatterers, and the phase lag between the fields scattered at a given angle by any two particles is depending on the vector joining the two particles, thereby the phase lag $\Delta\phi$ vanishes if $\mathbf{k_0}$ is parallel to $\mathbf{k}_s$ (Born and Wolf, 2013), where we denoted with $\mathbf{k_0}$ the wave vector of the incident field, and $\mathbf{k}_s$ the wave vector of the scattered field. If the particles are randomly distributed, at any angle $\theta > 0$, as a consequence of the averaging out of constructive and destructive interference, we have that the overall intensity is approximately given by the sum of the intensities scattered by each

particle in the cloud:

$$I^{\mathrm{tot}}(\theta,\phi) = \sum_i S_i(\theta,\phi) \tag{1.15}$$

The situation for $\theta = 0$ deserves a separate discussion. The particles act like coherent emitters and interfere constructively regardless of their position in the scattering volume (Parola et al., 2014, Van de Hulst, 1981). Under this assumptions, the total scattering amplitude of an ensemble of N particles is

$$S^{\mathrm{tot}}(0) = \sum_i S_i(0) \tag{1.16}$$

By integration over all directions we find that the total scattering cross-section is thus given by

$$C_{\mathrm{ext}}^{\mathrm{tot}} = \sum_i C_{\mathrm{ext,i}} \tag{1.17}$$

The same rule holds also for the scattering and absorption cross-section, the last one as a consequence of equation 1.12.

An important diagnostic of scattering and absorption measurements is the *single scattering albedo*, which described the ratio of scattering efficiency to extinction efficiency at a particular wavelength. Its value approaches 1 for non-absorbing particles and 0 if scattering is negligible compared to absorption. A similar property, the *aerosol extinction coefficient* is defined as $\sigma_{ext} = N \cdot C_{ext}$, where N is the number of particles per cubic meter of air. The vertically integrated value of the extinction coefficient is equal to the commonly used non-dimensional *aerosol optical depth*, which represents the total amount of radiation extinguished by aerosol in an atmospheric column. The model described above is relevant for estimating the overall aerosol optical depth of the atmosphere, which may be considered a good approximation as a very rarefied cloud of solid particles immersed in a non-absorbing medium. Instead, at close distances, neighboring particles experience the coupling of internal electric fields (Kinnan and Chumanov, 2010) to an appreciable extent, so that equation (1.17) does not give the best interpretation of experimental data.

Chapter 2

Digital Holography

Particle-by-particle optical measurements contribute significantly to an all-around characterization of mineral dust by giving direct access to their optical properties, especially when many parameters are measured simultaneously and independently. Holographic particle characterization uses coherent illumination to measure properties of micrometer-sized particles, enabling a direct measurement of their size, extinction cross-section, and three-dimensional position.
The following is an introduction to the salient physical processes underlying the holographic technique. We then discuss our implementation of image analysis in Chapter 3, and conclude with an overview of the experimental results from Antarctic and Alpine ice cores by applying a holographic particle-by-particle characterization. Particular attention was given to the shape of the particles which consistently exhibit a considerable non-sphericity.

2.1 Overview

Digital holography (DH) is a technique that has been widely used in the fields of optics. It is well suited for the investigation of micro-components, dynamic three-dimensional particle field imaging, and tracking systems. It offers a non-contact approach, preserving the samples, and it can cover a wide range of sizes. For these reasons, it has many applications that include studying contaminants in water (Philips et al., 2017), quantifying unconstrained bacterial mobility (Nadeau et al., 2016), studying protein aggregates (Kasimbeg et al., 2019), or characterizing flowing aerosol particles in air (Kemppinen et al., 2020).
It was introduced in the 1940s thanks to the study of Dennis Gabor, who at the time was working on electron microscopy and was seeking ways to avoid the problems caused by primitive electron lenses that suffered from spherical aberration (Gabor, 1948) by proposing to avoid lenses entirely. He created the word *holography* by combining the Greek words *holos*, which means *everything*, and *graphein*, which means *writing*. His idea was based on a diverging incident wave, like that shown in

Figure 2.1, which today we would refer to as *point source in-line holographic microscopy*. However, its proposal can be applied to light as well, as he demonstrated by using a mercury arc lamp and a pinhole to create an almost monochromatic, coherent source of spherical waves (Gabor, 1948, 1949). For his invention and development of the holographic method, Gabor later won the Nobel Prize. With this technique, it was possible to recover original images by illuminating the holograms in reverse. In this way, from a single image, he could *reconstruct* multiple object planes. We discuss reconstruction in more detail in Section 2.3.

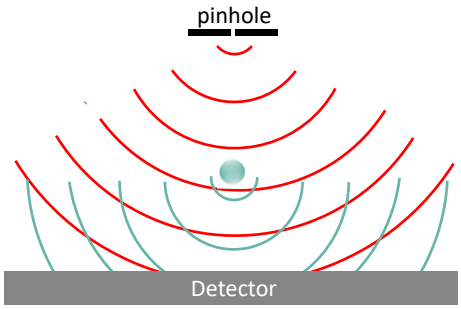

Figure 2.1: Schematic illustration of point source in-line holographic microscopy as proposed by Gabor. A spherical incident wave emanates from a pinhole and illuminates a scatterer. Because the scatterer is downstream from the pinhole, the phase difference between the scattered and incident waves will vary over the detector, which will consequently record a fringe pattern.

Although remarkable results were achieved, some limitations did not allow holography to become practical until the development of digital holographic microscopy in the 1990's[1]. Even after lasers became readily available sources of intense, coherent light, recording holograms generally required finely grained photographic films, which were difficult to chemically develop and required high time-consuming. The development of CCD/CMOS cameras, along with improvements in the computational capacity of computers, made it possible both to record holograms digitally and to simulate the optical reconstruction process numerically (Schnars and Jüptner, 1994). *Digital holograms* enjoy all the convenience of digital files, such as transport simplicity, the ability to be duplicated and sent remotely, and the possibility of being modified with relative simplicity through computer software, without losing the original image. One of the earliest works with both digital recording and numerical hologram reconstruction was that of Schnars and Juptner (Schnars and Jüptner, 1994). They proposed to image ordinary gaming die by the use of an

[1]We refer the reader interested in the historical holography development to Schnars and Jüptner (1994) and the references therein.

off-axis rather than inline configuration. They soon identified one of the limitations of CCDs as opposed to the specialized photographic films: the large pixel size ($\sim$ µm), resulting in almost two orders of magnitude larger than the resolution of holographic films. The resulting loss of high-spatial frequency information necessarily degraded the imaging resolution. Anyway, the convenience of digital recording and numerical reconstruction compared with photographic films was substantial. One solution to this problem is to reduce the effectiveness of pixel size by the use of lenses to magnify holograms (Cuche et al., 1996, Zhang and Yamaguchi, 1998). The approach of combining magnifying lenses and an off-axis holographic configuration be mostly applied in the area of biological microscopy (Cuche et al., 1999b). However, off-axis holographic instruments have the disadvantage of a much more challenging setup and alignment, and quantitatively precise reconstruction can be harder. An alternative approach to overcome the problem of large CCD pixel sizes was given by the idea to use an in-line configuration with illumination by a point source, as in Figure 2.1 (Kreuzer et al., 1999, Xu et al., 2002). In particular, since in this setup the wave from the point source diverges, it is possible to magnify the hologram fringe pattern without any lenses whatsoever, simply by placing the detector further away. The size of the hologram is equal to the size of the object area multiplied by the magnification factor $M = D/d$, where D is the distance between the object and the point source, while d is the distance between the detector and the point source. Despite the straightforward setup of this approach compared to the off-axis configuration, with no lenses that might introduce optical aberrations, it is still arguably not ideal. Indeed, the detector has to be moved far away from the point source and the scatterers (i.e. D has to be greater than d). The result is that the detector, having a limited side length ($\sim 4\,\mathrm{cm}^2$), collects only light at small scattering angles, missing important information about the size of scatterers. However, non-spherical particles, or particles that exhibiting surface roughness or protuberances, tend to scatter light at higher angles (see Sec. 2.2, Figure 2.5).

The optical configuration we used in this thesis is described in Chap. 3 and it is shown schematically in Figure 2.2, with the insertion of a microscope objective lens between the scatterer and the detector to magnify the hologram. It is a combination of the magnifying optics (as in the work of Cuche et al.) and the in-line setup with plane wave (as in Kreuzer et al.), similar to Lee et al., Berg and Videen and Sheng et al.. This setup allowed the effective hologram plane to remain relatively close to the scatterers (within hundreds of µm), achieving a greater scattering angle coverage with high numerical aperture objectives (N.A. $\sim$ 40).

We conclude with a list of symbols and abbreviations in table 2.1, which will be useful for the rest of the reading.

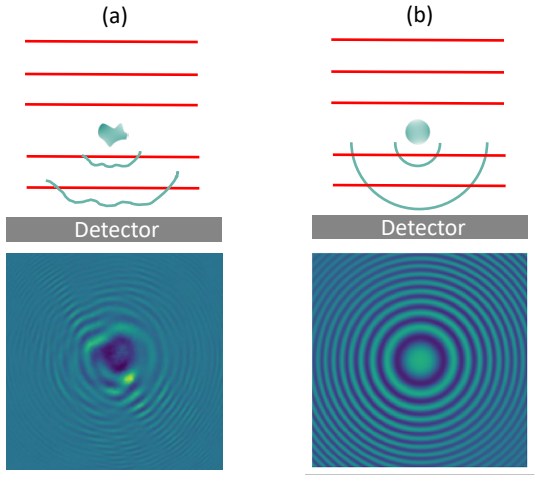

Figure 2.2: Schematic overview of in-line digital holography (DM). A coherent plane wave from a laser illuminates a complex shape scatter (a) and a spherical scatter (b). The interference pattern, recorded by the detector and placed after the object, is formed between the scattered light (green lines) and the unscattered incident light (red straight lines).

Description	Symbol
Digital holography	DH
Extinction cross-section	C_{ext}
Cross sectional area, orthogonal to the optical axis	*csa*
Aspect ratio, the ratio between the major and minor axes of the *csa*	*ar*
Thickness (along the optical axis) to diameter ratio	*tdr*
Coordinates on the hologram plane	(ξ, η)
Coordinates on the objects plane	(x_0, y_0)
Wavenumber	$k = \frac{2\pi}{\lambda}$
Complex scattering amplitude	S(0)

Table 2.1: List of symbols and abbreviations

2.2 Encoding scatterer information

To understand holography, we need to consider the wave nature of light. At any point in space, a light wave can be described by an amplitude and phase of the oscillating electromagnetic field. Coherent imaging preserves the phase information that is instead averaged away in conventional incoherent images. Therefore, whereas a conventional photograph captures the intensity of light reflected or scat-

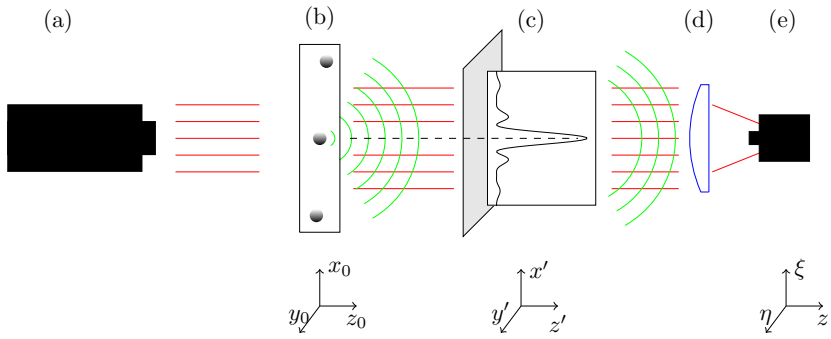

Figure 2.3: Diagram of in-line digital holographic microscopy (DHM). A collimated laser beam (a) impinges on a thin cell (b) through which samples are flown to be measured, placed at the (x_0, y_0, z_0) plane. A microscope objective (d) is located in the far-field of the sample. A sensor (e), placed on the (ξ, η, z) plane, records the holographic pattern resulting from the interference of the faint scattered (green lines) and transmitted waves (red lines). The insert (c) shows the longitudinal intensity profile of a holographic pattern along an arbitrary (x', y') plane.

tered from an object, a hologram can record both the amplitude and phase of a wave. The position and physical properties of individual scatterers are encoded in this phase information and can be extracted by reconstructing the pattern (Sec. 2.3) or fitting the resulting intensity patterns to an appropriate light scattering theory (Sec. 2.4).

The Figure 2.3 illustrates the working principle of in-line digital holographic microscope (DHM). A coherent laser with plane wave (a) impinges onto a scatterer into the sample (b), which we assume has an object's density not exceedingly large. Some of this incident light is scattered by the particle (the *object beam*, green lines), while most of the incident light does not interact with the particle and proceeds undisturbed (the *reference beam*, red lines). Therefore, if the two waves are coherent (temporally and spatially), it is possible to record at the plane of the detector (e) an interference pattern—the so-called *hologram pattern*—resulting from the faint scattered light and the unscattered incident light, and magnifying by the objective lens (d). The concentric fringes of the hologram pattern are centered around the particle position in the lateral (ξ and η) directions, perpendicular to the optical axis. While the spacing of the fringes encodes the position of the particle in z_0, that is the distance along the optical axis between the particle and the hologram plane. The dependence on the optical axis position is also shown in Figure 2.4: as the distance z increases (1) the spacing of the fringes increases and (2) the contrast in the hologram fringes decreases. The last one is due to the approximate $1/r$

dependence of the scattered electric field, as we can see in Eq. 1.2. The simula-

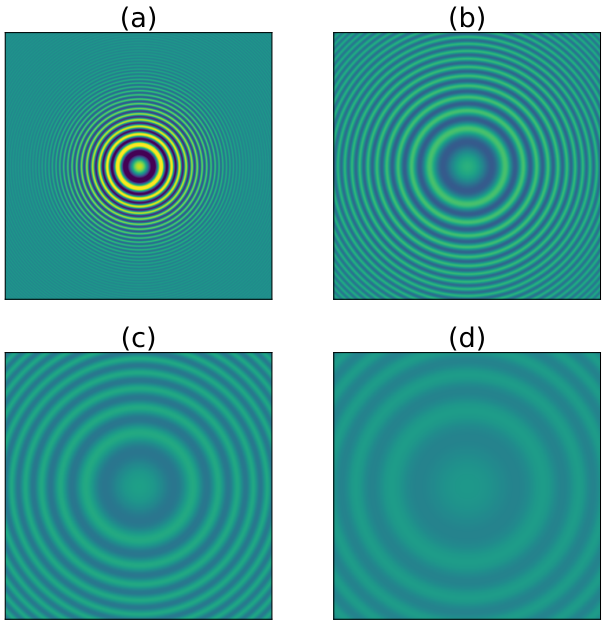

Figure 2.4: Simulated holograms of a 1 µm*-diameter polystyrene sphere in water with different z, from* 50 µm *(a),* 150 µm *(b),* 300 µm *(c), to* 600 µm *(d). As z increases, the spacing between the hologram fringes increases and the contrast decreases. We reported the output as a color gradient with the same scale (minimum value: blue, maximum value: yellow). Holograms are simulated using the Lorenz-Mie formalism described in Sec. 2.4 and App. B, with an in-line optical setup (detector shape* $= 300$ pixel^2*, pixel size* $= 0.26\,\mu\text{m}$*,* $\lambda = 0.633\,\mu\text{m}$*). Calculation were conducted using the open-source package HoloPy.*

tions shown in Figure 2.4—and in general in above this work—were performed using the open-source package *HoloPy* (`https://github.com/manoharan-lab/holopy`). HoloPy scattering computations perform the Lorenz-Mie formalism, including layered sphere, Mie superposition calculation, and DDA calculations. These theories are used to accurately simulate light scattering from a particle of known size and arbitrary shape. The scattered light is then superimposed with the incident light to generate a simulated contrast hologram.

Anyway, a hologram contains far more information in addition to particle position, because it hosts a footprint of the scatterer that generated it, and therefore its characteristics (dimension, refractive index, extinction, ...). First, the amplitude of

the hologram fringes is modulated by the angular dependence of the scattered light from the particle, which depends, in general, on its size and refractive index. As it is shown in Figure 2.4 and 2.5, the amplitude of the hologram fringes decreases towards the edges (or equivalently, as the scattering angle increases). In Figure 2.5 we show two simulated holograms of a polystyrene sphere 5 µm in diameter (a), and 2 µm in diameter (b). The plots of the intensity across the horizontal black lines in Figure 2.5, on the right, show that the fringes of the two holograms have different envelopes, which are approximately set by the amplitude of the scattered electric field (dashed red lines).

Moreover, the geometry of the particles can break the circular symmetry of the interference path. When a source impinges on an ellipsoid or a cylinder, for example, the intensity of the hologram path is elongated due to the sides of the ellipsoid (or cylinder) that scatter light more than the ends. We report an example in Figure 2.6 (a, d), where we simulated a spheroid with semi-axes (a, a, c) aligned with a hypothetical axis x, while z is the direction of the source. Anyway, if we change the orientation of the spheroid such that it is aligned with the optical axis z—so the sources illuminate a "spherical" cross-sectional area (with r = a)—the intensity of the hologram path exhibits, in turn, circular fringes (Figure 2.6 (b, e)). We can distinguish it from a sphere only by the measurement of the C_{ext} value (Sec. 2.5 and 3.2). The more complex is the geometry of the scatterer and the more the hologram pattern exhibits irregular fringes as opposed to the circular fringes, that reveal its shape. In Figure (2.6) (c, f) we show the result from an aggregate of three polystyrene beads of different sizes. If more than one particle is in the field of views of the source, their patterns will overlap but could be distinguishable in the reconstruction.

2.3 Holographic registration and reconstruction

In this section, we will model mathematically the physical process that leads to the formation of an image of an illuminated particle at the focal plane of the objective lens. We will assume that a scatterer is illuminated by an incident plane wave $\mathbf{E}_0(\mathbf{r})$. Monochromatic light has a time dependence of $e^{-i\omega t}$. Measurements of the light's intensity are time averaged over the duration of the camera's exposure period of at least 10 µm. As we will be imaging with a wavelength λ of 633 nm (with frequency $\omega \sim 473$ THz), our time average will include billions full cycles; we will therefore safely neglect this time dependence. As this incident illumination propagates in the $\hat{z}$ direction through the meltwater sample, it scatters from the particles, each of which will emits a diverging scattered wave, $\mathbf{E}_{\text{s}}(\mathbf{r})$, in response. For the kind of interest in this study, the scattered field is dominated by forward

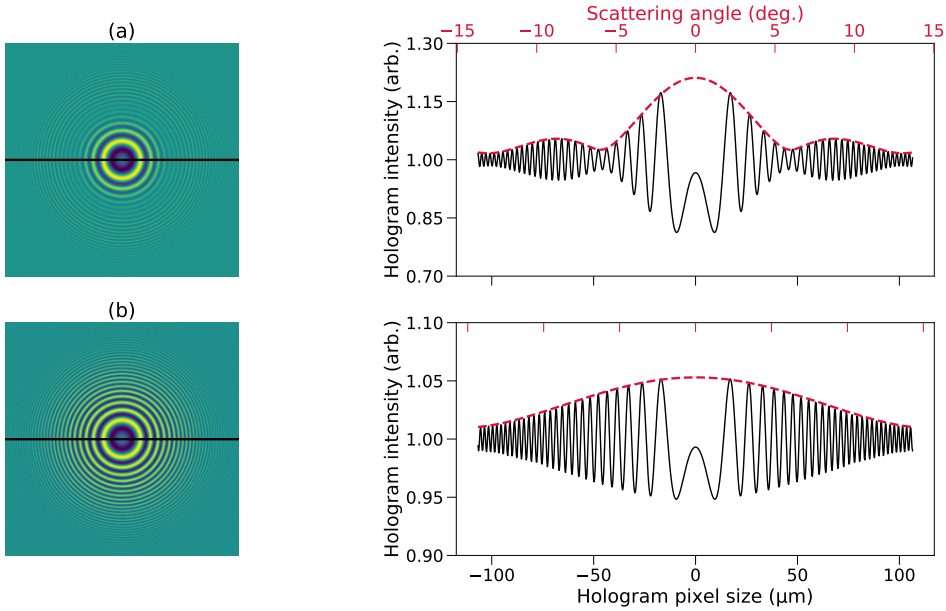

Figure 2.5: Amplitude of scattered field sets envelope of hologram fringes. Simulated holograms shown 2.5 µm *radius (a) and* 1 µm *radius (b) polystyrene spheres (n = 1.58) in water. Solid lines on the right plots show hologram intensity along horizontal black lines in the left. Dotted red lines show amplitude of in-plane components of scattered electric field computed in simulations, shifted vertically for clarity and normalized by* $2\sqrt{Q_{ext}\pi x^2/z}$*, where* $x = kr$ *is the dimensionless size parameter and* Q_{ext} *the total extinction efficiency. We reported the output as a color gradient (minimum value: blue, maximum value: yellow). Computational parameters: detector shape =* 821 pixel^2*, pixel size =* 0.26 µm*,* $\lambda =$ 0.633 µm*,* $z =$ 420 µm*.*

scattering (because the angle of detection θ_{det} is small) and the scatterer absorbs a negligible proportion of the incident wave. Both of these waves, the incident and the scattered wave, illuminate a detector, which records an interference pattern. In general, detectors (such as the pixels of a camera, or the human eye) are sensitive not to electric fields directly, but to the intensity I. In particular, because the detector in an in-line configuration records both the scattered wave as well as the unscattered incident wave, the intensity recorded for a hologram is

$$\begin{aligned} I(\mathbf{r}) =& |\mathbf{E}_0 + \mathbf{E}_\text{s}|^2 \\ =& |\mathbf{E}_0|^2 + \mathbf{E}_0\mathbf{E}_\text{s}^* + \mathbf{E}_0^*\mathbf{E}_\text{s} + |\mathbf{E}_\text{s}|^2. \end{aligned} \tag{2.1}$$

This relation holds true regardless of any assumptions made by a reconstruction

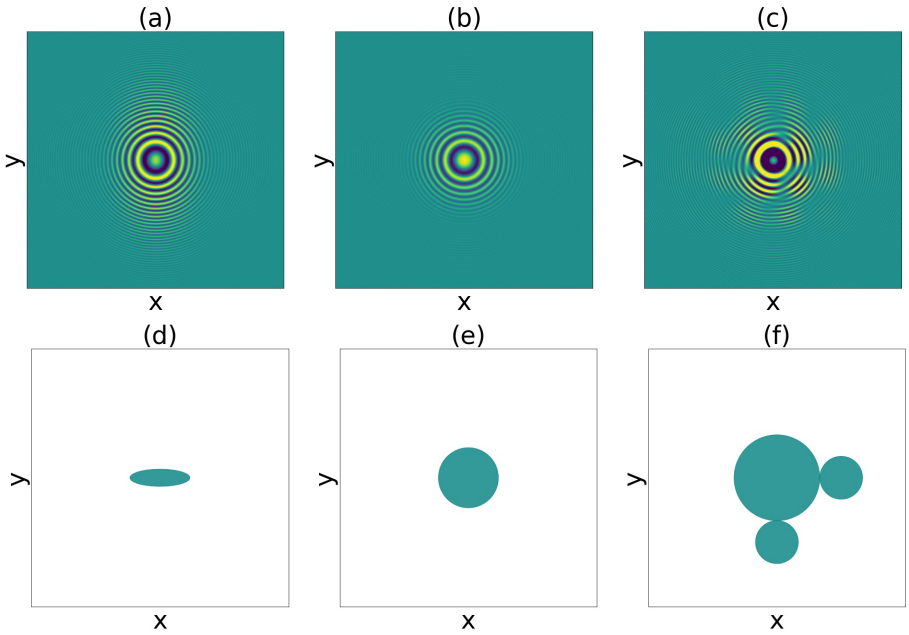

Figure 2.6: Simulated holograms of more complex scatterers. (a, d) Prolate spheroid with (0.7, 0.7, 0.2) µm semi-axis in water aligned with an hypothetical x-axis and (b, e) aligned with the z-axis. (c, f) An aggregate of three polystyrene spheres of different diameters (d_1=2 µm, d_2=1 µm, d_3=1 µm). Computational parameters: detector shape = 401 pixel^2, pixel size = 0.2 µm, λ= 0.633 µm, z = 40 µm, m = 1.18. In HoloPy by default these objects are aligned with the z-axis, but they can be rotated into any orientation by passing a set of Euler angles.

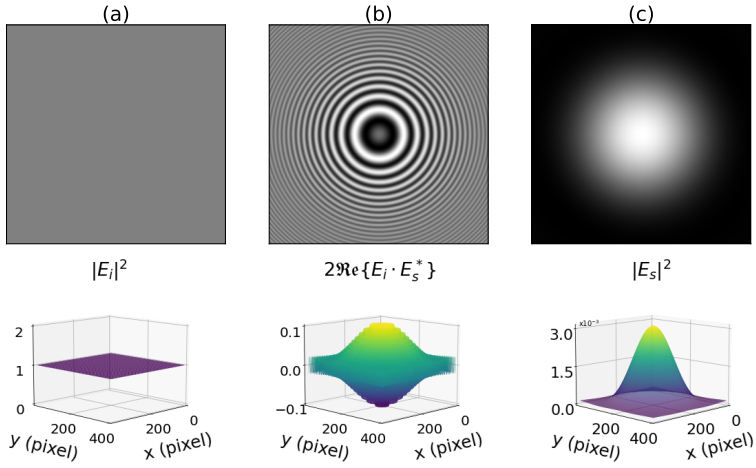

Figure 2.7: Depicting separately the three intensity contributions to a holographic image formed by a 2 micrometer-sized diameter scatterer. Computational parameters: detector shape $= 401$ pixel^2*, pixel size* $= 0.26\,\mu$m, $\lambda = 0.633\,\mu$m, $z = 200\,\mu$m, $m = 1.19$.

technique. Figure 2.7 presents a simulate holographic image for a 2 µm diameter polystyrene sphere ($n = 1.58$). The relative contributions of the terms in Eq. 2.1 are illustrated in Figure 2.7 (a), (b) and (c). The first term, $|\mathbf{E}_0|^2$, is a DC term due to the unscattered wave alone: for plane wave illumination, it is constant over the field of view and incorporates no phase information. The last term, $|\mathbf{E}_\mathrm{s}|^2$, is a self-interference term and corresponds to the intensity of the diffracted wave at the sensor plane. It is also real-valued but is not constant over the field of view. The second term, $\mathbf{E}_0\mathbf{E}_\mathrm{s}^* + \mathbf{E}_0^*\mathbf{E}_\mathrm{s} = 2\mathfrak{Re}\{\mathbf{E}_0 \cdot \mathbf{E}_\mathrm{s}^*\}$, contributes the spatially-varying interference pattern from the phase profile of the scattered wave. To obtain the original image of the object from the recorded hologram a second step is needed, which was traditionally (non-digitally) achieved by illuminating the recording medium with the same reference wave. The fringes of a recorded hologram essentially act as a zone plate[2] and can focus light when illuminated. In particular, by shining light backwards through the hologram, it is possible to reconstruct the field scattered by the particle. Digitally, this operation is possible with some approximations. First of

[2]A zone plate is a device used to focus light or other things exhibiting wave character. They are circular diffraction gratings with radially increasing line density, where the position of adjacent zones reproduce that of Fresnel half period zones, which alternate between being opaque and transparent. Light hitting the zone plate will diffract around the opaque zones. The zones can be spaced so that the diffracted light constructively interferes at the desired focus, creating an image there.

all, one assumes that scattering is weak: $|\mathbf{E}_\mathrm{s}| \ll |\mathbf{E}_0|$. Consequently, the last term in Equation 2.1 may be neglected relative to the remaining terms. Illuminating the hologram backwards is akin to multiplying Equation 2.1 by $\mathbf{E}_0^*$. If we had an incident plane wave e^{ikz}, where k is the scattered wavevector, backwards-propagating wave would have the form e^{-ikz}. Therefore, we obtain

$$\mathbf{E}_0^* I(\mathbf{r}) = \mathbf{E}_0^* |\mathbf{E}_0|^2 + \mathbf{E}_\mathrm{s}^* + \mathbf{E}_0^{*2} \mathbf{E}_\mathrm{s} \tag{2.2}$$

at the hologram plane. The second term here is $\mathbf{E}_\mathrm{s}^*$, a backwards-propagating version of the scattered wave. In particular, if $\mathbf{E}_\mathrm{s}$ is a spherical wave outgoing from the hologram plane is described in Eq. 1.2 but with the opposite sign because we have a backwards-propagation:

$$\mathbf{E}_\mathrm{s}(\mathbf{r}) = S \cdot \frac{e^{ikr}}{-ikr} \mathbf{E}_0 \tag{2.3}$$

where r is the distance between the particle and a point on the hologram plane, then

$$\mathbf{E}_\mathrm{s}^*(\mathbf{r}) = S^* \cdot \frac{e^{-ikr}}{ikr} \mathbf{E}_0^*. \tag{2.4}$$

This is a spherical wave converging at the origin, where the particle was: this is why we can state that the reconstruction recovers the wave scattered by the particle.
In Equation 2.2 the first term, arising from the DC background, will once again be constant[3], but the third term, proportional to $\mathbf{E}_\mathrm{s}$, will give rise to the *twin image* artifact, i.e. a wave that converges on the opposite side of the hologram plane as the real image from $\mathbf{E}_\mathrm{s}^*$. This twin image problem was recognized early on by Gabor (Gabor, 1949), and by trying to eliminate this unwanted feature, holographic off-axis techniques have been developed. In-line reconstruction approaches generally ignore the twin image, assuming that the field due to the twin image near the focal point of the real image is small.
Once we have $\mathbf{E}_\mathrm{s}^*$ at the hologram plane (from Equation 2.2, neglecting DC and twin image contributions), it is then necessary to propagate this field from the hologram plane. The field $\mathbf{E}_\mathrm{s}^*(x', y', z')$ at an arbitrary point (x', y', z') is related to the field $\mathbf{E}_{\mathrm{s,hp}}^*(\xi, \eta, z)$ at the hologram plane via the Fresnel-Kirchoff diffraction formula (Benzie, 2008, Latychevskaia and Fink, 2015):

$$\mathbf{E}_\mathrm{s}^*(x', y', z') = \frac{1}{\lambda} \int\int \mathbf{E}_{\mathrm{s,hp}}^*(\xi, \eta) \frac{e^{ik\rho}}{ik\rho} \,\mathrm{d}\xi \,\mathrm{d}\eta. \tag{2.5}$$

Here λ is the wavelength of the illuminating light, ξ and η are coordinates in the hologram plane, the integrals run over the entire hologram plane, and

$$\rho = \sqrt{(\xi - x')^2 + (\eta - y')^2 + z'^2} \tag{2.6}$$

[3]Usually, it is possible to measure and subtract off the DC background term prior to the reconstruction.

denotes the distance between a point in the detector plane $P_0(\xi, \eta, z = 0)$ and a point in the arbitrary plane $P_1(x', y', z')$, as illustrated in Fig. 2.8.

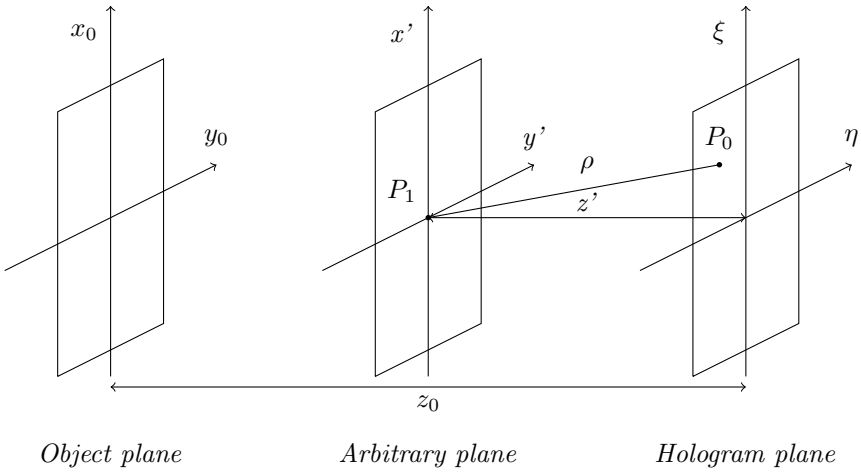

Figure 2.8: System of coordinates and distances involved in the reconstruction of a digital hologram. (ξ, η, z=0) are the coordinates in the hologram plane, (x', y', z') in an arbitrary plane, while (x_0, y_0, z_0) in the object plane.

We have here neglected the obliquity factor z'/ρ, because the angles are approximately 0. For ξ and η values as well as for x' and y' values, which are small compared to the distance z' between the reconstruction and the detector plane, the expression Eq. 2.6 can be approximated with the Taylor series expansion:

$$\rho = z' + \frac{(\xi - x')^2}{2z'} + \frac{(\eta - x')^2}{2z'} - \frac{1}{8}\frac{[(\xi - x')^2 + (\eta - x')^2]^2}{z'^3} + ... \tag{2.7}$$

When the z' distance is sufficiently large

$$z'^3 \gg \frac{1}{8\lambda}\left[(\xi - x)^2 + (\eta - y)^2\right]^2, \tag{2.8}$$

so that the Fresnel approximation is fulfilled, Eq. 2.5 turns into

$$\mathbf{E}^*_{\mathrm{s}}(x', y', z') = \frac{1}{\lambda z}\int\int \mathbf{E}^*_{\mathrm{s,hp}}(\xi, \eta)\frac{e^{\frac{ik}{z'}[(\xi - x')^2 + (\eta - y')^2]}}{ik}\,\mathrm{d}\xi\,\mathrm{d}\eta. \tag{2.9}$$

Since the integrand in Equation 2.9 depends only on the differences $\xi - x'$ and $\eta - y'$, we may write $\mathbf{E}^*_{\mathrm{s}}(x', y', z')$ as a convolution:

$$\mathbf{E}^*_{\mathrm{s}}(x', y', z') = \mathbf{E}^*_{\mathrm{s,hp}}(\xi, \eta) * h \tag{2.10}$$

where h is the impulse response function of free space:

$$h * (\xi - x', \eta - y') = \frac{1}{\lambda} \frac{e^{ik\rho}}{ik\rho}. \tag{2.11}$$

Recalling the convolution theorem, thanks to the fast Fourier transform it is computationally faster to compute $\mathbf{E}^*_{\mathrm{s}}(x', y', z')$ using the transfer function $H = \mathcal{F}\{h\} = e^{i\pi\lambda z'\left(u^2+v^2\right)}$, where $\mathcal{F}$ denotes the Fourier transform and (u, v) the Fourier domain coordinates. Therefore the hologram reconstruction consists in calculating the inverse Fourier transform of the multiplication of the Fourier transform of $\mathbf{E}^*_{\mathrm{s,hp}}$ with H:

$$\mathbf{E}^*_{\mathrm{s}}(x', y', z') = \mathcal{F}^{-1}\{\mathcal{F}\{\mathbf{E}^*_{\mathrm{s,hp}}\} \cdot H\}. \tag{2.12}$$

The actual computational implementation is somewhat less straightforward than this; in particular, experimentally recorded holograms are not continuous functions. This is the consequence of the use of a digital detector, which has in output a discrete number of values, one for each pixel, in addition to the noise that can not be entirely avoided.

2.3.1 Angular spectrum method

The angular spectrum method is based on the concept that the plane wave propagation can be described by the propagation of its spectrum (Ratcliffe, 1956, Goodman, 2005) and does not use any approximations. We start to define the components of the scattering vector

$$\mathbf{k} = \frac{2\pi}{\lambda} (\cos\varphi \sin\theta, \sin\varphi \cos\theta, \cos\theta) \tag{2.13}$$

which are related to the Fourier domain coordinates (u, v) as follows:

$$\begin{aligned} \cos\varphi \sin\theta &= \lambda u \\ \sin\varphi \cos\theta &= \lambda v \end{aligned} \tag{2.14}$$

where $(\lambda u, \lambda v)$ are the direction cosines of the vector $\mathbf{k}$. As a consequence, the following condition is fulfilled:

$$(\lambda u)^2 + (\lambda v)^2 \leq 1. \tag{2.15}$$

Therefore the reconstruction of the hologram is calculated by using the formula (Goodman, 2005):

$$\mathbf{E}^*_{\mathrm{s}}(x', y', z') = \mathcal{F}^{-1}\left[\mathcal{F}\{\mathbf{E}^*_{\mathrm{s,hp}}\} \cdot e^{-ikz'\sqrt{1-(\lambda u)^2-(\lambda v)^2}}\right]. \tag{2.16}$$

Due to the constraint described in Eq. 2.15, the term $e^{\pm ikz'\sqrt{1-(\lambda u)^2-(\lambda v)^2}}$ has non-zero values in the range of $(\lambda u, \lambda v)$, which thus acts like a low-pass filter. Eq. 2.15 set also the limit for the maximal possible frequency in the Fourier domain:

$$\lambda u_{\max} = 1. \tag{2.17}$$

Recalling the definitions of the Fourier domain coordinates (Eq 2.14) we obtain:

$$\lambda u_{\max} = \sin\theta_{\max} = 1, \tag{2.18}$$

where $\theta_{\max}$ is the greater angle of the scattered wave. The condition given by Eq. 2.15 relates to the classical resolution limit, whereby we can defined the lateral resolution, given by the Abbe criterion (Abbe, 1881, 1883), as:

$$\mathrm{R}_{\mathrm{lateral}} = \frac{\lambda}{2\sin\theta_{\max}} = \frac{\lambda}{2} \tag{2.19}$$

2.3.2 Resolution in in-line holography with plane waves

We can define the lateral resolution as

$$\mathrm{R}_{\mathrm{lateral}} = \frac{\lambda z_0}{N\Delta} = \frac{\lambda z_0}{S}, \tag{2.20}$$

which is in general valid for digital Gabor in-line holography. In particular, z_0 is the distance between the sample and the detector, and $S = N\Delta$ is the side length of the hologram, N denotes the number of pixels and Δ is the pixel size in the hologram plane.

In practice, the resolution of in-line holography depends on the spacing and visibility of the interference fringes at large diffraction angles, resulting from the interference between the reference and the object waves scattered. Moreover, a further limit for the resolution is set by the mechanical stability of the optical setup. A quantitative value of the lateral resolution can be achieved by the highest observable frequency in the Fourier domain $u_{\max}$—similar to the resolution estimation in coherent diffractive imaging. If $u_{\max}$ is detected at a determinate pixel A from the center of the spectrum, its coordinate is given by:

$$u_{\max} = \Delta_F A, \tag{2.21}$$

where Δ_F is the pixel size in the Fourier spectrum. Using the relation 2.18, we obtain that

$$\sin\theta_{\max} = \lambda\Delta_F A. \tag{2.22}$$

Finally, from the classical Abbe resolution criterion, by Eq. 2.19 we obtain:

$$\mathrm{R}_{\mathrm{lateral}} = \frac{\lambda}{2\sin\theta_{\max}} = \frac{1}{2u_{\max}} = \frac{1}{2\Delta_F A} = \frac{S}{2A}, \tag{2.23}$$

The axial resolution (in the z-direction, along the optical axis) can be defined as a depth of focus δ:

$$\delta = \frac{2\lambda}{(2\mathrm{NA})^2}, \tag{2.24}$$

where *N.A.* is the numerical aperture of the system. This provides an estimate for the axial resolution:

$$\mathrm{R}_{\mathrm{axial}} = 2\delta = \frac{\lambda}{(\mathrm{NA})^2} \tag{2.25}$$

2.4 Fitting techniques

Despite the relative simplicity and, above all, the generality of analyzing digital holograms based on their reconstruction, this technique has some limitations that will now be briefly reviewed.

As we will describe in Chap. 3, the original position of the particle along the optical axis (i.e. the focal point, z_0) is indicated by an abrupt increase in the amplitude of $\mathbf{E}_{\mathrm{s}}^*$ (Fig. 2.11). The amplitude here exhibits a spike that indicates the presence of a particle (Goodman, 2005). However, this method shows some limits when we try to apply it to larger particles. The reconstructions of spherical particles, in fact, tend to appear elongated in the axial direction (Xu et al., 2002). We illustrate this effect in Figure 2.9, where we display the field back-propagating from the hologram plane within a $x - z$ slice. The elongation is noticeable for the 5 µm-diameter polystyrene sphere in Figure 2.9 (b), but not for the smaller scatterer (1 µm-diameter polystyrene sphere) in Figure 2.9 (a). While it would be straightforward to detect the lateral $(x-y)$ positions of the particles, the precision for detecting the axial position of strong scatterers might be an order of magnitude greater ($\sim$ hundreds of nm).

By reconstructing holograms, modeled throw an exact solution (the *Lorenz-Mie* solution for the scattering of a plane wave by isolated spheres), Pu and Meng (2003) demonstrated that the elongation arose from the waves scattered by large scattering particles (particle radius very larger than the incident wavelength λ), being far from spherical. In particular, as expressed in Eq. 2.10, the reconstructed field can be viewed as a spherical wave $\mathbf{E}_{\mathrm{s,hp}}^*$ modulated by the impulse response h, which causes the actual wavefront to deviate from the Gaussian reference sphere (Fig. 2.10). Accordingly, the spike in intensity is displaced along the optical axis far from the actual position of the scatterer. Figure 2.9 (b) shows that this displacement is of 10 µm. To avoid this artifact, we can use a model based on the Lorenz-Mie scattering solution (App. B) not simply to model hologram formation, but also to extract physical information from experimentally recorded holograms through a fitting procedure (Lee et al., 2007). The Lorenz-Mie scattering solution is a vector

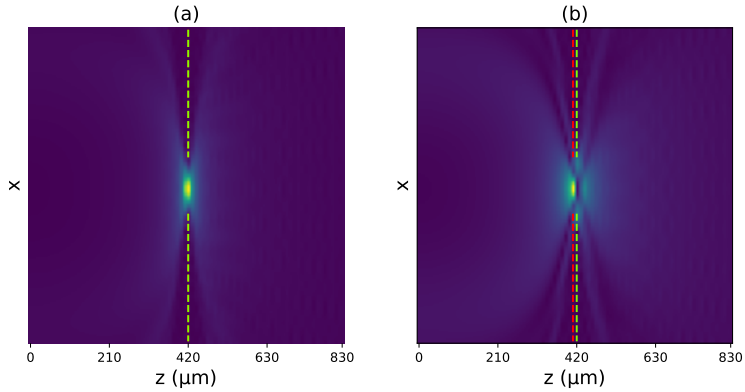

Figure 2.9: Reconstructions of simulated holograms. Slices in the $x-z$ plane of: (a) polystyrene sphere suspended in water, with radius $a = 1\,\mu\text{m}$; (b) polystyrene sphere in water, with $a = 2.5\,\mu\text{m}$. The $x - z$ slices are computed at the vertical midplane of the $x - y$ slices. Green dashed lines denotes actual z position of scatterers, while the red line the reconstructed z position. Computational parameters: detector shape $= 821$ pixel^2, pixel size $= 0.26\,\mu\text{m}$, $\lambda = 0.633\,\mu\text{m}$, $z = 420\,\mu\text{m}$.

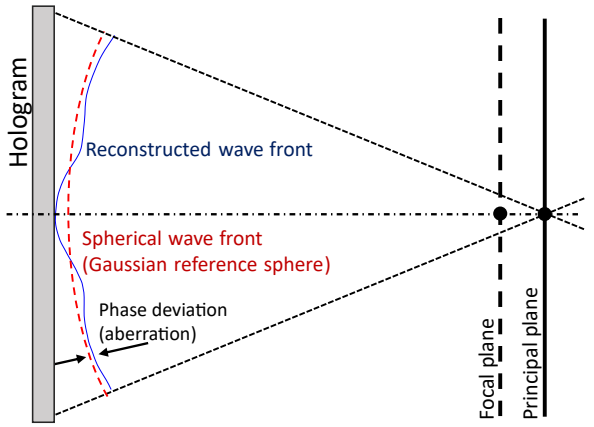

Figure 2.10: Phase deviation due to the holographic reconstruction. The wave front is deviated from the Gaussian reference sphere causing aberrations in the image reconstruction.

field solution to Maxwell's equations for the scattering of a plane wave by a sphere. We will assume the incident wave to be a plane wave propagating in the positive z direction. A key feature is that the Lorenz-Mie scattered field, $\mathbf{E}_\mathrm{s}$, depends linearly on the amplitude of the incident field $\mathbf{E}_0$. Therefore, recalling Eq. 1.2, we can define $\mathbf{E}_\mathrm{s}$ as:

$$\begin{aligned}\mathbf{E}_\mathrm{s}(\mathbf{r}) =& S(\theta,\phi)\frac{e^{ik(z-r)}}{ikr}\mathbf{E}_0 \\ =& \boldsymbol{f}(\mathbf{r})e^{ik(z-r)}\mathbf{E}_0.\end{aligned} \tag{2.26}$$

Here, $\boldsymbol{f}(\mathbf{r})$ is the vector scattering amplitude of the sphere (see for further details the Sec. 1.4). It depends not only on the distance vector $\mathbf{r}$ between the sphere and a detector point, but also on the polarization and wavelength of the incident light, the sphere radius a, and the relative index $m = n_\mathrm{p}/n_\mathrm{med}$, where n_p is the particle refractive index and n_med is the refractive index of the surrounding medium. Recalling the Equation 2.1 for the measured hologram intensity I in vector form:

$$\begin{aligned}I(\mathbf{r}) =& |\mathbf{E}_0 + \mathbf{E}_\mathrm{s}|^2 \\ =& |\mathbf{E}_0|^2 + \mathbf{E}_0\mathbf{E}_\mathrm{s}^* + \mathbf{E}_0^*\mathbf{E}_\mathrm{s} + |\mathbf{E}_\mathrm{s}|^2 \\ =& |\mathbf{E}_0|^2 + 2\mathfrak{Re}\{\mathbf{E}_0^*\mathbf{E}_\mathrm{s}\} + |\mathbf{E}_\mathrm{s}|^2,\end{aligned} \tag{2.27}$$

we may re-express it through the definitions of Eq. 2.26, and normalize the measured holograms by dividing by a background image of an empty field of view, which measured $|\mathbf{E}_0|$:

$$\begin{aligned}\frac{I}{|\mathbf{E}_0|^2} =& 1 + \frac{2\mathfrak{Re}\{\mathbf{E}_0^*\mathbf{E}_\mathrm{s}\}}{|\mathbf{E}_0|^2} + \frac{|\mathbf{E}_\mathrm{s}|^2}{|\mathbf{E}_0|^2} \\ =& 1 + 2\mathfrak{Re}\{\boldsymbol{f}(\mathbf{r})e^{ik(z-r)}\} + |\boldsymbol{f}(\mathbf{r})|^2.\end{aligned} \tag{2.28}$$

Analyzing holograms by fitting scattering solutions to them had several advantages over reconstruction techniques. First, it has a $\sim$ nm tracking precision (Lee et al., 2007) in the axial direction. The size of the particles can also be retrieved by fitting scattering models such as Eq. 2.28. Reconstruction methods require high computational cost to back-propagate light to many focal planes, in addition to complex particle-finding analysis, whereas fitting methods allow particle positions to be precisely determined from holograms in a single processing step. However, one great limiting aspect of fitting techniques is readily apparent: since the Lorenz-Mie solution strictly applies only to single spheres in an infinite, perfectly homogeneous medium, it is not clear how applied to holograms formed either by non-spherical particles or by multiple particles in close proximity, that is the main theme of this work. It is necessary therefore to extend this fitting paradigm to new types of scattering particles.

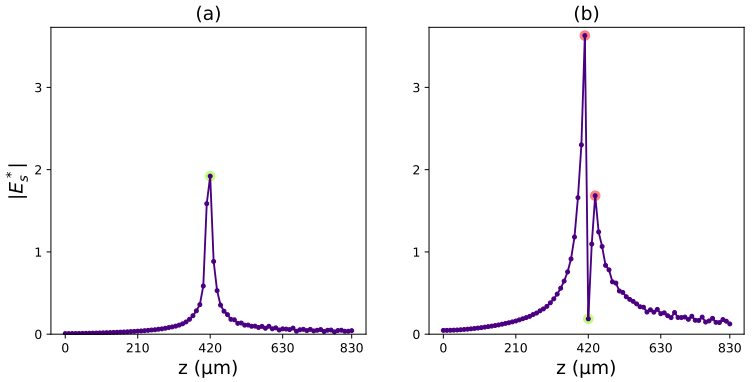

Figure 2.11: Reconstructions of simulated holograms. Line plots of the amplitude $|E_s^*|$ along z. (a) Polystyrene scattering sphere suspended in water, with radius $a = 1\,\mu m$; (b) strongly scattering polystyrene sphere in water, with $a = 2.5\,\mu m$. The plots are computed at the vertical and horizontal midplane of the $x - y$ lateral position, respectively. Green points denotes actual z position of scatterers, while the red points correspond to the external sides of the particle. Computational parameters: detector shape $= 821$ pixel^2, pixel size $= 0.26\,\mu m$, $\lambda = 0.633\,\mu m$, $z = 420\,\mu m$.

Returning to the reconstruction technique, there are some computational methods to avoid the mismatch of axial particle detection. Lets take a line plot of the amplitude $|\mathbf{E}_s^*|$ (Eq. 2.2) corresponding to the lateral $(x-y)$ position of the scatter along z. The plot exhibits a spike at the focal position z_0, whose amplitude depends on the nature of the particle (Goodman, 2005). We show this in Fig. 2.11 with a $1\,\mu m$-diameter polystyrene sphere (a), and $5\,\mu m$-diameter polystyrene sphere (b). The particles are the same simulated in Fig. 2.9. How we saw before, for the weaker scatterer the focal position is easily determined, and corresponds to the maximum of the line plot (green dot in Fig. 2.11 (a)). Instead, for the stronger scatterer, the focal position is located *inside* the object. Therefore the plot exhibits not one but two maximal positions (red dots in Fig. 2.11 (b)) interspaced by a local minimum (green dot in Fig. 2.11 (b)), that shows the actual focal position. To reconstruct the size of the particles we had to select the $x - y$ slice at z_0. In Fig. 2.12 we report the case for the $5\,\mu m$-diameter polystyrene sphere. Fig. 2.12 (a) and (c) show the slice at $z_0 = 410\,\mu m$ and $440\,\mu m$, the red maximal positions in Fig. 2.11 (b), respectively; while Fig. 2.12 (b) shows the slice at the actual focal position, $z_0 = 420\,\mu m$. By imposing a cutoff of 30% of the maximum of the intensity $|\mathbf{E}_s^*|^2$ we obtain (c), (e), and (f), respectively. The diameters found are $1.82\,\mu m$ (d), $4.94\,\mu m$ (e), $2.86\,\mu m$ (f). Keeping in mind this elongation in the axial direction, we can anyway obtain computationally the correct focal positions and the size of

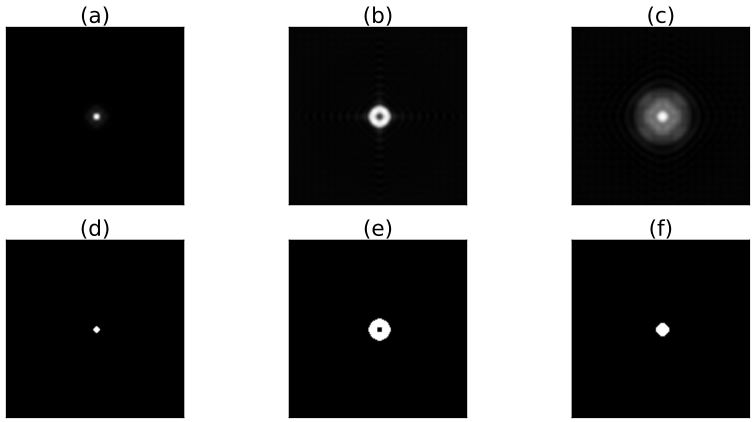

Figure 2.12: Slices in the $x-y$ plane of a strongly scattering polystyrene sphere in water reconstructions with $a = 2.5\,\mu\text{m}$. (b): Slice at the actual focal position. (a) and (c): Slice at the maximal positions found in Fig. 2.11 (b). By imposing a threshold mask in intensity we obtain (c), (e), and (f), respectively.

scatterers of any shape. In Chap. 3 we will discuss in further detail the object reconstruction algorithm.

2.5 Using holography to measure extinction and absorbtion cross-section

The interaction of a wave with a $\sim$ wavelength-scale particle causes a small attenuation of the original beam as the particle scatters and possibly absorbs part of the incoming radiation. *Extinction* is the overall effect that describes this power reduction, typically concentrated around the forward-scattering direction (Berg et al., 2008), and is quantified by the particle's extinction cross-section (C_{ext}) (Van de Hulst, 1957, Bohren and Huffman, 2008, Potenza et al., 2010). Since the hologram is a consequence of the interference between the scattered and transmitted field, the holographic pattern also contains information about the C_{ext} of the particle (Berg et al., 2014), independently by its shape.

Let us consider a particle of arbitrary shape and composition, embedded in a non-absorbing medium and illuminated by a light source, like a laser beam, at a large distance from the particle. We assumed the source be a linearly polarized plane wave traveling along the $\hat{\mathbf{k}}_0$ (z-axis) with wavelength λ, as shown in Fig. 2.13. The particle is exposed to an incoming field $\mathbf{E}_0 \sim e^{ikz-i\omega t}$, where $k = \frac{2\pi}{\lambda}$, and scatters light at all angles with the same time-harmonic dependence. Along the forward scattering direction, we put a detector, with planar size $\mathcal{S}_2$. We surround

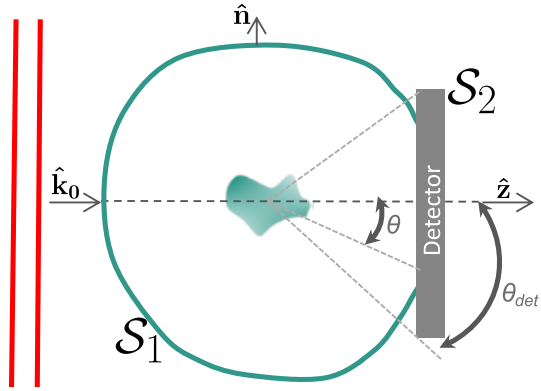

Figure 2.13: Geometry of scattering plane of an arbitrary particle showing the surfaces $\mathcal{S}_1$ (arbitrary) and $\mathcal{S}_2$ (detector), along with θ and θ_{det}. $\hat{\mathbf{k}}_\mathbf{0}$ represent the direction of propagation of the fields along the positive direction of the z-axis.

our particle with a large imaginary surface $\mathcal{S}_1$, and we call $\mathcal{S}$ the union of $\mathcal{S}_1$ and $\mathcal{S}_2$. In Berg et al. (2014), the authors state that measuring C_{ext} is equivalent to the difference of the net response of a detector looking into the light source without (I_0^{det}) and with (I^{det}) an arbitrary particle disturbing the incident wave. Throw the Poynting's theorem, with the same logic of 1.4.2, we can define them as

$$\begin{aligned} I_0^{\text{det}}(\theta) &= \frac{1}{I_i}\int_{\mathcal{S}_2} \left\langle \mathbf{S}_{\text{inc}} \right\rangle_t \cdot \hat{\mathbf{z}}\, da \\ I^{\text{det}}(\theta) &= \frac{1}{I_i}\int_{\mathcal{S}_2} \left\langle \mathbf{S} \right\rangle_t \cdot \hat{\mathbf{z}}\, da \end{aligned} \tag{2.29}$$

where $\left\langle \mathbf{S} \right\rangle_t = \left\langle \mathbf{S}_{\text{inc}} \right\rangle_t + \left\langle \mathbf{S}_{\text{sca}} \right\rangle_t + \left\langle \mathbf{S}_{\text{ext}} \right\rangle_t$. The first two terms involve the incident and scattered fields respectively, while the last term describes the energy flow due to the interference of these waves. Therefore, I_0^{det} is the total power received by the sensor due to the energy flow $\left\langle \mathbf{S}_{\text{inc}} \right\rangle_t$ and I^{det} to the energy flow $\left\langle \mathbf{S} \right\rangle_t$ integrated across $\mathcal{S}_2$, which subtends an angle θ_{det}, as shown in Fig. 2.13.
Recalling that for the law of conservation of energy

$$W_{\text{ext}} = W_{\text{sca}} + W_{\text{abs}}, \tag{2.30}$$

using the Poynting theorem we get

$$\begin{aligned} W_{\text{abs}} &= -\left[\int_{\mathcal{S}_1} \left\langle \mathbf{S} \right\rangle_t \cdot \hat{\mathbf{n}}\, da + \int_{\mathcal{S}_2} \left\langle \mathbf{S} \right\rangle_t \cdot \hat{\mathbf{z}}\, da\right] \\ W_{\text{ext}} &= -\left[\int_{\mathcal{S}_1} \left\langle \mathbf{S}_{\text{ext}} \right\rangle_t \cdot \hat{\mathbf{n}}\, da + \int_{\mathcal{S}_2} \left\langle \mathbf{S}_{\text{ext}} \right\rangle_t \cdot \hat{\mathbf{z}}\, da\right] \\ W_{\text{scat}} &= \int_{\mathcal{S}_1} \left\langle \mathbf{S}_{\text{sca}} \right\rangle_t \cdot \hat{\mathbf{n}}\, da + \int_{\mathcal{S}_2} \left\langle \mathbf{S}_{\text{sca}} \right\rangle_t \cdot \hat{\mathbf{z}}\, da \end{aligned} \tag{2.31}$$

Therefore the difference between I_0^{det} and I^{det} can be expressed as

$$\begin{aligned} f(\theta) &= I_0^{\text{det}} - I^{\text{det}} \\ &= \frac{1}{I_i}\int_{S_2} \left\langle \mathbf{S}_{\text{inc}} \right\rangle_t \cdot \hat{\mathbf{z}}\, \mathrm{d}a - \frac{1}{I_i}\int_{\mathcal{S}_2} \left\langle \mathbf{S} \right\rangle_t \cdot \hat{\mathbf{z}}\, \mathrm{d}a \\ &= \cancel{\frac{1}{I_i}\int_{\mathcal{S}_2} \left\langle \mathbf{S}_{\text{inc}} \right\rangle_t \cdot \hat{\mathbf{z}}\, \mathrm{d}a} - \frac{1}{I_i}\int_{\mathcal{S}_2} \left[\cancel{\left\langle \mathbf{S}_{\text{inc}} \right\rangle_t} + \left\langle \mathbf{S}_{\text{ext}} \right\rangle_t + \left\langle \mathbf{S}_{\text{sca}} \right\rangle_t \right] \cdot \hat{\mathbf{z}}\, \mathrm{d}a \\ &= \frac{1}{I_i}\left[W_{\text{ext}} + \underbrace{\int_{\mathcal{S}_1} \left\langle \mathbf{S}_{\text{ext}} \right\rangle_t \cdot \hat{\mathbf{n}}\, \mathrm{d}a}_{I_1} - W_{\text{scat}} + \underbrace{\int_{\mathcal{S}_1} \left\langle \mathbf{S}_{\text{sca}} \right\rangle_t \cdot \hat{\mathbf{n}}\, \mathrm{d}a}_{I_2} \right] \end{aligned} \tag{2.32}$$

Let us look the limits of this equation:

if $\theta \ll 1$ $\mathcal{S}_2$ approaches zero and $\mathcal{S}_1$ a closed surface surrounding the particle. $I_1 \approx -W_{ext}$ and $I_2 \approx W_{scat}$, therefore $f(\theta) \approx 0$.

if $\theta \gg 1$ $I_1 \approx 0$ due to this oscillation provided that $\hat{\mathbf{n}} \cong \hat{r}$ on $\mathcal{S}_1$ (Berg et al., 2014). I_2 decreases from its $\theta = 0$ value of W_{scat}.

With the same logic Eq. 2.32 can also be expressed as:

$$f(\theta) = \frac{1}{I_i}\left[W_{\text{abs}} + \underbrace{\int_{\mathcal{S}_2} \left\langle \mathbf{S}_{\text{sca}} \right\rangle_t \cdot \hat{\mathbf{z}}\, \mathrm{d}a}_{I_3} - W_{\text{scat}} + \underbrace{\int_{\mathcal{S}_1} \left\langle \mathbf{S}_{\text{sca}} \right\rangle_t \cdot \hat{\mathbf{n}}\, \mathrm{d}a}_{I_2} \right] \tag{2.33}$$

where:

if $\theta \ll 1$ then $f(\theta) \approx 0$.

if $\theta \gg 1$ $I_3 \approx W_{scat}$, since particles larger than λ typically scatter most strongly around $\theta = 0$, and $I_2 \approx 0$ for the same reason aforementioned. Therefore $f(\theta) \approx W_{abs}$ as θ grows.

In conclusion, $f(\theta)$, as θ increases from 0 to θ_{det}, shows a pattern that quickly rises from zero to a peak, then oscillates, and finally decays to an asymptote according to the nature of the scatterer: if the particle is non-absorbing, the curve will asymptotically approach zero (because $W_{\text{abs}} = 0$); if the particle is absorbing, the curve will approach W_{abs}. While, the average of f with θ over the domain where f oscillates approximates W_{ext} when extrapolated to $\theta = 0$. Therefore, based on Eq. 2.32 and 2.33, we get a measure of C_{ext} and C_{abs}.

In concrete terms, a hologram is proportional to the integrand of I_0^{det} in Eq. 2.29 evaluated at each sensor pixel, while the background, that is equivalent to a particle-free measurement, is proportional to the integrand of I^{det} in Eq. 2.29. Therefore, the operation $I_0^{\mathrm{det}} - I^{\mathrm{det}}$ is the same as integrating the *contrast hologram*, namely, the hologram pattern without the background. This procedure is sketched in Fig. 2.14. Three different cases are considered (panels a, b, and c): a non-absorbing sphere with $d = 5\,\mu\mathrm{m}$, m = 1.19; an absorbing sphere with $d = 5\,\mu\mathrm{m}$, m = 1.19 + 0.1i; and an aggregate of several particles of $d = 2\,\mu\mathrm{m}$, m = 1.19. The simulated particles produce three hologram patterns (Fig. 2.14 (d), (e) and (f)) that vary according to the scatterer morphology. Using the open-source package Holopy, we calculate the expected C_{ext} by computing scattered fields using Mie theory (g and h) and a T-matrix-based solution of scattering that accounts for multiple scattering between spheres (i). The $f(\theta)$ is plotted, normalized to the expected C_{ext} values, by integrating the pattern from its center to the edges. For this operation is crucial that the hologram pattern is with zero mean. The value of C_{ext} can be obtained by measuring the envelopes of the integration curve (black, dashed line in Fig. 2.14, panels (g), (h) and (i)), which define the average trend (pink, dashed line). For the absorbing sphere (h) and for large θ limit, the plot is asymptotic to C_{abs} (normalized by C_{ext}). While for non-absorbing objects (g, h) f approaches 0. In particular, the extinction cross-section of the aggregate is equivalent to $C_{\mathrm{ext}} = C_{\mathrm{ext,s}} \cdot N$, with $N = 6$ and $C_{\mathrm{ext,s}}$ the extinction of each particle aggregate, because they can be considered as a collection of independent particles (Sec. 1.4). In general, results show that this method works well for a large variety of particle sizes, shapes, and refractive index within ±10%, depending both by the maximal angle of detector of collection and by the intensity of scatterer (Berg et al., 2017). For example, for a 2.5 µm ray-particle as that in Fig. 2.14 (a) we obtain the extinction within 0.2% for $\theta_{det} \sim 11^\circ$ and 9% for $\theta_{\mathrm{det}} \sim 21^\circ$; while for a 1 µm ray-particle we obtain the extinction within 10% for $\theta_{\mathrm{det}} \sim 11^\circ$ and 5% for $\theta_{\mathrm{det}} \sim 21^\circ$. The results of the simulations are reported in Table 2.2.

2.6 Using holography to measure extinction via the Optical Theorem

As we see in Sec. 2.4, holograms can be modeled by fitting techniques, allowing reliable information about the size and optical properties of the scatterers. For sphere particles, in the forward direction at $\theta = 0$, the scattering wave superposed on the incident plane wave is a spherical wave, and the amplitude and phase are

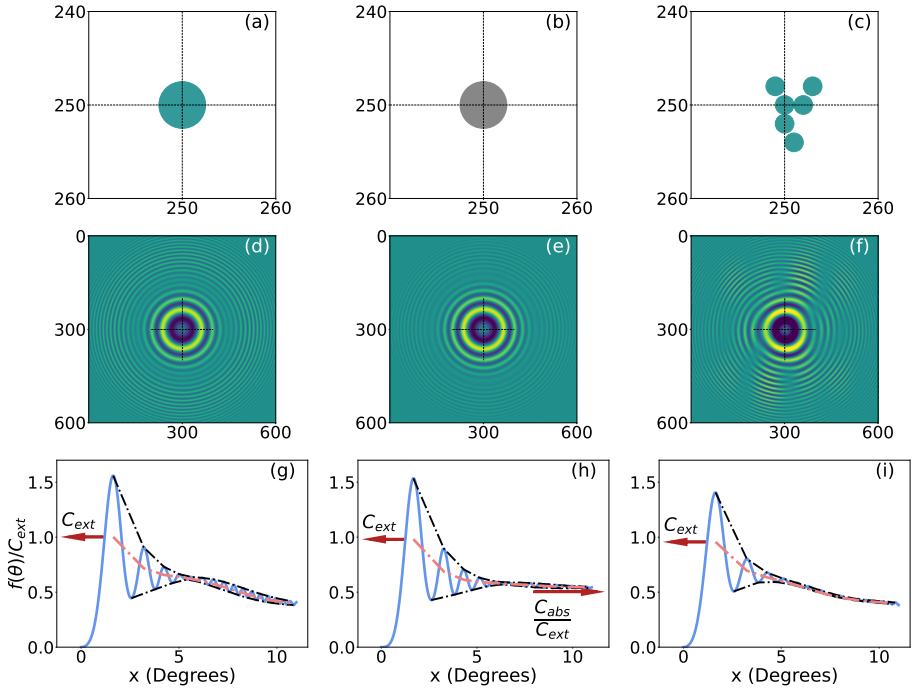

Figure 2.14: Examples of a general method to extract the extinction and absorption cross-section from a hologram in three simulated cases. (a) Non-absorbing sphere with $d = 5\,\mu\text{m}$, $m = 1.19$*; (b) absorbing sphere with* $d = 5\,\mu\text{m}$, $m = 1.19 + 0.1\text{i}$*; (c) six spheres aggregate of* $d = 2\,\mu\text{m}$, $m = 1.19$*. (d, e, f) Intensity plots of the corresponding holograms; the centered dashed lines correspond to the position of the dashed lines in the top images. (g, h, i) Integration of the corresponding holographic pattern, normalized to the* C_{ext} *value expected, by transition square matrix from the center of the pattern to the edges. The x-scale are in degree (*θ *in Fig. 2.13). Following integration, the endpoint of the trend curve (pink dashed line) corresponding to the first maximum gives the* C_{ext} *(red arrow), in good agreement with the expected value (approaches 1). For the absorbing sphere (panel h), the plot is asymptotic to the* C_{abs} *value (normalized by* C_{ext}*). We reported the output as a color gradient with the same scale (minimum value: -0.2 blue, maximum value: +0.2 yellow). Computational parameters: detector shape =* $601\ \text{pixel}^2$*, pixel size =* $0.26\,\mu\text{m}$*,* $\lambda = 0.633\,\mu\text{m}$*,* $z = 400\,\mu\text{m}$*.*

Panel	Quantity	Integral method	Mie Theory
a	C_{ext}	$41\,\mu\text{m}^2$	$41\,\mu\text{m}^2$
b	C_{ext}	$42\,\mu\text{m}^2$	$43\,\mu\text{m}^2$
	C_{abs}	$23\,\mu\text{m}^2$	$22\,\mu\text{m}^2$
c	C_{ext}	$58\,\mu\text{m}^2$	$60\,\mu\text{m}^2$

Table 2.2: Results of the simulations with the integral method for extracting extinction and absorption cross-section compared with the Mie Theory. The values are within 5%.

characterized by the amplitude function

$$S(0) = s(0)e^{i\sigma(0)} \tag{2.34}$$

The phase $\sigma(0)$ is independent of the choice of origin and of sign conventions for polarized light. Let (x, y, z) be a point in this plane, within the boundaries of 0. For this point, x and y are $\ll z$, so that

$$r = z + \frac{x_0^2 + y_0^2}{2z} \tag{2.35}$$

where (x_0, y_0) is the position of the scatterer on the plane and z is the position along the optical axis. In this way, from Eq. 2.28, we obtain:

$$\frac{I}{|\mathbf{E}_0|^2} - 1 = \frac{2s(0)}{kz} \cos\left(\frac{k}{2z}(x^2 + y^2) + \sigma\right) f(\theta) \tag{2.36}$$

where $f(\theta)$ is the form factor, the characteristic function of the interference pattern accounting for the intensity damping as the scattering angle increases. Therefore, we can fit the contrasted hologram, that is equivalent to the operation $I/|\mathbf{E}_0|^2 - 1$, with Eq. 2.36 obtaining the value of $s(0)$ and the phase shift σ. Finally, from the *Optical Theorem* (Eq. 1.4.2) we can obtain the value of the scattering cross-section as (Van de Hulst, 1957):

$$C_{\text{ext}} = \frac{4\pi}{k^2}\text{Re}S(0) = \frac{4\pi}{k^2}s(0)\cos\left(\frac{\pi}{2} - \sigma\right). \tag{2.37}$$

Fig. 2.15 shows an example of this analysis. Fitted holograms from spherical polystyrene (n = 1.58) particles in water (Fig. 2.15 (a), (c)) are compared to our experimental results (Fig. 2.15 (b), (d)). We used spherical polystyrene particles of $2\,\mu\text{m}$ (a, b) and $5\,\mu\text{m}$ (c, d) suspended in ultra-pure (Milli-Q) water; we normalized the intensity of the interference term to the incident field and reported the output as a color gradient (minimum value: blue, maximum value: yellow). In Figure 2.15, it can be seen that the oscillations vanish at the edges of the holograms, where the scattered wave vanishes. From the fit we obtained the values of the C_{ext} equals to $11\,\mu\text{m}^2$ and $44\,\mu\text{m}^2$, within 7% and 9% to the expected values, respectively.

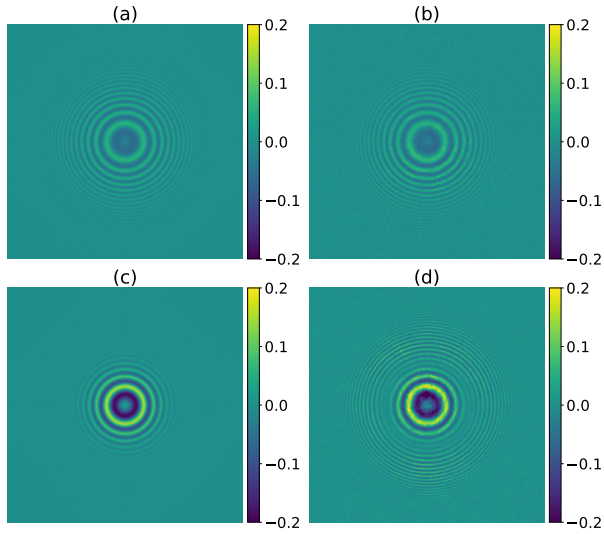

Figure 2.15: Result of fitted holograms (a, c) to experimental polystyrene spheres (b, d) of 2 µm *and* 5 µm *in diameter in water* ($n = 1.33$) *using the Lorenz-Mie formalism (Eq. 2.36). We reported the output as a color gradient with the same scale (minimum value: -0.2 blue, maximum value: +0.2 yellow)*

2.7 Quantitative three-dimensional imaging by phase contrast

Quantitative three-dimensional (3-D) imaging provides important information in many fields, especially in the study of biological specimens, such as living cells and their intracellular constituents since they are mostly transparent and therefore problematic for conventional bright-field microscopy. Off-axis digital holographic interference microscopy is an ideal tool for 3-D imaging, parameter extraction, and classification of living cells (Vora et al., 2017). Although in-line digital holography is the simplest of the common-path techniques, leading to compact setups using fewer optical elements and ensuring a great temporal coherence, it suffers from the reduction of field of view as only a portion of it contains useful information about the object. Moreover, in-line holography results in a superposition of the reconstructed object wavefront with a conjugate wavefront (the virtual twin image) and the intensity of the reference wave (the zero-order intensity). Thus, the reference beam may contain information about the medium surrounding the object, which may result in unwanted spatial phase variations. Therefore, an off-axis scheme has the potential to provide high-quality 3D images, as it can separate out the different diffracted components (non-diffracted reference, virtual object component, and

real-object component) in the frequency domain—only the frequency information about the virtual/real object is propagated—so there will not be any overlap between the three components in the reconstruction plane (Anand et al., 2011, Javidi et al., 2017). Summarizing, in quantitative digital holographic phase contrast microscopy, two aspects are of particular importance: (1) reconstructing the object wave without zero-order intensity and the twin image and (2) managing the phase aberration that is affected by the divergent object wave due to the application of a microscope lens. The first point can be obtained through a spatial phase-shifting (Carl et al., 2004, Liebling et al., 2004), while the second one is compensated by the use of double exposure, with and without the object.

Recalling that the intensity distribution I, located at the hologram plane, is formed by the interference of the object and the reference wave:

$$\begin{aligned} I =& |\mathbf{E}_0 + \mathbf{E}_\mathrm{s}|^2 \\ =& |\mathbf{E}_0|^2 + \mathbf{E}_0\mathbf{E}_\mathrm{s}^* + \mathbf{E}_0^*\mathbf{E}_\mathrm{s} + |\mathbf{E}_\mathrm{s}|^2 \\ =& |\mathbf{E}_0|^2 + |\mathbf{E}_\mathrm{s}|^2 + 2\sqrt{|\mathbf{E}_0|^2|\mathbf{E}_\mathrm{s}|^2}\cos\Delta\phi(x,y), \end{aligned} \tag{2.38}$$

we define the parameter $\Delta\phi(x,y) = \Delta\phi_0 - \Delta\phi_s$ as the *phase difference* between the two waves. In presence of a sample in the optical path the object-phase distribution is represented by the sum $\Delta\phi_s = \Delta\phi_{s_0} + \Delta\psi_s$, where $\Delta\phi_{s_0}$ denotes the pure object phase-shift and $\Delta\psi_s$ is proportional to the optical path length induced by the sample (Anand et al., 2011).
After the numerical propagation from the hologram plane to the object plane, we can obtain both the absolute amplitude and phase distribution of the scattered wave $\mathbf{E}_\mathrm{s}$:

$$\begin{aligned} \Delta\psi_s &= \Delta\phi_s - \Delta\phi_{s_0} \\ &= \arctan\frac{\mathfrak{Im}\{\mathbf{E}_\mathrm{s}(x,y)\}}{\mathfrak{Re}\{\mathbf{E}_\mathrm{s}(x,y)\}}(mod 2\pi) \end{aligned} \tag{2.39}$$

After removing of the 2π ambiguity by a *phase unwrapping process* (Kreis, 1996), the data obtained with Eq. 2.39 can be applied for quantitative phase contrast microscopy. Indeed, this phase difference is related to the object thickness through

$$\Delta\psi_s = \frac{2\pi}{\lambda}(n_p - n_\mathrm{med})h_i \tag{2.40}$$

where λ is the wavelength, z is the axial coordinate, h_i is the cellular thickness corresponding to the pixel i, n_p is the particle refractive index and n_med is the refractive index of the surrounding medium. Equation 2.40 can be used to determine either the thickness or the optical thickness, defined as $(n_p - n_\mathrm{med})h_i$.

Therefore, the object profile is directly obtained throw a phase imaging, and digital holography is a very effective process for achieving high-precision quantitative phase microscopy (Cuche et al., 1999a, Kühn et al., 2008, Kemper and Von Bally, 2008).

Chapter 3

Mineral dust characterization

The experimental setup is outlined in Fig. 3.1 and in Fig. 3.2. (a) Light from a visible laser source (He-Ne laser 5 mW, 633 nm, about 0.8 mm in width) is focused with a 20× objective, spatially filtered by a $\sim 30\,\mu m$ diameter pinhole (b), and collimated with a 4× objective lens. The pinhole filters the beam improving its spatial coherence and enhancing the quality of the holograms. The collimated beam impinges onto a quartz flow-cell (c) centered on the scattering volume (5×0.3 mm cross-section). A 20× microscope objective (d) is located in the far-field to reach the desired spatial resolution. Finally, the beam reaches a (e) CMOS detector (Ueye-5240CP-M-GL IDS Camera), illuminating its whole pixel array (1280×1024, 5.3 µm pixel size). The design of the instrument is simple and compact; its case is approximately 80 × 20 × 20 cm (Fig. 3.2). We operated in a cleanroom, and the custom table-top instrument is kept inside a laminar flow hood to prevent contamination of the samples. We examine light scattering data from dust particles once stored in ice cores from the cryosphere. Small portions of about $10\,cm^3$ were cut and isolated in sealed plastic tubes in a cold room (−20 °C). Coulter counter measurements have been performed immediately after melting at room temperature (∼24 °C) by the EuroCold research group at Università Degli Studi di Milano-Bicocca; then the samples are stored in a dark room at a temperature below 18 °C. The numbering of the sample is progressive starting from the first meter perforated, i.e from the most superficial portion of the core towards the depth, according to increasing numbers and correlated to the age of the layer. The age of each layer is expressed in *year before present* (KyBP), where conventionally the date assumed as *present* is 1951. By employing the digital holographic method for the analysis, the samples are transferred into a borosilicate glass container that serves as a reservoir; a steady stream of ∼1 ml min^{-1} is delivered to the illuminated region using a peristaltic pump. The samples were circulated through the instrument many times, up to some hundreds, in order to gather enough statistics. We acquired the images continuously in real-time (1280 × 1024, grayscale, 8-bit scale) with a frame rate of 27 $\#/s$ and an exposure time of 0.04 ms. We collected for each sample 38000 images; usually, this does not take more than ∼ 40 minutes for each measurement.

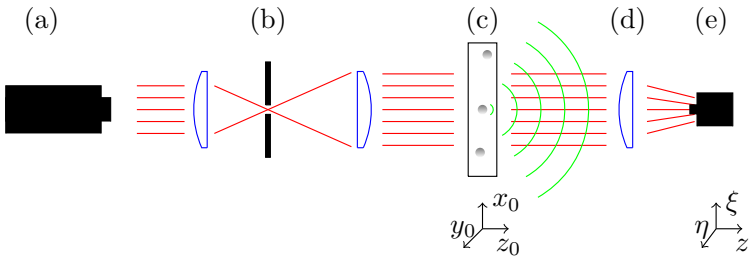

Figure 3.1: Diagram of in-line digital holographic microscopy. A laser beam (a) is focused and spatially filtered by a 30 µm *pinhole (b); the collimated beam illuminates a thin cell (c) through which particles (gray spheres) are flown. A* 20× *microscope objective (d) is located in the far-field of the sample, and a sensor (e) records the holographic pattern resulting from the interference of the faint scattered (green lines) and transmitted waves (red lines).*

Any small particle intercepting the laser beam scatters an almost spherical wave, which in turn interferes with the trans-illuminating field, similarly to in-line Gabor's holography (Gabor, 1948). The resulting self-reference interference pattern conveys information on both the amplitude and phase of the scattered field. An example of the output of the instrument is shown in Fig. 3.4.

Among the advantages of DH over other optical techniques is that the accurate alignment of its optical components is not critical, hence the setup is hardly affected by issues related to misalignment. Moreover, as it does not require time-consuming sample preparations, it is suited for in-line applications (Kaufmann et al., 2008, Bigler et al., 2011). Other factors contribute to the robustness of this method. Firstly, it is calibration-free, only needing a fine-tuning of the magnification (App. A). Secondly, it works well under strong dilution conditions (typically a limit for the static light scattering), hence it is particularly suited for polar ice core and snow samples. Low particle concentration in the samples prevents the overlap of waves from multiple dust particles. The main criticalities, such as the occurrence of multiple events, can be handled with custom-made software. For example, it is important to distinguish an aggregate from several separate particles, since the optical properties of these two morphologies are different even if the total mass is the same. In this regard, also the shape of the flow-cell is critical: the thicker it is, and the more likely it is to have particle detection on different focal planes. On one hand, this is discouraged as requires a high computational cost—to find the focal position we have to propagate the field from the hologram plane to the particle plane and it is time-consuming over $\sim 500\,\mu m$ with a personal laptop. Moreover, the overlap of the patterns from particles on multiple planes disturbs the

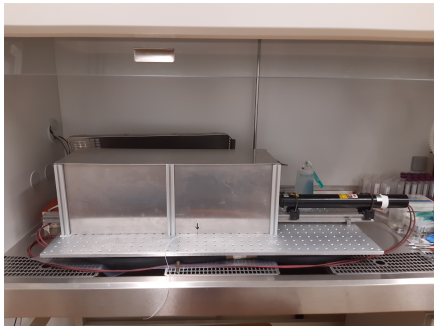

(a)

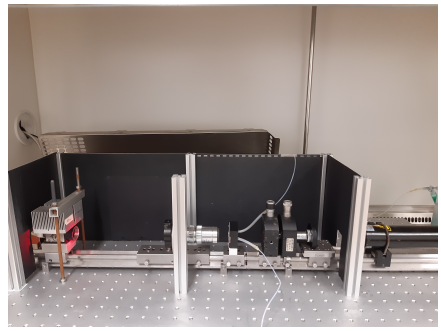

(b)

Figure 3.2: Photos of the custom instrumental setup kept inside a laminar flow hood at the EuroCold Laboratory at the Università degli Studi di Milano - Bicocca with its case (a) and without (b).

analysis. An example is shown in Fig 3.3, where a sample of polystyrene of 2 µm size-diameter is streamed through a cell of 1 mm of depth (along the optical view). The holographic patterns are very different due to the different focal positions and it is hard to mismatch the signals.

3.1 Image analysis and object reconstruction

After acquiring the images, the reconstruction is in post-process. An algorithm sets a threshold in the variance of the recorded images that allows detection if a particle falls into the field of view of the instrument. Since the amplitude of the scattered wave approximately decays as r^{-1}, the contribution of each scatterer is confined to a limited region of the image. Hereinafter, we refer to these regions of interest as *holographic features*: these need to be isolated from each experimental raw image and separately analyzed. As a pre-processing step, we form the *contrast hologram* $I_{\mathrm{c}}(\xi, \eta)$, which is produced after the normalization of the raw image with a background measurement, $I_{\mathrm{bg}}(\xi, \eta)$. This operation improves the hologram fringe contrast and eventual image. Since the background signal can vary slightly during the measurements, we compute a pixel-wise median to subtract the incident beam and suppress spurious contributions such as any laser intensity fluctuations. Each pixel of the resulting image is the median of the corresponding pixel in all images, over an interval range of 20 images. Thanks to the sample strong dilution, averaging we cancel each hologram patterns due to the particles that are driven through the scattering volume, obtaining a background image. The finals contrast hologram is

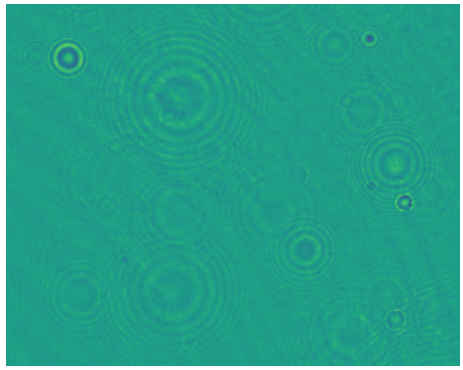

Figure 3.3: 2 µm-polystyrene beads streamed into a quartz flow-cell 1 mm thick (along the optical axis).

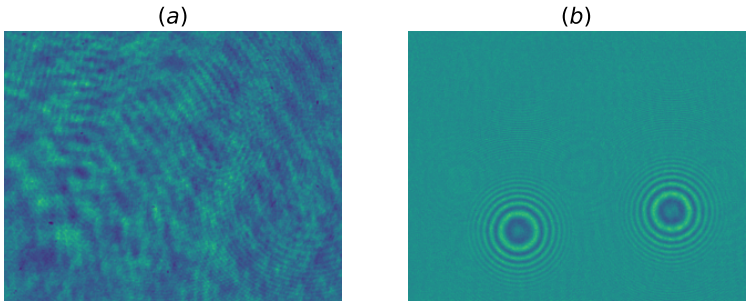

Figure 3.4: From the raw image (a) we subtract the background image and produce a normalized frame where the holograms are clearly distinguishable (b).

the result of the normalization

$$I_{\mathrm{c}}(\xi,\eta) = \frac{I(\xi,\eta)}{I_{\mathrm{bg}}(\xi,\eta)} \tag{3.1}$$

where $I(\xi,\eta)$ is the raw image recorded by the detector. Fig. 3.4 illustrates this process.

The second step is the *feature localization*. In each image, the center of the particle can be identified by performing a cross-correlation between the normalized hologram and a spherical function damping in intensity (see Eq. 2.36 and Fig 3.5, (a) and (b)). In this way, the hologram is transformed by the deconvolution into sharply resolved peaks (Fig 3.5 (c)), whose centers correspond to the position of the particle on the observation plane (Fig. 3.5 (d)). More than one distinguishable particle may appear in the same image. Given the importance of accurately finding

the center of the holograms on the (ξ, η) plane, we double-check it by implementing a Hough-based holographic feature detection algorithm (Krishnatreya and Grier, 2014). Following the approach of a Hough transform, the algorithm finds the pixel from which the most gradients point towards or away. Once this pixel is found, it uses a brightness-weighted average around that pixel to refine the center location to return. After the first center is found, the surrounding area is blocked out and another brightest pixel is searched for if more centers are required. Once the positions of the scatterers are retrieved, the original image is cropped to discard the portions of the image that do not include any fringes to reduce the computational cost (Fig 3.5 (d)). If an image includes many holographic features, it is divided into sub-images. Incomplete data are discarded: a threshold is set to disregard any hologram too close to the edges so that only image portions between 400×400 and 1000×1000 pixels are collected. Rejecting some events causes the apparent concentration to be slightly lower than the actual absolute concentration, an effect that can be compensated for.

The position of the scatterer on the (x_0, y_0) plane can be deducted directly from the hologram. Conversely, the position of the scatterer along the optical axis (z) must be reconstructed numerically. To do so, we propagate the wavefront recovered by the hologram ($\mathbf{E}^*_{\mathrm{s,hp}}$) to another position along the optical axis ($\mathbf{E}^*_{\mathrm{s}}$) (Schnars et al., 2015, Latychevskaia and Fink, 2015) by the Fresnel-Kirchhoff diffraction formula (Eq. 2.5). The original position of the particle along the optical axis (i.e. the focal point z_0) is indicated by an abrupt increase in the amplitude. We give an example of this method in Fig. 3.6: the amplitude exhibits a spike that indicates the presence of a particle (blue, dashed line). A threshold on the amplitude of the spike ensures that noise-related artifacts do not affect the retrieval. These steps are at the core of many-particle detection algorithms, some examples are given in Goodman (2005). An alternative method for particle detection is based on the spatial phase shift of the in-line hologram (Yang et al., 2006). Along the optical axis, the phase shift exhibits a $1/(z - z_0)$ singularity and a change in sign at the focal position, z_0, whereby it is possible to identify the position of the particle (see the red dashed line in Fig. 3.6).

Finally, having determined the position of the particle along the three axes, we are able to reconstruct the particle on the object plane and retrieve its silhouette, i.e. the cross-sectional area (*csa*), as follows. In Fig. 3.7 we can see some examples of the image reconstruction steps. Firstly, a threshold in amplitude is set to obtain a binary image, where "1" is the particle and "0" its (empty) surroundings. Here, a cutoff of 30% of the maximum of $|\mathbf{E}^*_{\mathrm{s}}|^2$ is used. In this way, we can label and recognize the different objects present in the images and obtain the *csa* of the particles (Fig. 3.7 (b, e, h)). Then, we check the first and second neighbors of each

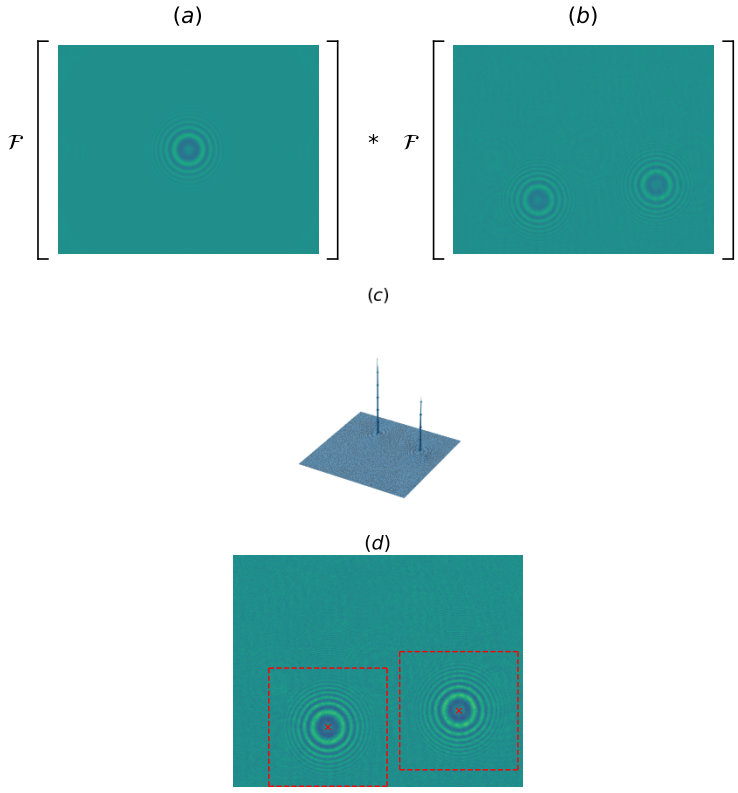

Figure 3.5: By the cross-correlation between a simulated hologram (a) and an experimental contrasted hologram (b), the hologram is transformed into sharply resolved peaks (c), whose centers correspond to the position of the particle on the observation plane (d). The final image is then cropped along the dashed red lines in (d) to discard the portions of the image that do not include any fringes.

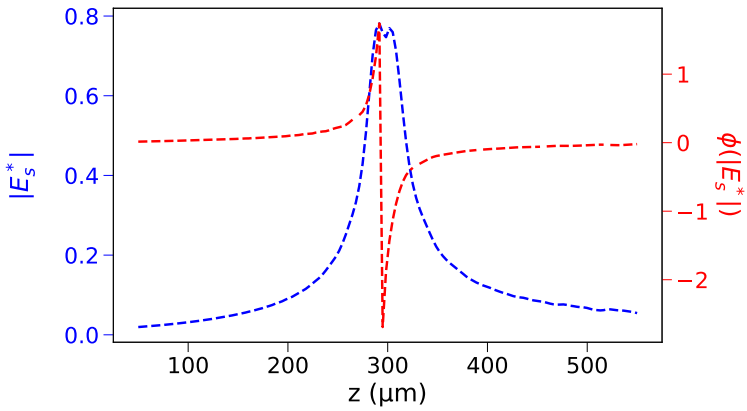

Figure 3.6: Numerical propagation of the field scattered by a polystyrene bead 2 µm *in diameter. At the focal position (z_0), the intensity (blue dashed line) exhibits a spike along the optical axis. Similarly, the phase shift along the optical axis (red dashed line) shows a $(z - z_0)$ singularity around the focal position.*

pixel: if there is at least one pixel within the second neighbor's range with the value "1", it is considered part of a single *cluster*. Cluster construction ends when the second neighbor's range returns zero pixels in all the ranges. An example of the recognition of two distinct objects is shown in Fig. 3.8. Finally, the images are processed with an edge detection algorithm that defines a contour enclosing each particle, designed to ignore regions affected by noise that causes the contour to be too small. If the algorithm identifies more than one particle, as in Fig. 3.10 (d, e, f), data are rejected to avoid artifacts that would lead to an overestimation of C_{ext}. It then computes a (possibly rotated) bounding rectangle around each particle. By computing the Euclidean distance between the midpoints of the rectangle, and multiplying by the pixel metric size, we obtain their cross-sectional height and width. The ratio between the major and minor axes gives the dimensionless aspect ratio (ar) (Fig. 3.7 (c, f, i)). In the special case where the two axes are equal ($ar \simeq 1$) we can uniquely define the dimensionless thickness (longitudinal axis along the optical axis) to *diameter* ratio (tdr). From the reconstructed images and the slopes of the major and minor axes, we can observe the orientation of the particles in the field of view and we can state that almost all ($\sim 90\%$) are oriented along the flow direction, as expected (Simonsen et al., 2018). The algorithm was validated with polystyrene microparticles, as described in Appendix A.

It is hard to precisely determine the particle throughput of the instrument. However, we can identify and discuss some limiting factors: (1) technological limits, and (2) methodological limits. The former is essentially due to the limited field of

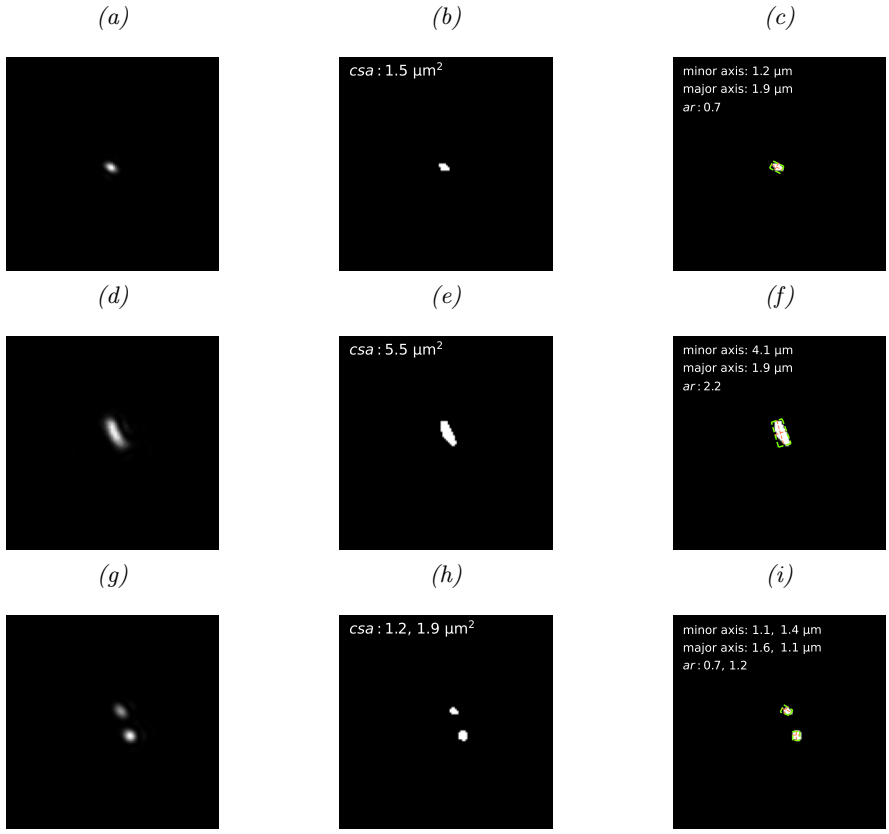

Figure 3.7: Examples of some mineral dust particles from Antarctica detected by the instrument (snowpits collected along the East Antarctic International Ice Sheet Traverse). From the contrasted hologram we propagate the field to the focal plane and we obtain the image of the particle (a, d, g). Then, by setting a threshold in amplitude we obtain the cross-sectional area (b, e, f). Finally, by computing a bounding rectangle around the particle (green dashed lines) we obtain the value of the cross-sectional height and width (red dashed lines) and their ratio (ar).

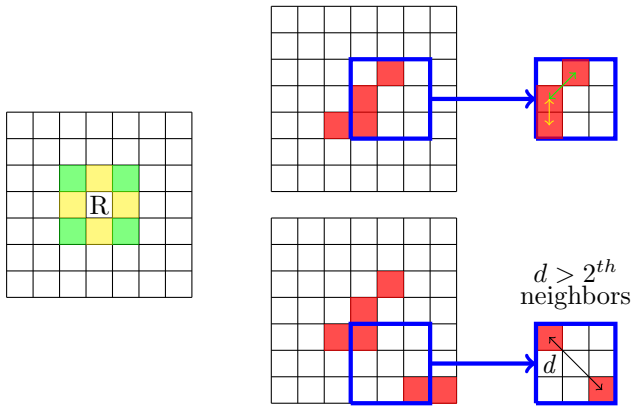

Figure 3.8: Left: structure with squared connectivity; the yellow boxes are the first neighbors; the green boxes are the second neighbors; R is the reference. Center, top: one cluster is recognized and labeled. Center, down: two clusters are recognized and labeled. Right, top: the distance between first neighbor (yellow arrow) and second neighbor (green arrow) whiting of a single cluster. Right, bottom: the distance between two clusters equals d, which is greater than the distance of the range of the second neighbor.

view of the camera, which currently is about 3% of the effective surface of the flow cell since we magnify the field with an objective lens. This does not introduce any instrumental biases and can be optimized with a larger sensor or a smaller flow cell (a wider field of view). The methodological limits are harder to compensate for and are mainly due to the signal-to-noise ratio: only particles with a $C_{\text{ext}} > 0.3\,\mu\text{m}^2$ can be analyzed successfully. Below this threshold, we cannot distinguish a very faint hologram pattern from an 'empty' image (with no particles in the field of view). We stress that this limit does not depend on the power of the laser, but rather on the extinction efficiency of the particle. Anyway, the working principle of the instrument makes it suitable for continuous flow analysis systems typically used in ice core characterization; this can be further eased by optimizing the camera field of view and the thickness of the flow cell.

3.2 Mineral dust content in snow

We now turn to the first part of the experimental results of this work. The experimental question we attempted to investigate is how does the shape of particles intercepting a laser beam affects their extinction cross-section. As regards the shape, the parameter we are interested in is the cross-sectional area (csa), and

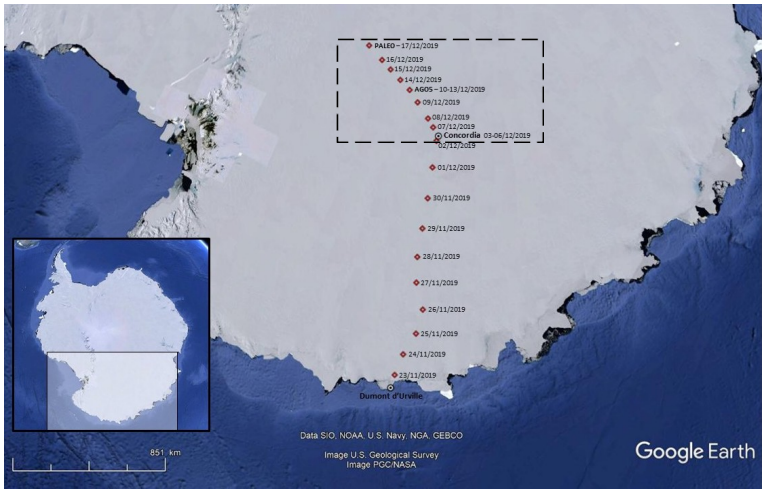

(a)

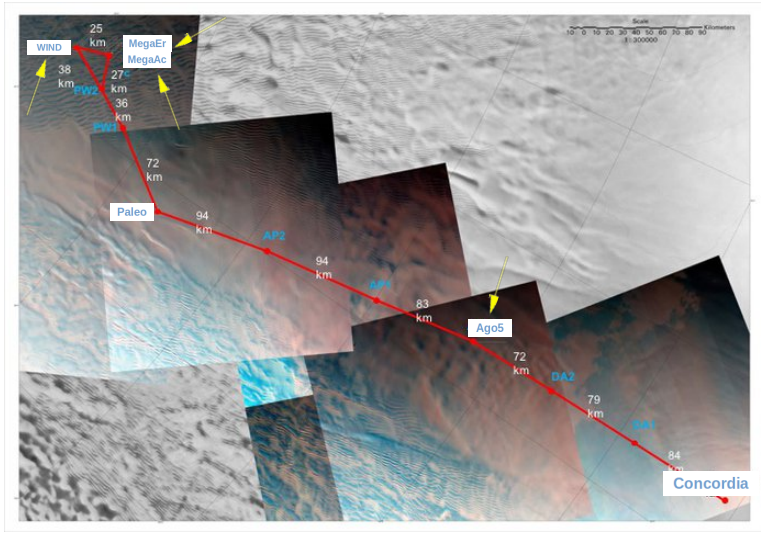

(b)

Figure 3.9: (a) Some of the stops planned by the EAIIST traverse during the 50-day expedition on the East Antarctic plateau, between Dome C (Concordia) and the geographic South Pole. (b) Zoom of the dashed rectangle in (a). On the 1670 km journey, the remarkable sites are labeled with yellow arrows.

the aspect ratio (*ar*), loosely defined as the ratio between the major and minor dimensions of the *csa*. The aspect ratio has values ranging from 1 for isometric *csa*, including both spheres and flat oblate-prolate spheroids, to ideally 0 for an infinitely thin *csa*. Moreover, for isometric *csa* we can obtain the ratio between the dimension of a particle and the width perpendicular to it, the dimensionless thickness to *diameter* ratio (*tdr*). In practice, it is common to encounter particles with $tdr \sim 0.3 - 0.4$.

We measured meltwater samples from snowpits collected along the East Antarctic International Ice Sheet Traverse (EAIIST project) across the East Antarctic plateau (Fig. 3.9), where dust concentration is very low ($\sim 10^2 - 10^3$ ppb). Samples (from the surface down to a depth of 175 cm depth) have been selected from five sites, which are: AGO5 (coordinate), mega dunes on the accumulation (MA), and on the erosion side (ME), and Wind Crust (WC, coordinate). These mega dunes formations (4 km long, few meters high) are structures generated in the interaction between the slope, wind direction, snow accumulation, and ice flow. The result is that the windward side loses mass, while the leeward side gains mass. Sampling over a very short distance of the accumulation and erosion part may allow measuring the influence of snowfall on the recording of climate parameters in the snow because only this parameter varies at the km scale mega dunes. We obtained the C_{ext}, *csa*, and *ar* as defined in the previous section. We observed a wide variety of particle shapes, as revealed by their silhouettes. Isometric and needle-like dust particles are most common (Fig. 3.10 (a), (b), and (c)), although we found some occurrences of aggregates of adhering particles (see Fig. 3.10 (e) and (f)). Generally, we observed a range of sizes from 1 to 20 μm^2 and a broad C_{ext} distribution (Fig. 3.11). Coulter Counter results reveal many mineral dust particles below the micrometric size range (0.5 µm – 1 µm approximately) that is inaccessible to our apparatus. However, with this study, we focus on the larger size range to better estimate the effects of shape. We don't observed highly absorbing particles (Appendix A.1).

The first thing to note is that no significant correlation between C_{ext} data and *csa* was found in any of the samples, which would instead be expected for sphere-like particles (see for example Fig. 3.14 below). In the histograms shown in Fig. 3.12, the area distribution of particles with isometric *csa*, obtained by the holographic reconstruction algorithm, is compared to the area distribution by inverting C_{ext} with spherical particles. The measured radius is ∼1.5 times that of the C_{ext}-equivalent radius. The spherical approximation distorts the distribution considerably, hence the importance of measuring two parameters simultaneously and independently. Similarly, trying to obtain the C_{ext} distribution from a volume-equivalent spherical model gives rise to discrepancies. In addition to optical extinction, information is needed about single-particle morphology, such as particle shape and orientation.

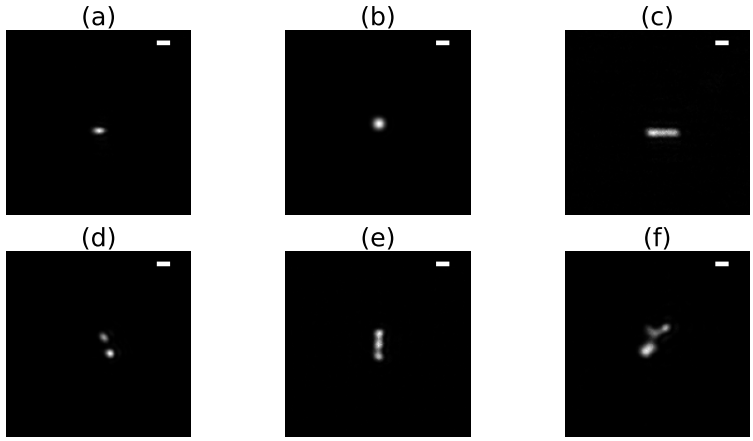

Figure 3.10: Examples of some reconstructed images from some contrast holograms. A wide variety of shapes (cross-sectional areas) is observed, although sphere and needle-like dust particles are most common (a, b, c). The white bar on the top-right corner of each image is set to $2\,\mu m$.

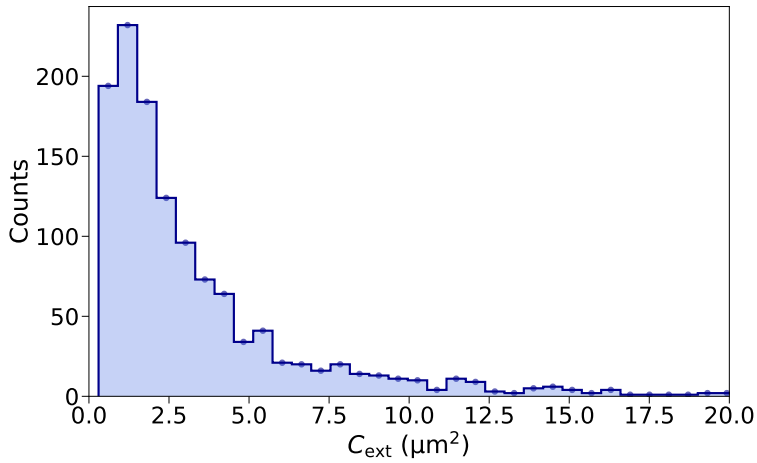

Figure 3.11: C_{ext} *distribution from AGO5 (depth* $69\,cm$*). The wide distribution covers a range of values from* 1 *to* $\sim 20\,\mu m^2$*. Larger sizes can be ascribed to aggregates and are discarded.*

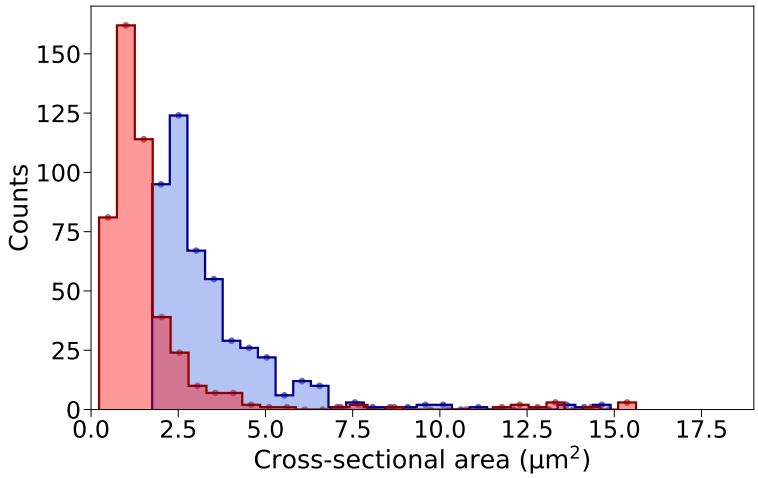

Figure 3.12: (Blue histogram) csa distribution for ME (depth 99 cm*) for isometric particles obtained from the reconstruction algorithm. (Red histogram) csa distribution for the same sample obtained from the C_{ext} distribution, interpreting particles as spheres.*

For example, flat particles cause a lower extinction of the incoming light compared to spheres for any given *csa*; it is crucial to take into account this feature in order to compare optical data to measurements of the volume of the particles (Simonsen et al., 2018).

Different sites exhibit considerably different shape distributions, as shown in Fig. 3.13, where we report the *ar* distributions of two samples from *ME* and *AGO5*, respectively. For *ME* at 99 cm depth (blue histogram in Fig. 3.13), a peak at around $ar = 1$ is clearly visible, a marker of isometric shapes, while the distribution of *AGO5* at 69 cm (green histogram) shows significant shape polydispersity. In order to compare the spherical model to our data, we consider the subset of particles whose *ar* approaches 1 (dashed columns in Fig. 3.13), and we plot C_{ext} vs area in Fig. 3.14. To compare to the expected curves for spherical particles, the C_{ext} of spherical particles were calculated with the open-source package Holopy. The expected refractive index of the particles in our samples is between 1.51 and 1.55 (∼1.14-1.16 relative to water), which is coherent with the expected Holocene dust composition observed at Dome C, mainly composed of plagioclase, feldspars, quartz, and phyllosilicates (Paleari et al., 2019). We chose 1.15 as an average value; the refractive index did not prove to be a critical parameter in this range, since variations in C_{ext} due to particles with different refractive indexes are negligible compared to the contribution of shape, specifically, to the distribution of *tdr* in

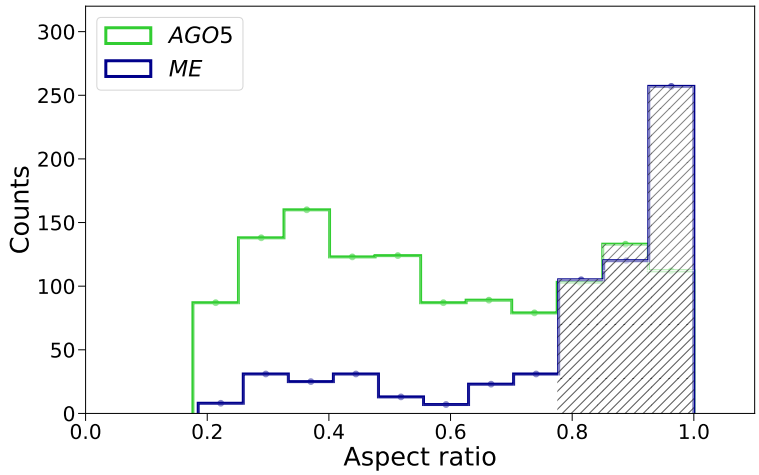

Figure 3.13: ar distribution from AGO5 (depth 69 cm*) and from ME (depth* 99 cm*). The dashed columns are the subset of particles whose aspect ratio approaches* 1*.*

the population of particles. In addition, we were able to assess that in the samples there are almost no particles characterized by high absorption such as combustion by-products, which are marked by an exceptionally high C_{ext} for any given size (App. A.1). We also note that low refractive index impurities such as bacteria give a low-intensity contrast in the images and do not pose a problem during measurements: repeating measurements after several hours gave consistent results. The solid black line in Fig. 3.14 is calculated with the Lorentz-Mie model for spheres with a diameter ranging homogeneously from 1.4 to 2.8 µm and a relative refractive index of 1.15. Particles that are nearly isometric fall close to this line. We include an uncertainty band in gray obtained for Mie calculations with a refractive index ranging between 1.14 and 1.16. We note that data appear appreciably spread out at any given size, and C_{ext} spans over an extended range ($\sim$ 1 order of magnitude). Such variability is attributable to the non-isometric shape of the particles. Specifically, our samples are dominated by flat (oblate) particles, whose C_{ext} is consistently lower than it is for spheres, or any equivalent isometric shape.

The extinction and scattering cross-sections of non-spherical particles can be calculated with the *Amsterdam Discrete Dipole Approximation* (ADDA) code (Yurkin and Hoekstra, 2011). The spheroid model allows a much more accurate modeling of scattered light from dust than that achievable through a model based on Mie spheres (Redmond et al., 2010). Each particle is discretized in many small sub-volumes (dipoles); the algorithm then calculates their interaction with a given incident electromagnetic wave. We used ADDA to determine the C_{ext} of oblate el-

lipsoids (1.15 relative refractive index) with a ranging thickness over diameter ratio (from $tdr = 0.1$, turquoise dashed line, to 0.9, dark green dashed line in Fig. 3.14), and we compared to our distribution, labeling the particles with the same range of color. Some data points in the top-left corner of the plot lay well above the Mie curves at very high values of extinction. The former are reported as purple points in Fig. 3.14 and are about $5-6\%$ of the total counts, and are essentially due to particles with a non-negligible absorption cross-section. Some of these events arise when many particles located at different z coordinates occupy the scattering volume and only one of them is tracked by the reconstruction algorithm. While the other particles still contribute to the total extinction, the contrast of their holograms is too low and the estimate of the particle size is altered. However, these events are statistically negligible due to the low concentration of the samples.

By comparing the C_{ext} of oblate ellipsoids with our data, we can obtain the distributions of *tdr* from the subset of particles whose *ar* approaches 1 (Fig. 3.15). In doing so, we can also implicitly use the fact that the majority of particles orient themselves orthogonally to the optical axis. The shape of the final distribution does not have a peak around 1 (a trait of isometric particles) but extends over a wide range with a prevalence of $0.2-0.4$ *tdr* (plate-shaped particles). Moreover, the distributions in Fig. 3.15 exhibit a similar trend, showing a comparable presence of plate-shaped particles. Once obtained the thickness of the particles, we can univocally determine the volume. At any given volume, the observed (oblate) particles with $tdr = 0.1$ have an extinction 1/3 times that of the equivalent spherical particles. As the *tdr* value increases, the oblate particles have a C_{ext} that tends to that of equivalent spheres ($\sim$1.1 times for $tdr = 0.6$ and 0.8 times for $tdr = 0.8$), as expected.

We summarize our results in Figure 3.16, where we include all the samples, selected so as to cover a variety of depths for each of the five sites. We show the parameters described above for each sample: the C_{ext} (a), the *csa* (b), and the *tdr* (c). The data points in the plot are the medians of the respective optical and geometrical distributions. Broad distributions characterize both the area and the C_{ext} but appear to be homogeneous among the different sites. We obtained the *tdr* distributions for all the samples that show a consistent number of particles whose *ar* approaches 1. The plot underlines the prevalence of a principal *tdr* range between 0.15 and 0.4. The gray regions in Fig. 3.16 highlight samples close to the surface that are exposed to contamination and are therefore excluded from the following analysis.

In Fig. 3.17, the particle counts for each sample are reported in comparison with Coulter Counter results. In order to compare the two analyses, we select the same range of cross-sectional area, from 1 to 20 μm^2. Some volcanic events have been

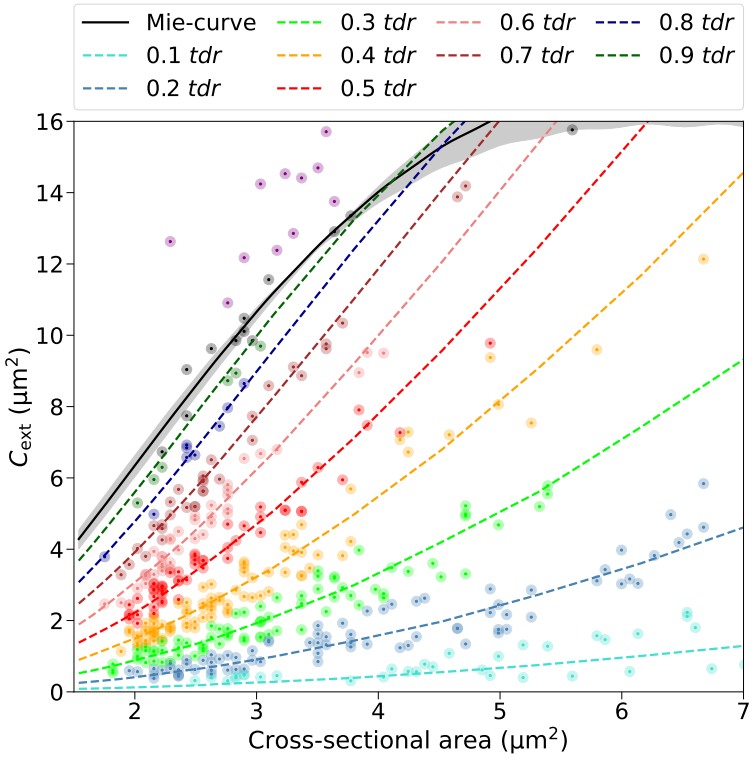

Figure 3.14: csa according to the extinction cross-section for a ME sample (depth 99 cm*). The solid black line is the Mie curve for spheres (*1.15*). The colored lines refer to the simulated extinction cross-section of oblate ellipsoids (*1.15 *refractive index) with a ranging thickness/diameter (tdr) from* 0.1 *(turquoise line) to* 0.9 *(dark-green line). The experimental data points, whose color indicates the tdr as in the corresponding dashed lines, are a subset of particles whose aspect ratio on the $\xi\eta$ plane approaches* 1.

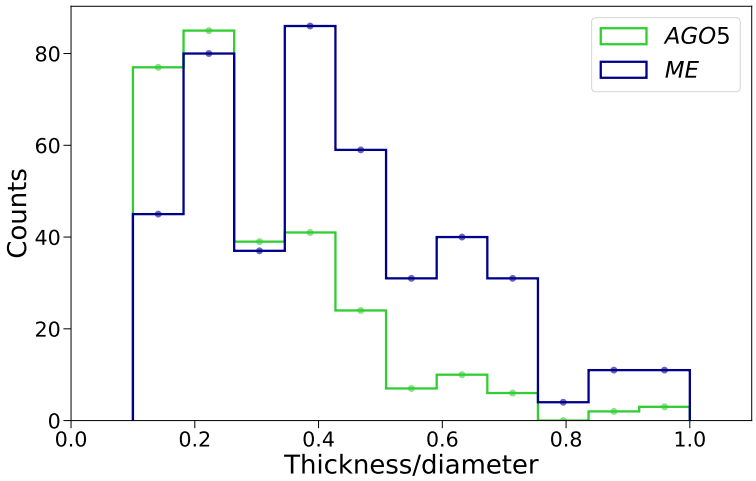

Figure 3.15: tdr distributions obtained by comparing the simulated C_{ext} of oblate ellipsoids (with isometric cross-sectional ar) with our data from AGO5 (depth 69 cm*), and from ME (depth* 99 cm*).*

identified in several sites at different depths (i.e. in samples MA 233-234, ME 227-229, and AGO5 20-23, as can be seen by the dashed blocks in Figure 3.17), from both DH and Coulter counter data. These events are marked by a very high particle concentration, especially at small diameters $\lesssim 1.5/2\,\mu$m, as revealed by Coulter Counter measurements. We do not have access to this size range due to the size limit of the holographic instrument presented here; however, we still notice a particle concentration anomaly in the larger size range. Moreover, we observe a large number of aggregates resulting from the increased probability for two particles to collide and stick together. Even if the absolute counts differ due to the different sensitivities of the two instruments, we can state that Coulter Counter and holography measurements are in good accordance, especially for samples not close to the surface or with volcanic events (dashed boxes in Fig. 3.17). These events are characterized by a very high particle concentration at small diameters, therefore here the measures deviate cause to the size limit of the holographic technique at this range. We notice the particle concentration anomaly, but mainly in the larger size range.

Finally, in Fig. 3.18, we show the average concentration of the five sites compared with Coulter Counter results, which deserve some further considerations. We show the results sorting the sites by the impact of wind erosion, increasing from left to right. To exclude possibly contaminated samples and anomalies, here we do not include samples containing volcanic events nor samples close to the surface. We

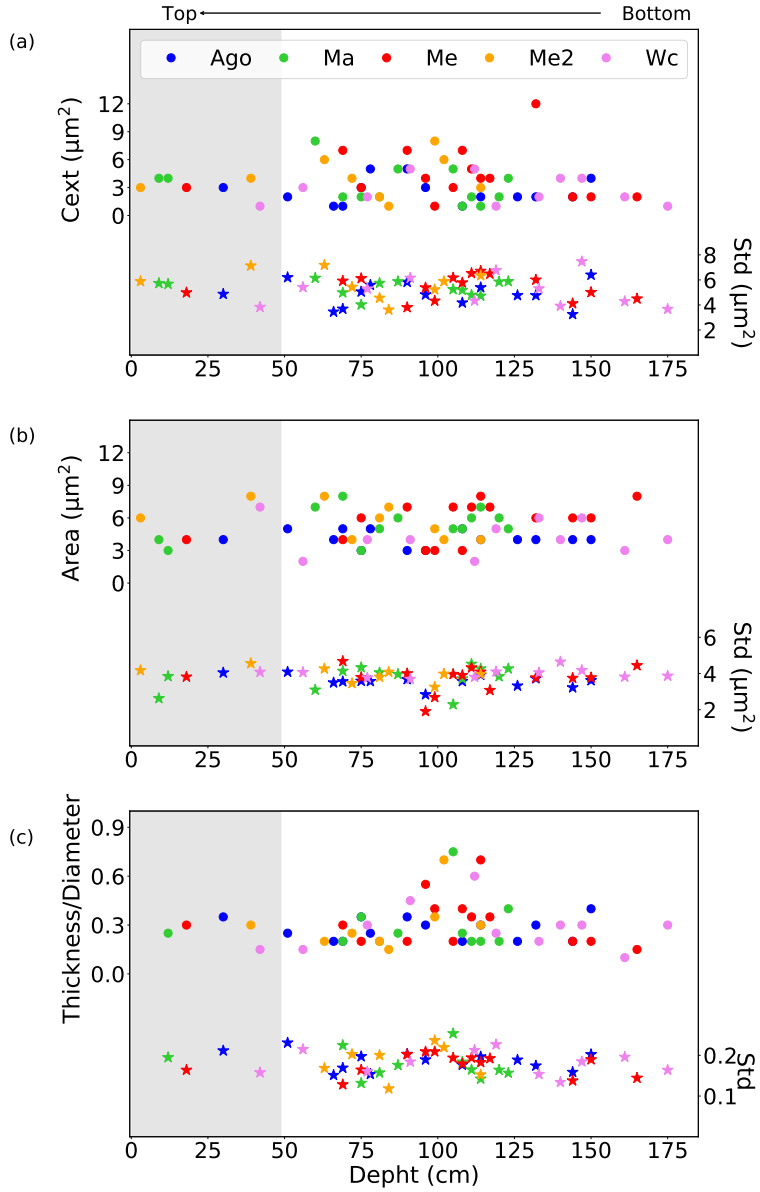

Figure 3.16: Summary of the results reported as a function of sample depth in cm. (a) C_{ext}, (b) csa, and (c) tdr distribution of each sample (circles, left y-axis) and standard deviation (stars, right y-axis). Sites are color-coded: blue for AGO, green for MA, red for ME, orange for ME2 (another sample site of ME2), and violet for WC. The gray regions highlight samples close to the surface.

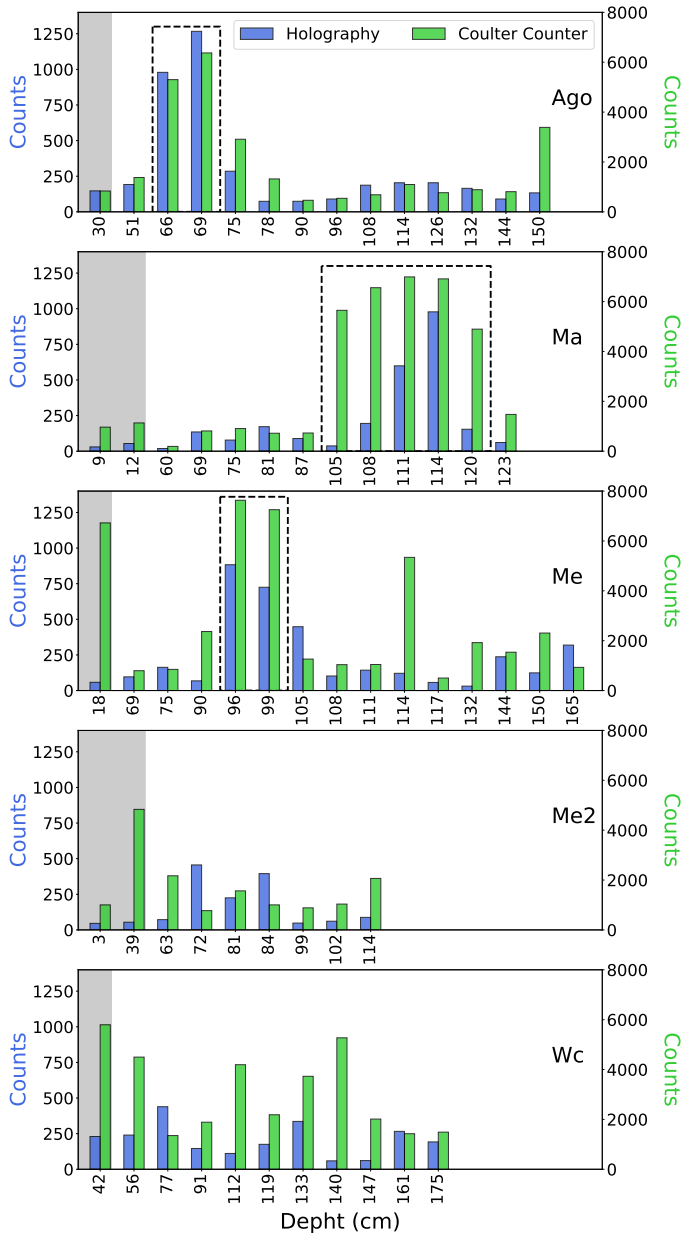

Figure 3.17: Particle counts as a function of sample depth in cm. The left y-axis refers to the holography measurements, whereas the y-axis on the right refers to Coulter Counter measurements on the same size range. The gray regions highlight samples close to the surface, while the dashed boxes represent the volcanic events. The absolute counts differ due to the different sensitivities of the two instruments.

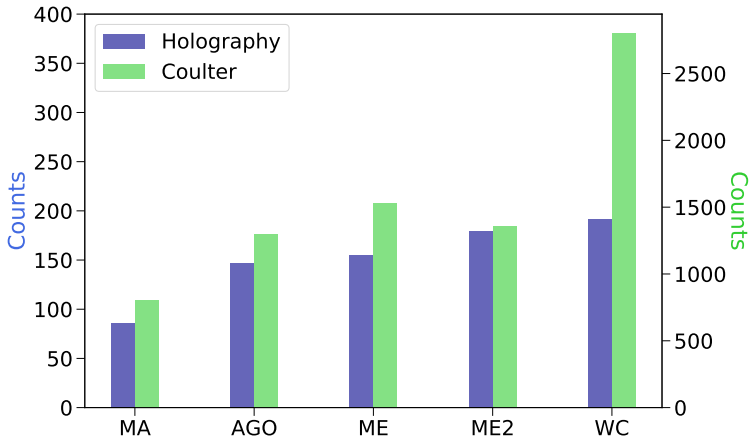

Figure 3.18: Comparison of the average particle counts for the five sites, excluding volcanic and superficial regions. The left y-axis refers to the DH measurements, whereas the y-axis on the right refers to Coulter Counter measurements on the same size range. The absolute counts differ due to the different sensitivities of the two instruments.

point out that comparing Coulter Counter and DH results for particle concentration and size distribution is not straightforward, as the physical quantities measured by these two methods are different. Here we set an approximate threshold in size to compare the two results, from 1 to 20 μm^2, but this is intrinsically blurred by the fact that the Coulter Counter gives a volume-equivalent diameter for each particle, whereas holography gives a cross-sectional area. The relationship between these two quantities is not trivial, as it clearly follows from Figure 3.14. This is more evident in the WC samples, which have $\sim$3 times the particle counts than the other sites. WC site is especially subject to sublimation by the wind while not exhibiting appreciable erosion, which produces crusts and alters the dust content, enhancing post-depositional aggregation. Anyway, we notice a distinct rise in dust concentration due to snow sublimation caused by the wind, in agreement with Coulter Counter measurements.

3.2.1 Alpine snow samples

Similar results can be found studying airborne particles from meltwater Alpine snow samples. We report briefly, as an example, three samples from the Rutor Glacier (2500 m - Aosta Valley, Italy) as representative of the majority of particles from this site with three-year historical series of snow cores, from 2015 to 2019.

Snow samples are collected by digging a trench and then are stored in vials, with a drilling system up to ∼4 m of depth. Alpine ice or snow samples are characterized by an elevated dust concentration and are considered to be highly sensitive to climatic and environmental conditions. First, they are composed of mineral dust from the deflation of local mountains. Moreover, a large amount of mineral dust can be transported long-range from North Africa due to Saharan dust storms, which are the world's largest source of aeolian desert dust and have significant direct and indirect radiative effects. Opposite to Antarctic samples, a great contribution is also due to anthropogenic sources, with a prevalence of carbonaceous particles. Elemental carbons are relevant due to their high absorption and are one of the most important anthropogenic constituents to global warming after CO_2 (Jenk et al., 2006). In the melting season, there is also a large release of micro-algae, microorganisms, and bacteria that can form a patchwork of red, green, or orange snow that covers large superficial areas (Hoham and Remias, 2020). The presence of micro-algae has important implications for snowpack stability, melting, and biogeochemistry (Courville et al., 2020) because they amplify the rate of snow loss by decreasing snow surface albedo. Finally, other contributions are derived from pollen and local vegetation, which are useful for the study of the response of terrestrial environments to climate change over the past age (Yang et al., 2010).
Light-absorbing impurities such as mineral dust, volcanic ash, algae, carbonaceous particles, or pollen influence the snow albedo and alter the radiative balance of snow and ice, enhancing the surface melting, exposing darker surface and reducing the snow cover. Experimental data and SNICAR[1] model simulation analysis suggest that the presence of mineral dust depositions strongly decreases the albedo in the visible wavelengths, especially for coarse ($3-5\,\mu m$ in size) and giant ($>10\,\mu m$) particles (Di Mauro et al., 2015), and reduce the reflectance of $80-90\%$ (Di Mauro et al., 2017). The radiative parameters of dust are indeed strongly dependent on particle size (Tegen and Lacis, 1996). This is more evident in the Alpine ice cores, where the dust concentration is higher than the Antarctic ice cores. It has been found that not including the coarse and giant particles in atmospheric models over the Sahara resulted in an overestimate of the single scattering albedo by up to 0.11, with an associated increase in atmospheric heating by 3 times (Ryder et al., 2013). Furthermore, in the long-wave spectrum, larger particles more than double the long-wave aerosol optical depth (Otto et al., 2011). In conclusion, giant particles can change the sign of the net radiative effect of dust and the impact of dust on atmospheric circulation. Therefore, it is important to give an accurate estimation of dust particle size distribution across all sizes.

[1]The Matlab version of the code is openly available at `https://github.com/mflanner/SNICARv3`. The model provides simulations of snow spectral albedo and has been largely used as a reference in snow spectroscopy and radiative transfer.

By our analysis, we found particle counts with two orders of magnitude greater than Antarctic samples, both in the fine and coarse size range. This can be associated with the varied micro-particulate sources and the higher precipitations. Moreover, we observed a great number of aggregates, especially in 2016, probably due to a melting process. Some examples are shown in Fig. 3.19. The in situ formation of dust aggregates is due to a relocation of the impurities and represents a critical indication for post-deposition processes. They are recognized due to the anomalously large dust size distribution, sometimes partially separated by voids and labeled as multiple different clusters. As consequence of the varied dust compositions, the refractive index of the particles has a large range between 1.47 and 1.60 (∼1.10-1.20 relative to water). We choose again 1.15 as an average value: variations in Cext due to particles within this refractive indexes range are almost negligible compared to the contribution of the size. We found in general that the cross-sectional area spans over an extended range, from 1 to 25 µm^2, and the extinction cross-section from 0.3 to 30 µm^2, which is in marked contrast to the ideal case of spherical particles, as can be seen in Fig. 3.20. Some occurrences have higher C_{ext} values ranging between $150 - 200\,\mu\text{m}^2$ and cross-sectional diameters of $20 - 30\,\mu\text{m}$, due to the aggregation of particles. We exclude the presence of algae due to the sample depths. Anyway, the microbial dust-associated during the deposition have a low-intensity contrast in the images, and therefore can not be detected through the analysis.

The modal value of *csa*, C_{ext}, *tdr* are reported in Table 3.1, excluding the aggregate particles. In 2015 and 2016 we obtained smaller values of C_{ext} ($< 1\,\mu\text{m}^2$), while the *csa* are almost homogeneous among the years, with small *tdr* modal values (< 2). We found the 8% average of giant particles, defined as particles with a cross-sectional diameter $> 10\,\mu\text{m}$. The particle count in 2019 is about one order of magnitude less than the snow samples collected in 2015 and 2016, which probably experiment some melting processes, or were contaminated after the drilling. We make the point that with digital holographic technique we are not able to detect melt events in the past, but these events have always as consequence a rise in the particle concentration, especially in the aggregate form, that can be detected. Finally, in Fig. 3.20 (b) we note also a higher number of particles that lay above the Mie curve. This can be attributed to the presence of prolate samples or particles with a non-negligible absorption. The work is currently in progress to quantitative characterize such features.

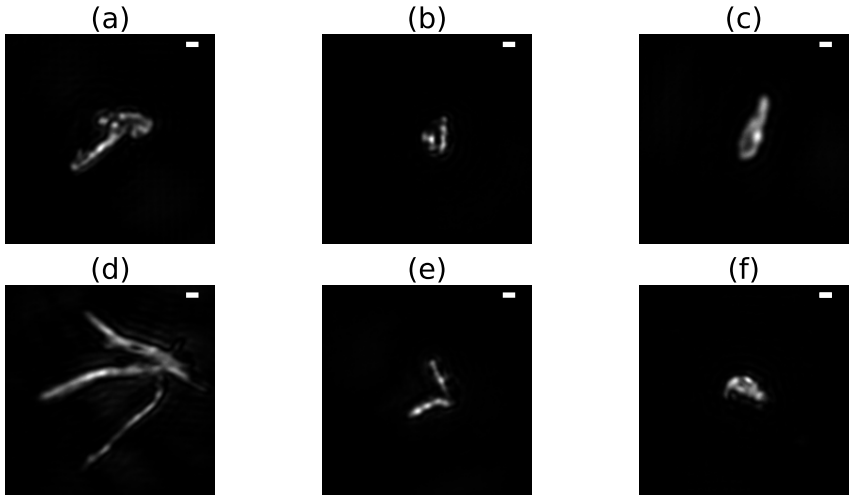

Figure 3.19: Reconstructed images of some impurities and aggregates relating to Alpine sample from Rutor Glacier, 2500 m *- Aosta Valley, Italy. The white bar on the top-right corner of each image is set to* 2 µm*.*

Age (y)	C_{ext} (µm^2)	*csa* (µm^2)	*tdr*	Counts (#)
2015	0.6	4.5	0.2	10507
2016	0.9	3.2	0.3	17677
2019	2.7	4.0	0.2	2570

Table 3.1: Optical and size characterization of the Alpine snow core samples chosen for the analysis. The C_{ext}, csa, ar, tdr values are the modal values of the distributions, excluding the aggregates particles.

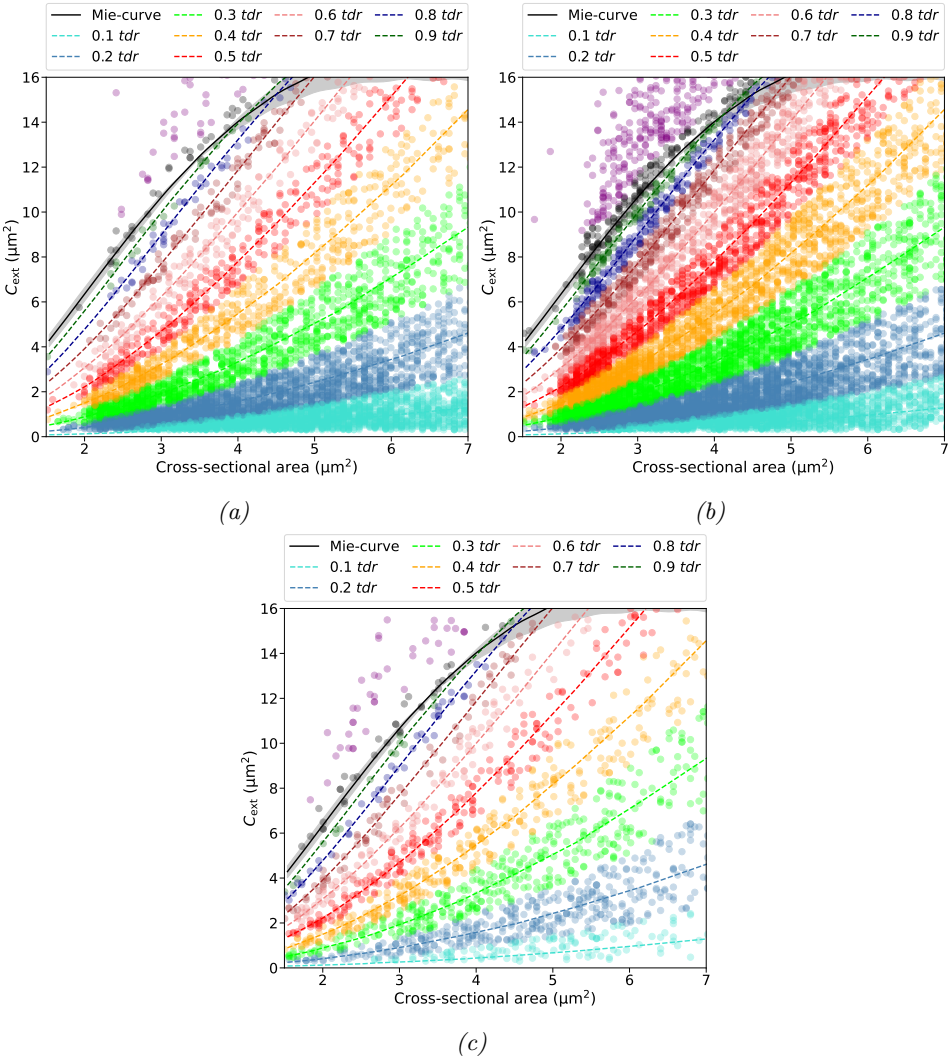

Figure 3.20: csa according to the extinction cross-section relating to Alpine samples from Rutor Glacier, 2500 m *- Aosta Valley, Italy, 2015 (a), 2016 (b) and 2019 (c). The colored lines refer to the extinction cross-section of oblate ellipsoids defined as in Fig. 3.14.*

Figure 3.21: Map of Antarctica marked with the location of Roosevelt Island, an ice dome between two submarine troughs carved by paleo-ice-streams in the Ross Sea, Antarctica [79°25'S 162°00'W]. The RICE ice core was drilled on the ice divide of Roosevelt Island.

3.3 Mineral dust content in ice cores

We devote this chapter to the study of deeper ice samples from a new, annually dated, ice core record from the eastern Ross Sea. The ice core was extracted as part of the Roosevelt Island Climate Evolution (RICE) project (2010–2014) and adds information on past accumulation changes in an otherwise poorly constrained sector of Antarctica (Fig. 3.21). The RICE project seeks to provide new information about the past configuration of the West Antarctic Ice Sheet (WAIS) and its retreat during the last deglaciation, thus improving estimates of its contributions to future sea-level rise (Lee et al., 2018). As shown in Fig. 3.22, with a recovered of ∼764 m of ice core, depth where the glacier comes into contact with the bedrock, it will be possible to formulate hypotheses on the possible climatic conditions of Antarctica and the Southern Ocean in the last 80000 years (BP) (Winstrup et al., 2019). In this work, we focus on the Holocene age (11.7 kyBP-today), and the sampling is shown in Fig. 3.22 by the rainbow-colored dots. Typical Holocene average values of the dust concentration between 600 nm and 18 µm are around 20-25 ppb, while in the glacial ages can rise to an average of ∼ 110-120 ppb. Indeed, the end of each glaciation is associated with an increase of the sea level and an intensified hydrologic cycle, thanks to higher humidity and water precipitation, together with a greater vegetation coverage as well an increased rate of snow and ice accumulation over the Antarctic ice sheet. All of these factors reduce the deflation of mineral

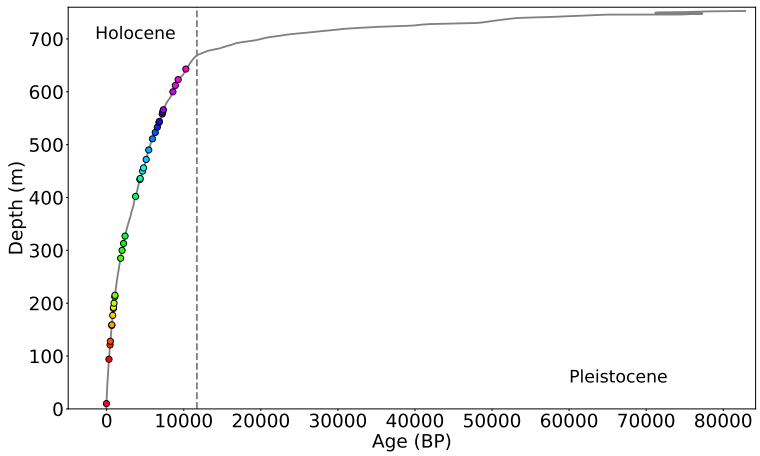

Figure 3.22: Temporal range coverage by the ice core obtained by the perforation at the Roosevelt Island. The colored dots are the sample analyzed with the holographic technique, that well sampling the Holocene age.

dust and hence their concentrations recovered in ice. In RICE the Holocene extends up to 600 m, covering most of the extracted core. Typical Holocene concentration levels are indeed reached at depth of ~ 682 m, corresponding to about 14.6 kyBP. Therefore, the Holocene age in the RICE ice core has a particular high temporal resolution with a constant sampling of ~ 15 cm in comparison to the deeper portion of the core to date to the Glacial period. The analysis has been performed in close collaboration with the EuroCold Laboratory[2], who provided Coulter Counter measurements and optical microscope observations, which confirmed the presence of possible aggregates and the sporadic presence of diatoms and sponge spicules, still under interpretation. Coulter Counter measurements showed that, for the Holocene age, volume-equivalent diameters of the particles typically range between 0.5 µm and 2 µm (fine grain range), with some occurrences up to 10 µm, and a mean concentration equivalent to 24 ppb. We performed an optical and size characterization of the insoluble particulate embedded in the ice in accordance with the depth of the ice core. Here we show the preliminary results, that will be included in a wider spectrum of analysis already in progress and future. For each sample we obtained the value of C_{ext}, *csa*, *ar*, *tdr* and counts, as defined in the previous section, which we reported the modal values in Table 3.2. In Fig. 3.23, we show three examples of the *csa*-C_{ext} distributions at different depht, represented as two-dimensional histograms and normalised on their maximum (dark blue). Fig. 3.23 (a, c, e) display

[2]A substantial portion of the contents of this section follows from the work undertaken with Dr. Sofia Cerri and Dr. Serena Lagorio, who performed the Coulter Counter measurements.

all the particles present in the samples, while Fig. 3.23 (b, d, f) only a subset of particles that show a symmetrical *csa* ($ar > 0.8$). We note that the particles show distributions on the plane which are almost identical both for symmetrical *csa* and not, attributable only to the distribution of non-spherical particles. In Fig. 3.24, we summarize our results including all the samples in function of depth, selected so as to cover the Holocene age. We show the parameters for each sample: the modal values of C_{ext} (a), *csa* (b), and *tdr* distributions (c), and the counts number (d). Although broad distributions characterize both the area and the C_{ext}, the modal value appears to be almost homogeneous among the different age, with some spikes in the Medium Holocene, where we observed greater *csa* values (up to $\sim 7\,\mu\text{m}^2$) in accordance to a higher C_{ext} values (up to $\sim 15\,\mu\text{m}^2$). This is in correspondence of an increase of the coarse particle percentage (CPP) over the fine particle percentage (FPP), observed by Coulter. In particular, we define the fine, coarse and giant particle percentage as the ratio of the following volume-equivalent diameters ranges (in µm):

$$FPP = \frac{(1-2)}{(1-5)} \cdot 100$$
$$CPP = \frac{(3-5)}{(1-5)} \cdot 100$$
$$GPP = \frac{(10-18)}{(0.6-18)} \cdot 100$$

We observed a prevalence of a principal *tdr* range between 0.1 and 0.25, indicating the most presence of plates particles. Moreover, also the thicker particles do not exceed a $tdr > 0.6$ (in the modal value). We found also some aggregates, especially in the samples with higher counts, due maybe to an in situ particulate aggregation process.

Finally, Figure 3.25 shows the particle counts for each sample in comparison with Coulter Counter results. As in the previous section, in order to compare the two analyses, we select the same range of cross-sectional area, from 1 to $50\,\mu\text{m}^2$ (that correspond to an equivalent spherical diameter range of $1.3 - 7.9\,\mu\text{m}$). Even if the absolute counts differ due to the different sensitivities of the two instruments, we can state that Coulter Counter and holography measurements are in good agreement, and they follow a similar trend over the years. Coulter measurements revealed on average a higher percentage of fine particles ($\sim 49\%$) than coarse ($\sim 25\%$). We don't observe this marked difference because we do not have access to size range $< 1\,\mu\text{m}$, however, we still notice a higher presence of fine particles,

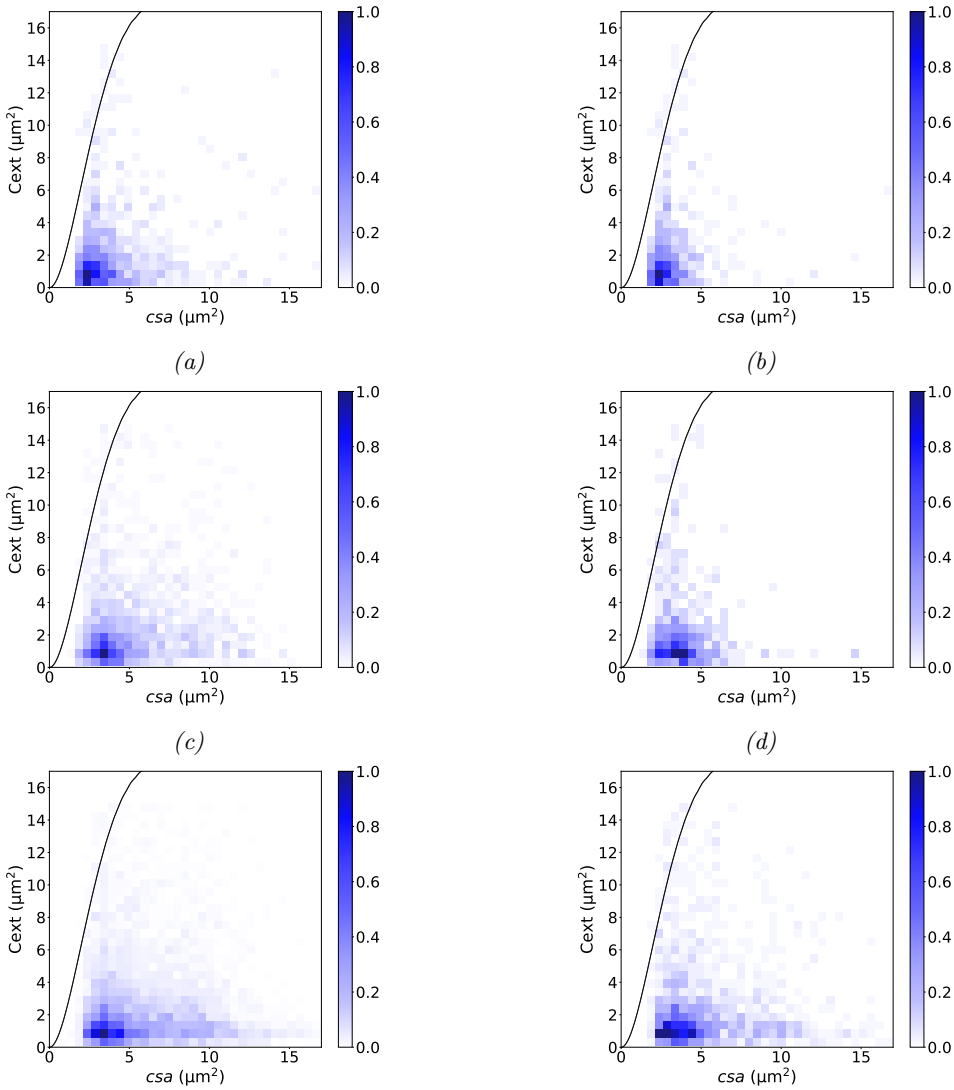

Figure 3.23: (csa, C_{ext}) planes adopted for representing the digital holography data, reported as two-dimensional histograms and normalized on their maximum (dark blue), relating to three RICE samples at 10 m *(a-b),* 313 m *(c-d), and* 612 m *(e-f) of depth. On the left are shown all the particles detected, on the right only the subset of particles with ar* > 0.8.

Depth (m)	Age (BP)	C_{ext} (µm^2)	*csa* (µm^2)	*ar*	*tdr*	Counts (#)
10	-38	0.77	3.17	0.9	0.15	1773
94	293	0.56	3.17	0.8	0.2	1594
121	435	1.2	3.03	0.9	0.2	1347
128	473	0.74	4.41	0.9	0.2	548
158	654	0.78	2.76	1.0	0.1	1814
159	660	0.39	3.03	0.9	0.25	351
177	777	0.93	3.17	0.9	0.2	1387
190	868	4.26	2.7	1.0	0.5	50
192	884	1.23	3.03	1.0	0.3	296
200	947	0.64	3.79	0.9	0.15	596
209	1020	0.21	2.34	1.0	0.15	3015
215	1070	5.21	6.93	0.9	0.2	96
285	1802	0.63	3.65	0.9	0.2	336
300	1993	12.2	5.16	0.9	0.3	49
313	2184	0.47	2.2	1.0	0.2	826
327	2380	7.75	4.24	0.8	0.4	47
402	3749	0.28	5.08	0.9	0.1	210
434	4302	14.63	3.65	0.8	0.2	91
436	4344	0.7	3.24	0.8	0.1	540
450	4652	0.52	4.27	0.8	0.1	542
456	4778	1.12	3.51	0.8	0.15	299
472	5124	0.58	3.7	0.9	0.1	259
490	5453	0.67	5.93	0.9	0.1	313
523	6296	0.97	2.77	0.9	0.1	873
533	6570	0.57	2.62	0.9	0.15	1965
542	6780	0.29	3.08	0.9	0.2	181
544	6839	0.28	3.31	0.9	0.15	387
558	7204	0.47	4.16	1.0	0.1	378
562	7271	1.37	3.03	0.9	0.2	232
566	7349	0.36	7.17	0.4	0.2	998
600	8589	0.77	3.31	0.9	0.25	1043
612	8903	0.64	3.03	0.9	0.1	5890
623	9265	1.21	2.16	1.0	0.5	463
643	10269	1.04	2.36	1.0	0.4	85

Table 3.2: Depth, age, optical, and size characterization of the RICE ice core samples chosen for the analysis. The C_{ext}, csa, ar, tdr values are the modal values of the distributions.

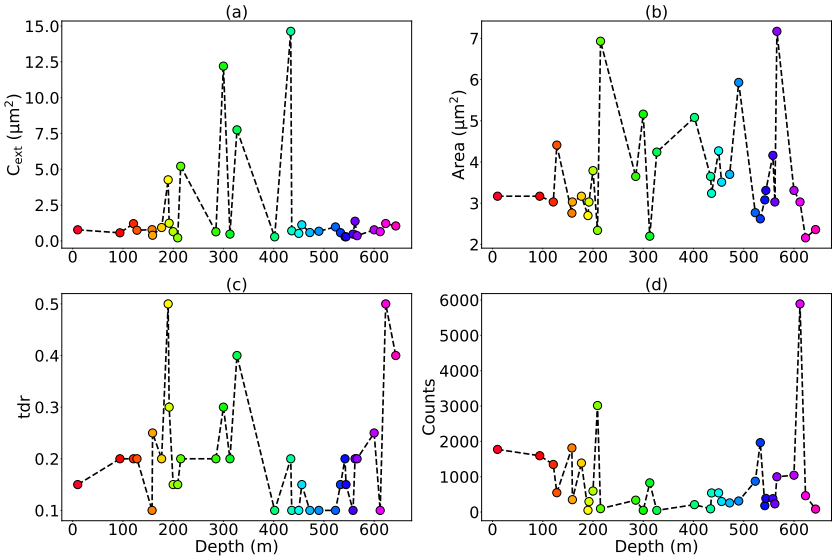

Figure 3.24: Summary of the results reported as a function of sample depth in meter. Modal values of the (a) C_{ext}, (b) csa, (c) tdr and (d) counts distribution of each sample along the Holocene age in RICE ice core.

equals to 33% to be compared with the 25% of coarse particle[3]. In particular, if we extend the definition of FPP to 3 µm, it rises ∼75%. We find in mean 1% of giant particle, with some spike up to 9%. Size is crucial in determining the capability of particles of traveling large distances by aeolian processes. A particularly high concentration of coarse or giant particles may be due to explosive volcanic events, or, more likely, to local transport phenomena. In particular, the Roosevelt Island has probably been influenced by the proximity to the sea, the low elevation (∼ 500m asl), and the presence of volcanic areas in the Mary Byrd Land region. Indeed, similarly to the neighboring site of Talos Dome, as far as the mineral dust profile is concerned, the RICE site is probably characterized by a great sensitivity to variations in atmospheric circulation both locally, in the Ross Sea area, and at a hemispheric scale. Moreover, as we before stated for Alpine snow samples, giant particles contribute more to dust mass and have a strong impact on their radiative interactions. In the shortwave spectrum, larger particles reduce the single scattering albedo, causing more absorption of solar radiation and atmospheric heating. Anyway, in RICE the radiative contribution due to superficial giant particles, probably due to marine algae, is almost negligible because (1) the dust concentration is extremely low (significant effects are observable for concentration $\sim 10^3$ ppb) and

[3]We calculated the FPP, CPP and GPP with the major axis of the *csa*.

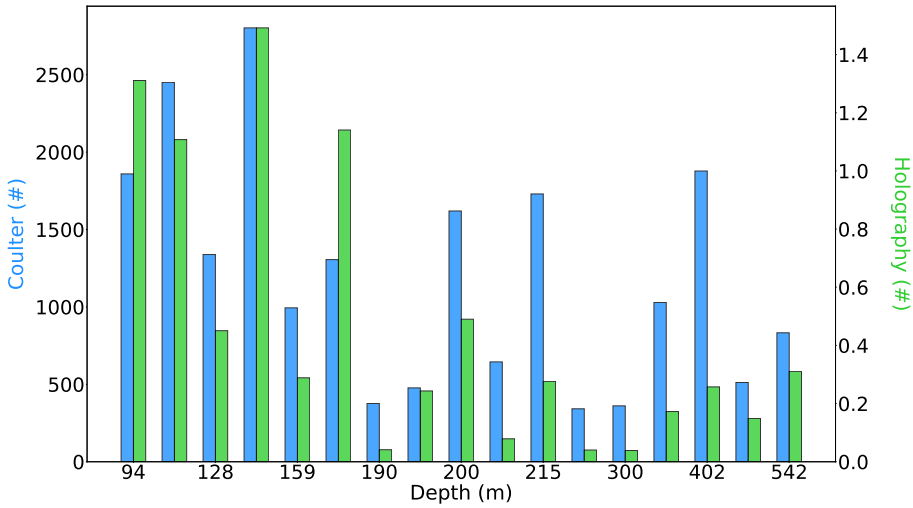

Figure 3.25: Particle counts as a function of sample depth in m. The left y-axis refers to the Coulter Counter measurements (blue bars), whereas the y-axis on the right refers to holography measurements (green bars) on the same size range. The counts are normalized to 1 µL *of volume. The absolute counts differ due to the different sensitivities of the two instruments.*

(2) the radiation in Antarctica is almost grazing to the surface.

3.4 Integrated digital holographic microscopy

After this overview of the effectiveness of the technique to characterize compact non-spherical mineral dust, in the following I will conclude with a technical application of digital holography. A particularly compatible variant of in-line holographic setup can be obtained implementing it over a commercial optical microscope, with few and straightforward modifications. We started from simply replacing the conventional illuminator in a bright-field microscope with a collimated laser. This compact custom-made instrument can be easily accessible to all the scientific community with appreciable results in different fields. A qualitative sketch of the setup is shown in Fig. 3.26, which recalls the in-line scheme (Gabor, 1948). Over an optical microscope (BRESSER Erudit DLX 40-1000x Microscope) we placed a quartz flow-cell (c) centered on the scattering volume (5×0.3 mm cross-section). Instead of the LED illumination, a laser source (a) (He-Ne diode laser, 60 mA) coupled with a (b) commercial collimator (F110FC-633 Fiber Collimation, Thorlabs) impinges on the flow-cell passing through the interaction volume, where the objects to be detected are driven. A custom assembly can be designed with a 3D printer

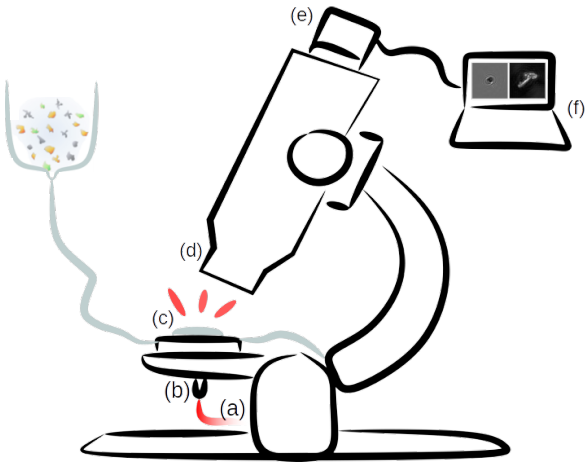

Figure 3.26: Sketch of in-line digital holographic technique integrated over a commercial microscope. A laser diode (a) coupled with a collimator (b) illuminates a thin cell (c) through which particles (gray and yellow objects) are flown. A 20× microscope objective (d) is located in the far-field of the sample, a sensor (e) records the holographic pattern, which transmits the information to a laptop (f).

in order to join the collimator, like that in Fig. 3.27 (b). We suggest tilting the cell compared to the laser source to suppress multi reflection in the image plane ($\sim 10°$). The small fraction of diffracted light superimposes in the forward scattering direction with the (almost unchanged) transmitted beam. The interference between these two fields gives rise to fringes, that depend on the object properties, magnified by a 20× microscope objective (d). Finally, the beam reaches a (e) CMOS detector (IDS camera GV-5260CP-M-GL, 1920×1200, 5.86 µm pixel size). A custom c-mount adapter has been performed at the mechanical workshop of the University of Milan, Department of Physics; anyway, it is a commercial device. The image acquisitions can be checked in real-time by a personal laptop (f). Among the advantages, this adaptation is free from any tight alignment requirement and is particularly suitable for a flow continued analysis thanks to its compactness, cheapness, and availability.

We report the measurements of calibrated polystyrene spheres with different sizes compared with Mie calculations in Fig. 3.28. Some examples of the outputs of the instrument are shown in Fig. 3.29. Both the extinction cross-sections and the diameters distributions are in good agreement with the expected values (dash black lines). We reported in Table 3.3 the results from the corresponding normal distributions that best fit the data. We note that for greater particles the size distribution becomes broadly due to the difficulty to detect the exact focal position

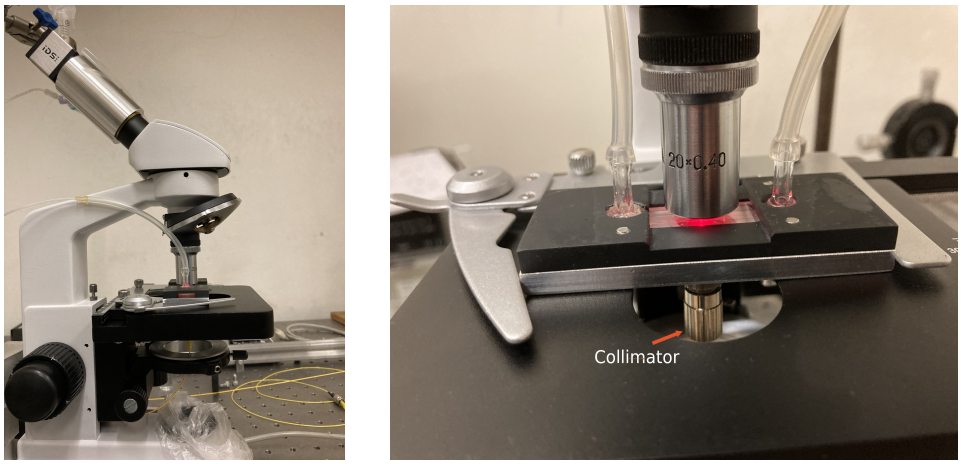

(a) *(b)*

Figure 3.27: Photos of the digital holographic technique integrated over a commercial bright-field microscope.

(as described in Section 2.4). The measurement of the C_{ext} distribution is not affected by the phase aberration of the reconstructing wave, since it is obtained directly from the holographic pattern. For this reason, it is used also as a fine-tuning of the *effective pixel size* over the (x_0, y_0, z_0) plane image[4], that is different from the tabulated detector pixel size due to the magnification (see also Appendix A). We can reasonably suppose that it is equal to $\Delta_{\text{eff}} = \frac{\Delta_{\text{det}}}{M}$, where Δ_{eff} is the effective pixel size, Δ_{det} the pixel size of the detector, and M the magnification number of the objective lens used. In our case $\Delta_{\text{eff}} = \frac{5.86\,\mu\text{m}}{20}$. Anyway, for a better accuracy we suggest relying on the C_{ext} measurements of calibrated particles. We obtained $\Delta_{\text{eff}} = 0.3\,\mu\text{m}$. By the translation of the position of the flow-cell, through the $z-$mechanical slide movement of the microscopic stage, we can automatically change the distance of the focal position z_0 of the objects. This movement doesn't affect the effective pixel size, cause the distance between the detector and the magnification lens is fixed. In this way it is very simple and immediate the choice of the plane image, from which the spacing of the fringes of the holographic patterns depends (Fig. 2.4). The plane image is selected in order to collect all the fringes in the best way. If the plane is too far from the objective lens, we can not detect the fringes at higher scattering angles due to the limited side length of the detector, missing information about the shape of the particles. If the plane is too near to the objective lens, we can not resolve the fringes at all and the holograms

[4]As reminder of the coordinates we recall the in-line holography scheme shown in Fig. 2.3

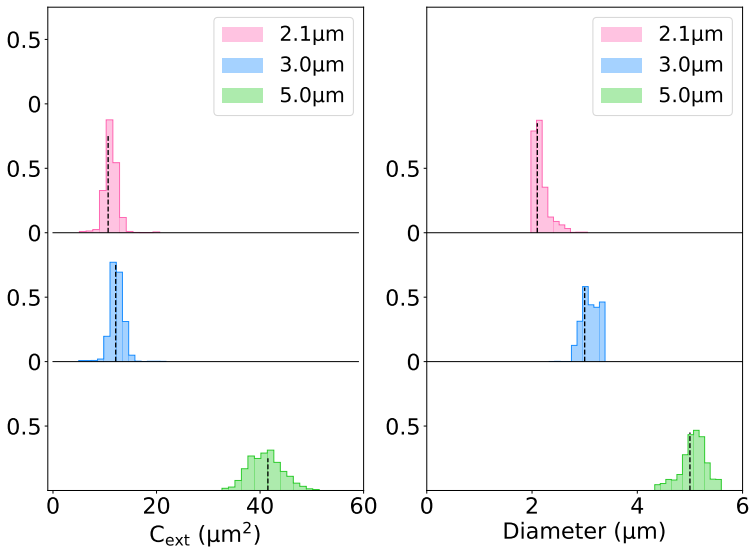

Figure 3.28: Normalized extinction cross-section (a) and size distribution (b) of 2.1, 3 *and* 5 µm *diameter polystyrene spheres in water. The distributions are in good agreement with the expected values, shown as black dashed lines, obtained according to Mie expansion.*

become like point sources. We obtain the focal distance between 340−540 µm evenly distributed. The natural follow-up of this application will be the insert online to the continuous flow analysis instrument currently developing at the EuroCold laboratory.

Quantities	Obtained values	Expected values
C_{ext} (µm^2)	11.0 ± 1.0	10.6
Diameter (µm)	2.1 ± 0.1	2.1
C_{ext} (µm^2)	12.3 ± 1.2	12.1
Diameter (µm)	3.1 ± 0.2	3
C_{ext} (µm^2)	40.8 ± 3.3	41.5
Diameter (µm)	5.1 ± 0.2	5

Table 3.3: Means and standard deviation values obtained through a normal distribution that best fit the C_{ext} and size distributions of 2.1, 3 *and* 5 µm *diameter polystyrene spheres in water. The values are compared with that of spherical particles, obtained according to Mie expansion. The color are coded as in Fig. 3.28.*

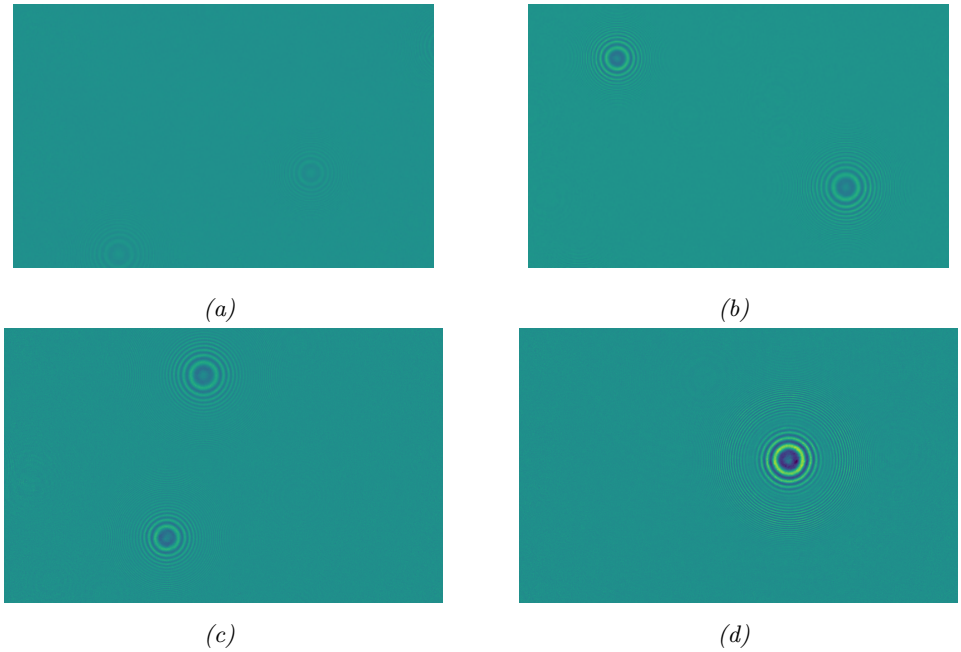

(a) *(b)* *(c)* *(d)*

Figure 3.29: From (a) to (d): experimental contrast hologram of 1, 2.1, 3 *and* 5 m*icrometer-polystyrene beads in water obtained throw the normalization of the raw image with the background. We reported the output as a color gradient with the same scale (minimum value: 0.8 blue, maximum value: 1.2 yellow.*

Conclusions

The purpose of this thesis was to characterize non-absorbing size-polydisperse micrometric mineral dust particles in liquid suspensions, providing information about the morphological and optical properties of each measured particle. In particular, the effect of shape on their radiative properties has been investigated.
In strictly collaboration with the EuroCold research group (Università Degli Studi di Milano), we study Antarctic and Alpine ice core samples by the development of a digital holographic technique, which has proven to be an excellent suite for distinguishing non-spherical particles, going beyond the common spherical approximation. For example, in the presented case in Sect. 3.2, the size of the particles would have been overestimated by a factor ~ 1.5 with equivalent spherical diameters.
The instrument setup resembles a flow imaging microscope and the acquisition process is at least as fast. From an imaging standpoint, the resolution of the images reconstructed from the holograms is intrinsically lower than those from an equivalent optical microscope; on the other hand, the holograms contain usable information about the particle's optical properties. Particle size and shape can be easily identified, and image quality can be enhanced computationally. Moreover, holography relies on the capability of recovering images and optical information from objects within volumes much thicker than the limited depth of focus of traditional imaging.
The technique shows results that are compatible with Coulter Counter measurements; the setup works at low flow rates (~ 1 ml/min) and can be implemented in continuous flow analysis systems typically used in ice core characterization. Moreover, the single-particle approach of the technique ensures the study of dilute and polydisperse samples. In its current design, the instrument is able to effectively detect particles whose extinction cross-section roughly above $C_{\text{ext}} \gtrsim 0.3\,\mu\text{m}^2$. In addition to the extinction cross-section, we retrieve the particle shape, projected on a plane orthogonal to the optical axis.

Our analysis reveals that the majority of the particles in the samples deviate from the isometric shape, with a prevalence of oblate particles with a thickness over diameter ratio ranging between 0.15 and 0.4 for snowpit Antarctic samples, and between 0.1 and 0.25 for deeper ice core. We found in all the samples a remarkable variability in the extinction cross-section of the particles depending on their thickness, for any given size. In the RICE ice core we observed a prevalence of fine ($<2\,\mu m$ in size) particles, with the occurrence of aggregates and some giant ($>10\,\mu m$ in size) particles, with values up to 9%. These particles are a proxy of local transport. In particular, Roosevelt Island cores can be influenced by the proximity to the sea.

Alpine snow samples are characterized by wide and high impurities concentration, from Saharan mineral dust to carbonaceous particles, volcanic ash, micro-algae, and pollen. We observed a particle concentration of about two orders of magnitude greater than Antarctic samples, both in the fine and coarse size range. Moreover, we detect a sensible number of aggregate particles with C_{ext} values ranging between $150-200\,\mu m^2$ and cross-sectional diameters of $20-30\,\mu m$. We are not able to detect melt events in the past, but this high number of aggregates can be associated with some melting processes, sensitive to climate alteration. These have a strong impact on the atmospheric radiative balance, affecting both the single scattering albedo and the aerosol optical depth. We found in average the 8% of giant particles. Coarse and giant dust can change the sign of their net radiative effect and their impact on atmospheric circulation. Therefore, is important to give an accurate estimation of dust particle size distribution across all sizes. We note also a higher number of particles with a non-negligible absorption. The work is currently in progress to give a quantitative characterization.

Finally, we present a variant of in-line holographic setup by implementing the technique over a bright-field microscope, simply by replacing the conventional bright illuminator. A set of measurements with calibrated particles have been provided, showing its efficiency and availability.

Experimental data indicates that the extinction cross-section of isometric particles is up to 3 times that of plate-shaped particles. Indeed, experimental data highlight the importance of multi-parametric characterization in order to obtain reliable particle sizing based on optical methods (as in optical particle counters): the size distribution is strongly model-dependent and varies significantly with the aspect ratio. Depending on its size, dust interaction with shortwave and longwave radiation and its impact on radiative transfer can range from cooling to a warming effect (Huang et al., 2021). Similarly, accounting for dust asphericity leads to significant differences in the aerosol optical depth (compared to spheres) and in the extinction efficiency (Dubovik et al., 2006, Potenza et al., 2016). Cur-

rently, global and regional models assume dust particles as uniform spheres and neglect the coarsest particles (>10/20 µm in diameter), introducing biases in the estimation of the radiative effect (Di Biagio et al., 2020). They will benefit from more accurate modeling of the aerosol size and shapes, especially if obtained from the optical properties themselves. A starting point will be a distinction between spherical and spheroidal particles, and the identification of the aggregate particles, that are a critical indication for post-deposition processes (Potenza et al., 2017). Moreover, absorption and scattering by soot, black carbons, or microbial growth, have a dramatic impact on climate due to their strong interaction with solar and terrestrial radiation. By studying carbon smoke soot aggregates in Appendix A.1, we demonstrated that holography can distinguish absorbing particles from non-absorbing ones, whereby we can state that no trace of highly absorbing particles was found in the analyzed samples. However, studies of a quantitative investigation of how the morphology impacts the absorbing and scattering would be a fruitful area for further research. In conclusion, deriving information about particle shapes, and simultaneously about their extinction and absorption cross-section, is critical to determine the intrinsic single-scattering properties needed for state-of-the-art radiative transfer models (Meng et al., 2010, Kok et al., 2017).

Within the analytical framework offered in the present thesis, several projects can be devised, as a natural extension of the line of research. In particular, the following separate yet related issues will be addressed soon:

The importance of shape

An additional advantage of the holographic method is to be sensitive to the optical thickness of the particles across its transverse section. Optical thickness is intended here as the product of the geometrical thickness and the refractive index, as explained in Section 2.7. Currently, we are working on the reconstruction of the object wave without zero-order intensity and the spurious contribution of the *twin image*, while at the same time compensating the phase aberration. We started on simulated spherical and non-spherical particles, and we will conclude with calibrating particles as polystyrene, kaolinite, and quartz.

Improving the analysis with machine learning techniques

By applying a machine learning technique, we can mitigate the computational cost of detecting, localizing, and analyzing holographic features. Moreover, in this way we will benefit from a robust particles detection for overlapping holograms or even heterogeneous holographic features in the same image, extending the measurements to more dense and heterogeneous samples, like mineral dust in deeper ice core to

date to the Glacial age. Subsequently, the particles can be studied through a discrete dipole approximation, by the implementation of fitting technique with a spheroidal approximation in order to obtain the shape, the three major axes, the C_{ext} and the refractive index of each particle.

Single precipitating ice-crystal holography

The experimental results reported in this thesis regards melted ice core samples. However, besides particles suspended in water, the technique can be operated also to study airborne particles. In particular, we are currently working on a new project for the upgrading, testing, and installation at Concordia (Antarctica) of a digital holographic instrument. The aim is to monitor in real-time the shapes and the extinction cross-sections of ice and snow crystals directly in air. This opens the possibility to easily provide an estimate of the presence of voids-structures inside the crystals-snowflakes. The characterization of the optical properties of ice crystals has great importance on the Antarctic plateau: at lower latitudes, the modulation of the Earth albedo is due to thick clouds and aerosols. On the Antarctic plateau, the scarcity of aerosols and thick water clouds makes ice crystals the main modulator of the radiative transfer of visible radiation in the atmosphere. The radiative transfer models for Antarctica thus require a realistic characterization of the optical properties of the ice crystals, obtainable on a statistical basis through long-term measurements performed by automatic devices. The surface climatic conditions at Concordia are similar to those encountered inside the cirrus clouds elsewhere located at much higher altitudes. Measurements performed at Concordia on suspended ice crystals are therefore similar to those expected inside cirrus and are therefore useful also in the modeling of the radiative transfer of cirrus at lower latitudes and higher altitudes. Finally, the cutting-edge technology of acoustic manipulators will be experimented with for concentrating and trapping the crystals into the measurement volume of the instruments.

Continuous flow analysis

Continuous flow analysis (CFA) is a well-established method to measure aerosol constituents in polar and Alpine ice cores as indicators of past changes in the climate system, in very high-depth resolution. Currently, a CFA is about to be developed at the EuroCold laboratory, at the Università Degli Studi di Milano. The aim is to insert online to the analysis also a digital holographic instrument, implemented in an optical microscope, like that described in Section 3.4, thanks to its compactness.

Publications

i) Ravasio, C., Cremonesi, L., Artoni, C., Delmonte, B., Maggi, V., and Potenza, M. A. (2021). Optical Characterization of Mineral Dust from the EAIIST Project with Digital Holography. ACS Earth and Space Chemistry, 5(10), 2855-2864.

ii) Ravasio, C., A digital holographic technique for studying mineral dust content in ice cores, Il Nuovo Cimento, Società Italiana di Fisica. (In peer review).

Appendices

Appendix A

Calibration Tests

Digital holography boasts both a non-critical accurate alignment of its optical components and a calibration-free, except for the *effective pixel size*, i.e. the physical dimension of the pixels on the image plane, which is different from the detector pixel size due to the magnification. This operation is important because the extinction cross-section and cross-sectional area depend on the pixel size, and therefore it requires fine-tuning. The *effective pixel size* can be obtained in a good estimate checking the dimension of a calibrated object (∼micrometers in size) illuminated by the source. An example may be the use of a matt tape as a diffuser to generate a *speckle* pattern. By the translation of the matt object in a perpendicular way to the optical axis, and by cross-correlating two different positions, we can obtain the pixel size value within a $\sim 1\%$ of error. The final check is given by the C_{ext} value of known particles, as polystyrene beads, as described below. The pixel size obtained for this setup is 0.27 µm and it is kept constant for all the measurements. From this value, we set the other parameters like the amplitude threshold in the object reconstruction (Sec. 3.1).

The performance of the system, in particular of the reconstruction algorithm, has been tested with a dilute colloidal suspension of polymeric beads, namely polystyrene (PS) spheres of several diameters. A Scanning Electron Microscope image of a polystyrene sphere bead 5 µm in diameter is shown in Fig. A.1. We made extensive use of such calibrated polymeric particles as a benchmark for our experimental measurements. In particular, we recovered the size of spherical particles and their cross-sectional extinction, both directly from the pattern (Sec. 2.5), and from the amplitude and phase of the zero-angle scattering amplitude $S(0)$ (Sec. 2.6). Indeed, in this case, the scattering amplitude can be calculated effectively with the Mie theory.
We report in Figures A.2 the results obtained from diluted colloidal suspensions of calibrated polystyrene spheres 2 and 2.9 µm in diameter. The C_{ext} (a) and size (b) distributions are comparable and in accordance with the expected values (dashed black lines).

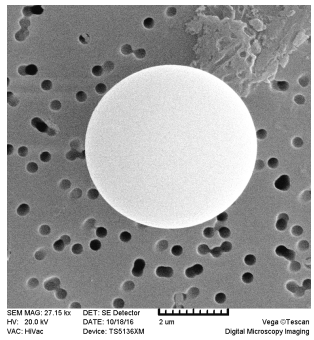

Figure A.1: Scanning Electron Microscope image of a polystyrene sphere bead $5\,\mu\mathrm{m}$ *in diameter (*$n = 1.58$ *at* $\lambda = 633\,\mathrm{nm}$*). The image was acquired by Dr. Delmonte (University of Milano-Bicocca) with a Scanning Electron Microscope at the Euro-Cold laboratory at the University of Milano-Bicocca.*

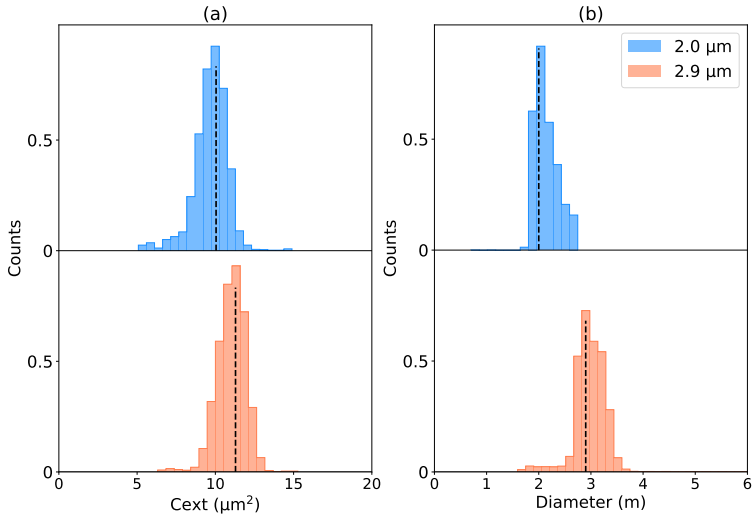

Figure A.2: Normalized (a) extinction cross-section and (b) size distribution of 2 *and* $2.9\,\mu\mathrm{m}$ *diameter polystyrene spheres in water. The distributions are in good agreement with the expected values, shown as black dashed lines, obtained according to Mie expansion.*

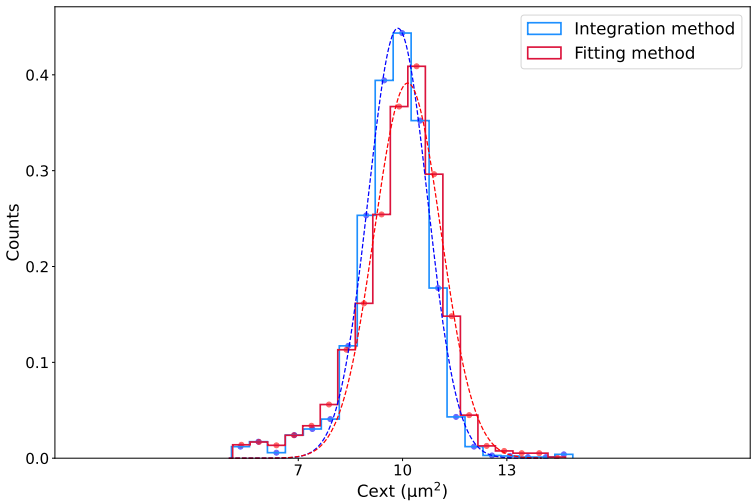

Figure A.3: Normalized C_{ext} distribution of polystyrene beads 2 µm *in diameter obtained through two different methods: by fitting with Eq. 2.36 (red) and by integrating the hologram pattern (blue). The dashed lines are the corresponding normal distributions that best fit the data. Fit values:* $\sigma_{\text{fit}} = 0.8\,\mu\text{m}^2$, $\sigma_{\text{int}} = 0.9\,\mu\text{m}^2$, $\mu_{\text{fit}} = 9.9\,\mu\text{m}^2$, $\mu_{\text{int}} = 10.1\,\mu\text{m}^2$.

Then, in order to validate the image-reconstruction procedure, we recovered the extinction cross-section both using the *Optical Theorem* (Van de Hulst, 1957) and compared the results obtained by integrating the holographic pattern, as described in Sec. 2.5. As shown in Fig. A.3, the two distributions are comparable and in accordance with the expected value ($10\,\mu\text{m}^2$ for a sphere with relative refractive index $n = 1.58$, according to Mie expansion). The *integration* method displays a slightly narrower distribution ($\sigma_{\text{int}} = 0.8\,\mu\text{m}^2$ and $\sigma_{\text{fit}} = 0.9\,\mu\text{m}^2$), and underestimates the value of extinction cross-section ($C_{\text{ext, int}} = 9.9\,\mu\text{m}^2$ and $C_{\text{ext, fit}} = 10.1\,\mu\text{m}^2$, to be compared with $C_{\text{ext, exp}} = 10\,\mu\text{m}^2$). However, this difference is negligible for our purposes.

In Fig. A.4 we show the *csa* according to the C_{ext} distribution both for 2 µm diameter polystyrene (blue data) and kaolinite (red data) in water. Kaolinite are standard monophasic non-spherical particles, with $n \sim 1.55$ (Weidler and Friedrich, 2007). A good agreement is found with Mie calculations for the polystyrene beads ($n = 1.58$), reported with a blue line. This indicates that the particles are isometric (aspect ratio approaching 1), as expected. Non-isometric particles differ from spherical ones in that the field they scatter is susceptible to a change in orientation, so they produce a different distribution. Therefore, fitting the data with a distribu-

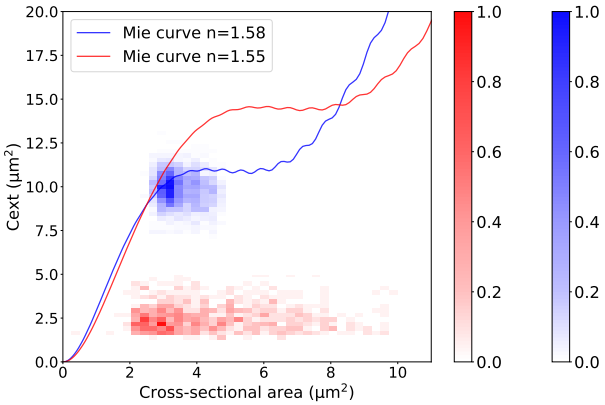

Figure A.4: Cross-sectional area according to the extinction cross-section for 2 µm *diameter polystyrene (blue data) and kaolinite (red data) in water reported as a two-dimensional histogram. Counts are normalised on their maximum. The data are compared with Mie calculations for spheres with a refractive index* $n = 1.58$ *(blue solid line) and* $n = 1.55$ *(red solid line), respectively.*

.

tion of spheres (red line in Fig. A.4) does not match the actual C_{ext} of the oblate particles, since these are located lower in the (*csa*, C_{ext})-plane. This is further evidenced in Fig. A.5, where it is shown the cross-sectional height according to the cross-sectional width of 2 and 2.9 µm diameter polystyrene (a) and kaolinite (b) in water as a two-dimensional histogram. The *major* and *minor* axes are obtained as in Sec. 3.1. The polystyrene distribution lies between an aspect ratio (*ar*) value of 0.8 and 1 (dashed gray and black line, respectively), while the kaolinite distribution shows a consistent number of particles with $ar < 0.5$ (red dashed line), as expected by non-spherical particles. However, kaolinite distribution lays also between $0.8 < ar < 1$, a distinguishing mark of isometric particles. Anyway, as we saw in Fig. A.4, the Mie curve doesn't fit the kaolinite sample. This can seem a paradox, but it is explained by the fact that kaolinite have plate-like shapes and therefore have a C_{ext} consistently lower than it is for spheres, and it is more evident when the *csa* is symmetrical (*ar* approaches 1). In Sec. 3.2 we show that by comparing the C_{ext} of simulated oblate ellipsoids with data, we can obtain the thickness of the particles.

A.1 Absorbing particles

We turn then to the following study for addressing the case of absorbing particles. This is particularly relevant because, as one of the brightest natural surfaces on

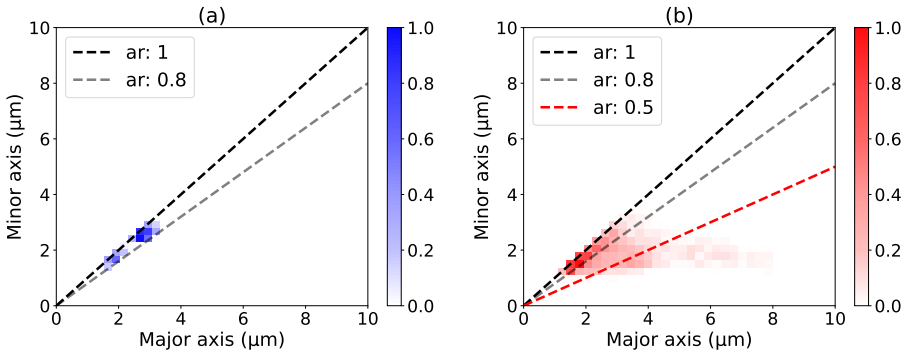

Figure A.5: Cross-sectional height (major axis) according to the cross-sectional width (minor axis) of 2 *and* 2.9 µm *diameter polystyrene (a) and kaolinite (b) in water as a two-dimensional histogram. Counts are normalised on their maximum. Isometric particles show an aspect ratio approaching* 1 *(the distribution lays between ar* 0.8 *and* 1*, black and gray dashed line), while non-isometric particles show a consistent number of particles with ar* <0.5 *(red dashed line).*

.

Earth, the darkening of snow by absorbing particles—dust, black carbon or microbial growth—can trigger albedo feedbacks and accelerate snowmelt. Moreover, an increase in black carbon deposition following the industrial revolution has led to the recognition that absorbing particles radiative forcing has contributed to a reduction in the global cryosphere, with corresponding climatic impacts. In this context, we analyzed carbon smoke soot aggregates produced by suspending 10 mg of dry powder pigment (Sennelier n. 761) in 25 ml pure, filtered water at room temperature, then keeping the suspension in an ultrasonic bath for ∼10 minutes until its properties stabilized. Finally, samples were diluted at 1:20 before the holographic measurements. We don't have specific information about the primary particle diameters, however, we shift our focus on the comparison between absorbing and non-absorbing particles.

The independent scatter approximation (Sect. 1.4) is valid also for absorbing particles, therefore the total absorption cross-section of an aggregate of N identical particle is N times the absorption cross-section of its constituents. In Fig. A.6 we report the integration pattern of two examples of different aggregates particle, from which we obtained the C_{ext} and C_{abs} values, following Sec. 2.5. The reconstructed images are shown in Fig. A.7, while we reported in the Table A.1 the respective values. Nonetheless, holographic reconstruction is not able to separate the contribution of unaltered compact particles from aggregates of small sizes when applying the threshold mask in amplitude. However, since Antarctic samples are in general

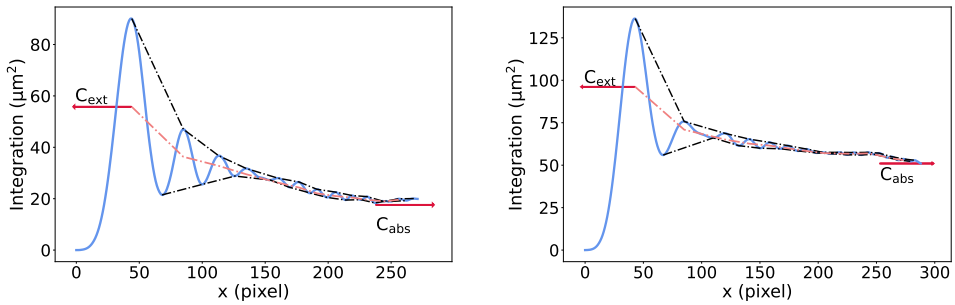

Figure A.6: Examples of carbon smoke soot aggregates produced by suspending dry powder pigment in water. Integration of the corresponding holographic pattern by transition square matrix from the center of the pattern to the edges. The y-scale are in pixel. Following integration, the endpoint of the trend curve (pink dashed line) corresponding to the first maximum gives the C_{ext} (left red arrow). The plot is asymptotic to the C_{abs} value (right red arrow).

Panel	C_{ext} (µm^2)	C_{abs} (µm^2)	*csa* (µm^2)
(a)	55.8	19.6	25.7
(b)	96.1	53.0	42.5

Table A.1: C_{ext}, C_{abs} and csa values of two examples of absorbing aggregates from black dye in water shown in Fig. A.6 and A.7

with an equivalent spherical diameter <5 µm (that is the equivalent of a *csa* of 20 µm^2) we can recognize aggregates from their large *csa* and high C_{ext}. Moreover, we can easily distinguish when a particle has a relevant absorption contribution. In Fig. A.8 we report two examples from polystyrene beads 2 µm in diameter. The integration pattern is asymptotic to $C_{\text{abs}} = 0$, in stark contrast with the black carbon aggregates, which are marked by an exceptionally high C_{ext} for any given size, and are asymptotic to distinct values $\gg 0$.

Actually, this method is not so straightforward. C_{abs} values are more critical to obtain than C_{ext}, because they are strongly affected by the signal over noise ratio of the image, by the accuracy of the localization in the (x_0, y_0) plane, and by the overlaps of the fringes of near particles. An in-depth analysis of such phenomenon could be the subject for future work, starting from the measurements of calibrated carbon aggregates that can be validated by scattering simulation. Anyway, we can safely state that in the Antarctic samples analyzed in the Sections 3.2 and 3.3 no trace of highly absorbing particles was found.

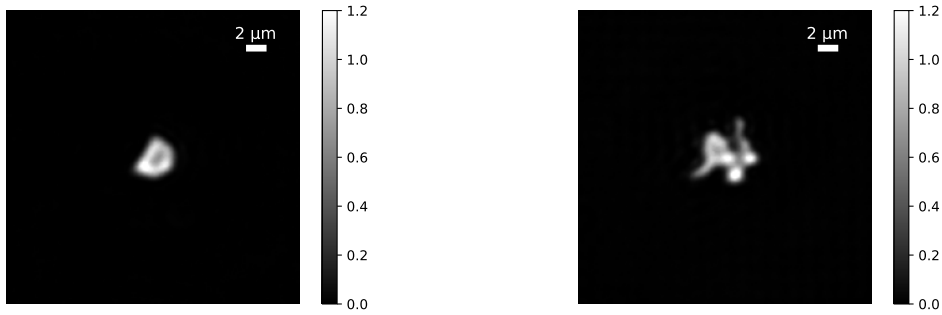

(a) *(b)*

Figure A.7: Image reconstruction of two examples of absorbing particles from carbon smoke soot aggregates in water. The white bar on the top-right corner of each image is set to $2\,\mu\mathrm{m}$.

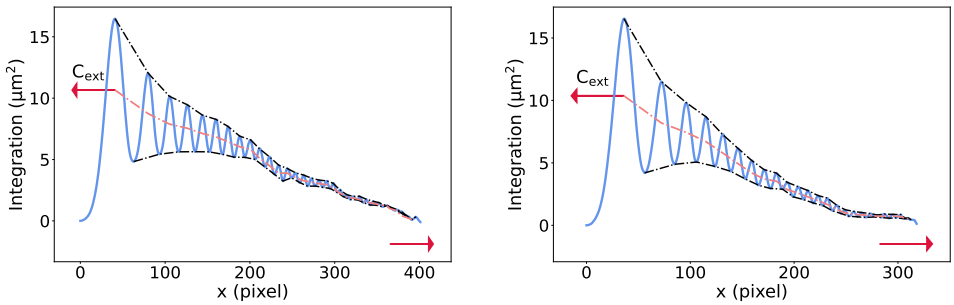

(a) *(b)*

Figure A.8: Examples of non-absorbing spheres from polystyrene in water. Integration of the corresponding holographic pattern by transition square matrix from the center of the pattern to the edges. The y-scale are in pixel. Following integration, the endpoint of the trend curve (pink dashed line) corresponding to the first maximum gives the C_{ext} *(left red arrow). The plot is asymptotic to 0 (right red arrow), reveling that* $C_{\mathrm{sca}} = C_{\mathrm{ext}}$ *(right red arrow).*

Appendix B

Lorenz-Mie theory

In this appendix, we outline the process of obtaining the Lorenz-Mie solutions for the scattering of a plane wave by a sphere (Bohren and Huffman, 2008). We will not work out the detailed derivation, but we will give an overview and highlight a few aspects that are important for our research. We begin by considering a homogeneous, dielectric sphere of radius a_p and refractive index n_p situated at a position, r_p, in a medium with refractive index n_m. We define a spherical coordinate system whose origin coincides with the sphere as depicted in Fig. B.1. The particle in the origin of the reference frame is exposed to an incoming field modeled as a plane wave $\mathbf{E}_0 \sim e^{ikz-i\omega t}$ that propagates toward the scatterer from $\hat{z}$ direction. The scattering event leads to three fields, namely the incident field, the external scattered field, and the internal scattered field, all of which must match boundary conditions at the surface of the sphere. The internal and external fields in the vicinity of a sphere are most naturally expressed as an expansion in vector spherical harmonics. These provide an orthonormal basis for the solutions to Maxwell's wave equations in free space. The Lorenz-Mie solution amounts to expressing the incident plane wave as a sum of vector spherical harmonics and matching the boundary conditions at the surface of the spherical scatterer. After matching the boundary conditions (Bohren and Huffman, 2008, Mishchenko et al., 1996), the resulting external scattering function is

$$\mathbf{f}_s(k\mathbf{r}) = \sum_{n=1}^{\infty} f_n \left[ia_n \mathbf{N}^{(3)}_{\mathrm{e1n}}(k\mathbf{r}) - b_n \mathbf{M}^{(3)}_{\mathrm{o1n}}(k\mathbf{r}) \right], \tag{B.1}$$

where $f_n = i^n(2n+1)/[n(n+1)]$, and $\mathbf{M}^{(3)}_{\mathrm{o1n}}(k\mathbf{r})$ and $\mathbf{N}^{(3)}_{\mathrm{e1n}}(k\mathbf{r})$ are the vector spherical harmonics,

$$\mathbf{M}^{(3)}_{\mathrm{o1n}}(k\mathbf{r}) = \frac{\cos\phi}{\sin\theta} P^1_n(\cos\theta) j_n(\rho)\hat{\theta} - \sin\phi \frac{dP^1_n(\cos\theta)}{d\theta} j_n(\rho)\hat{\phi}, \tag{B.2}$$

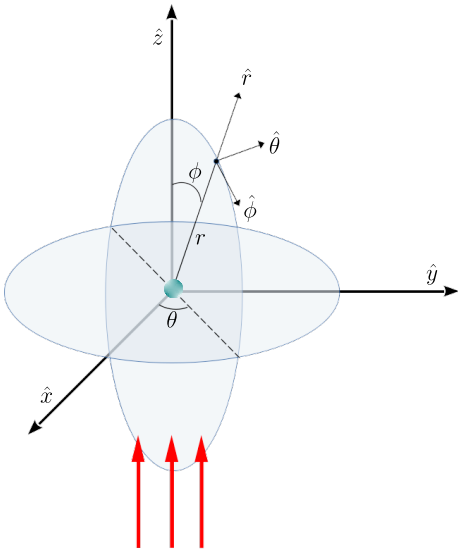

Figure B.1: Spherical coordinates used to describe the Lorenz-Mie theory. The origin of the coordinate system is at the center of the spherical scatterer. For viewing ease, the positive $\hat{z}$ direction is depicted upwards.

and

$$\begin{aligned}\mathbf{N}^{(3)}_{\mathrm{e1n}}(k\mathbf{r}) =& n(n+1)\cos\phi P^1_n(\cos\theta)\frac{j_n(\rho)}{\rho}\hat{\mathbf{r}} \\ &+ \cos\phi\frac{dP^1_n(\cos\theta)}{d\theta}\frac{1}{\rho}\frac{d}{d\rho}[j_n(\rho)]\hat{\theta} \\ &- \frac{\sin\phi}{\sin\theta}P^1_n(\cos\theta)\frac{1}{\rho}\frac{d}{d\rho}[\rho j_n(\rho)]\hat{\phi}.\end{aligned} \tag{B.3}$$

Here, $\rho = kr$ is the reduced radial coordinate, $P^1_n(\cos\theta))$ is the associated Legendre polynomial of the first kind, and $j_n(\rho)$ is the spherical Bessel function of the first kind of order n. The expansion coefficients a_n and b_n in Eq. B.1 are given by (Bohren and Huffman, 2008)

$$a_n = \frac{n_p^2 j_n(x_p)[x_m j_m(x_m)]' - n_m^2 j_n(x_m)[x_p j_m(x_p)]'}{n_p^2 j_n(x_p)[x_m h_n^{(1)}(x_m)]' - n_m^2 h_n^{(1)}(x_m)[x_p j_n(x_p)]'}, \tag{B.4}$$

and

$$b_n = \frac{j_n(x_p)[x_m j_m(x_m)]' - j_n(x_m)[x_p j_m(x_p)]'}{j_n(x_p)[x_m h_n^{(1)}(x_m)]' - h_n^{(1)}(x_m)[x_p j_n(x_p)]'} \tag{B.5}$$

where primes denote derivatives of function with respect to the argument of the embedded special function, and $x_m = \frac{2\pi n_m}{\lambda}a_p$ and $x_p = \frac{2\pi n_p}{\lambda}a_p$ are the reduced

particle size associated with the medium and the particle, respectively. The infinite sum in Eq. B.1 can be safely truncated after $x_m + 4x_m^{1/2} + 2$ terms (Wiscombe, 1980). The vector spherical harmonics do not depend on the scatterer's properties; the scatterer's influence on the external scattered field is completely contained in the expansion coefficients. The coefficients a_n and b_n converge to zero as n_p approaches n_m, which is the case for index-matched particles. The condition for terminating the series in Eq. B.1 depends only on the refractive index of the medium and the size of the particle in units of the wavelength.

In summary, the Lorents Mie theory has some important inherent assumptions. First, we assumed that the particles are spherical: we neglected any surface roughness (for example polystyrene spheres, in particular, are not atomically smooth) or asphericity. We also assumed that the particles are optically homogeneous. Finally, we assumed that the incident beam is sufficiently well-collimated that it may be regarded as a plane wave (even though it is actuality a Gaussian beam in a laboratory setup).

Bibliography

Abbe, E. (1881). Vii.—on the estimation of aperture in the microscope. *Journal of the Royal Microscopical Society*, 1(3):388–423.

Abbe, E. (1883). Xv.—the relation of aperture and power in the microscope (continued). *Journal of the royal microscopical society*, 3(6):790–812.

Albani, S., Balkanski, Y., Mahowald, N., Winckler, G., Maggi, V., and Delmonte, B. (2018). Aerosol-climate interactions during the last glacial maximum. *Current Climate Change Reports*, 4(2):99–114.

Alloway, B. V., Lowe, D. J., Barrell, D. J., Newnham, R. M., Almond, P. C., Augustinus, P. C., Bertler, N. A., Carter, L., Litchfield, N. J., McGlone, M. S., et al. (2007). Towards a climate event stratigraphy for new zealand over the past 30 000 years (nz-intimate project). *Journal of Quaternary Science*, 22(1):9–35.

Anand, A., Chhaniwal, V., and Javidi, B. (2011). Imaging embryonic stem cell dynamics using quantitative 3-d digital holographic microscopy. *IEEE Photonics Journal*, 3(3):546–554.

Babin, M. and Stramski, D. (2002). Light absorption by aquatic particles in the near-infrared spectral region. *Limnology and Oceanography*, 47(3):911–915.

Balkanski, Y., Schulz, M., Claquin, T., and Guibert, S. (2007). Reevaluation of mineral aerosol radiative forcings suggests a better agreement with satellite and aeronet data. *Atmospheric Chemistry and Physics*, 7(1):81–95.

Bauer, E. and Ganopolski, A. (2014). Sensitivity simulations with direct shortwave radiative forcing by aeolian dust during glacial cycles. *Climate of the Past*, 10(4):1333–1348.

Benzie, P. (2008). Thomas kreis, handbook of holographic interferometry: Optical and digital methods, wiley-vch (2005) isbn 3-527-40546-1 preface: 2pp., main

body: 408pp., appendix: 453pp.,€ 169 or£ 114. *Optics and Lasers in Engineering*, 46(1):94–95.

Berg, M. J., Sorensen, C. M., and Chakrabarti, A. (2008). Extinction and the optical theorem. part i. single particles. *JOSA A*, 25(7):1504–1513.

Berg, M. J., Subedi, N. R., and Anderson, P. A. (2017). Measuring extinction with digital holography: nonspherical particles and experimental validation. *Optics letters*, 42(5):1011–1014.

Berg, M. J., Subedi, N. R., Anderson, P. A., and Fowler, N. B. (2014). Using holography to measure extinction. *Optics letters*, 39(13):3993–3996.

Berg, M. J. and Videen, G. (2011). Digital holographic imaging of aerosol particles in flight. *Journal of Quantitative Spectroscopy and Radiative Transfer*, 112(11):1776–1783.

Bertler, N. A., Conway, H., Dahl-Jensen, D., Emanuelsson, D. B., Winstrup, M., Vallelonga, P. T., Lee, J. E., Brook, E. J., Severinghaus, J. P., Fudge, T. J., et al. (2018). The ross sea dipole-temperature, snow accumulation and sea ice variability in the ross sea region, antarctica, over the past 2700 years. *Climate of the Past*, 14(2):193–214.

Bierbaum, M., Leahy, B. D., Alemi, A. A., Cohen, I., and Sethna, J. P. (2017). Light microscopy at maximal precision. *Physical Review X*, 7(4):041007.

Bigler, M., Svensson, A., Kettner, E., Vallelonga, P., Nielsen, M. E., and Steffensen, J. P. (2011). Optimization of high-resolution continuous flow analysis for transient climate signals in ice cores. *Environmental science & technology*, 45(10):4483–4489.

Bohren, C. F. and Huffman, D. R. (2008). *Absorption and scattering of light by small particles*. John Wiley & Sons.

Bond, T. C., Doherty, S. J., Fahey, D., Forster, P., Berntsen, T., DeAngelo, B., Flanner, M., Ghan, S., Kärcher, B., Koch, D., et al. (2013). Bounding the role of black carbon in the climate system: A scientific assessment. *Journal of Geophysical Research: Atmospheres*, 118(11):5380–5552.

Booth, B. B., Dunstone, N. J., Halloran, P. R., Andrews, T., and Bellouin, N. (2012). Aerosols implicated as a prime driver of twentieth-century north atlantic climate variability. *Nature*, 484(7393):228–232.

Born, M. and Wolf, E. (2013). *Principles of optics: electromagnetic theory of propagation, interference and diffraction of light*. Elsevier.

Carl, D., Kemper, B., Wernicke, G., and von Bally, G. (2004). Parameter-optimized digital holographic microscope for high-resolution living-cell analysis. *Applied optics*, 43(36):6536–6544.

Carslaw, K., Boucher, O., Spracklen, D., Mann, G., Rae, J., Woodward, S., and Kulmala, M. (2010). A review of natural aerosol interactions and feedbacks within the earth system. *Atmospheric Chemistry and Physics*, 10(4):1701–1737.

Carslaw, K. S., Gordon, H., Hamilton, D. S., Johnson, J. S., Regayre, L. A., Yoshioka, M., and Pringle, K. J. (2017). Aerosols in the pre-industrial atmosphere. *Current Climate Change Reports*, 3(1):1–15.

Chung, S. H. and Seinfeld, J. H. (2005). Climate response of direct radiative forcing of anthropogenic black carbon. *Journal of Geophysical Research: Atmospheres*, 110(D11).

Claquin, T., Schulz, M., Balkanski, Y., and Boucher, O. (1998). Uncertainties in assessing radiative forcing by mineral dust. *Tellus B*, 50(5):491–505.

Courville, Z. R., Lieblappen, R. M., Thurston, A. K., Barbato, R. A., Fegyveresi, J. M., Farnsworth, L. B., Derry, J., Jones, R. M., Doherty, S. J., and Rosten, S. A. (2020). Microorganisms associated with dust on alpine snow. *Frontiers in Earth Science*, 8:122.

Cremonesi, L. (2021). Probing the morphology of dust particles in deep ice cores with light scattering. *Il nuovo cimento C*, 44(1):1–10.

Cremonesi, L., Passerini, A., Tettamanti, A., Paroli, B., Delmonte, B., Albani, S., Cavaliere, F., Viganò, D., Bettega, G., Sanvito, T., Pullia, A., and Potenza, M. A. C. (Dec 2019). Multiparametricoptical characterizationof airborne dust with single particle extinction and scattering. *Aerosol Science and Technology*, 0(ja):1–15.

Cuche, E., Bevilacqua, F., and Depeursinge, C. (1999a). Digital holography for quantitative phase-contrast imaging. *Optics letters*, 24(5):291–293.

Cuche, E., Marquet, P., and Depeursinge, C. (1999b). Simultaneous amplitude-contrast and quantitative phase-contrast microscopy by numerical reconstruction of fresnel off-axis holograms. *Applied optics*, 38(34):6994–7001.

Cuche, E., Poscio, P., and Depeursinge, C. D. (1996). Optical tomography at the microscopic scale by means of a numerical low-coherence holographic technique. In *Optical and Imaging Techniques for Biomonitoring II*, volume 2927, pages 61–66. International Society for Optics and Photonics.

Debye, P., Anderson Jr, H., and Brumberger, H. (1957). Scattering by an inhomo-

geneous solid. ii. the correlation function and its application. *Journal of applied Physics*, 28(6):679–683.

Debye, P. and Bueche, A. (1949). Scattering by an inhomogeneous solid. *Journal of Applied Physics*, 20(6):518–525.

Delmonte, B., Paleari, C. I., Andò, S., Garzanti, E., Andersson, P. S., Petit, J. R., Crosta, X., Narcisi, B., Baroni, C., Salvatore, M. C., et al. (2017). Causes of dust size variability in central east antarctica (dome b): Atmospheric transport from expanded south american sources during marine isotope stage 2. *Quaternary Science Reviews*, 168:55–68.

Delmonte, B., Petit, J., Andersen, K. K., Basile-Doelsch, I., Maggi, V., and Lipenkov, V. Y. (2004). Dust size evidence for opposite regional atmospheric circulation changes over east antarctica during the last climatic transition. *Climate Dynamics*, 23(3-4):427–438.

Delmonte, B., Petit, J., and Maggi, V. (2002). Glacial to holocene implications of the new 27000-year dust record from the epica dome c (east antarctica) ice core. *Climate Dynamics*, 18(8):647–660.

Di Biagio, C., Balkanski, Y., Albani, S., Boucher, O., and Formenti, P. (2020). Direct radiative effect by mineral dust aerosols constrained by new microphysical and spectral optical data. *Geophysical Research Letters*, 47(2):e2019GL086186.

Di Mauro, B., Baccolo, G., Garzonio, R., Giardino, C., Massabò, D., Piazzalunga, A., Rossini, M., and Colombo, R. (2017). Impact of impurities and cryoconite on the optical properties of the morteratsch glacier (swiss alps). *The Cryosphere*, 11(6):2393–2409.

Di Mauro, B., Fava, F., Ferrero, L., Garzonio, R., Baccolo, G., Delmonte, B., and Colombo, R. (2015). Mineral dust impact on snow radiative properties in the european alps combining ground, uav, and satellite observations. *Journal of geophysical research: Atmospheres*, 120(12):6080–6097.

Dubovik, O., Holben, B., Eck, T. F., Smirnov, A., Kaufman, Y. J., King, M. D., Tanré, D., and Slutsker, I. (2002). Variability of absorption and optical properties of key aerosol types observed in worldwide locations. *Journal of the atmospheric sciences*, 59(3):590–608.

Dubovik, O., Sinyuk, A., Lapyonok, T., Holben, B. N., Mishchenko, M., Yang, P., Eck, T. F., Volten, H., Munoz, O., Veihelmann, B., et al. (2006). Application of spheroid models to account for aerosol particle nonsphericity in remote sensing of desert dust. *Journal of Geophysical Research: Atmospheres*, 111(D11).

Ebert, E. E. and Curry, J. A. (1992). A parameterization of ice cloud optical properties for climate models. *Journal of Geophysical Research: Atmospheres*, 97(D4):3831–3836.

Ellis, A., Edwards, R., Saunders, M., Chakrabarty, R. K., Subramanian, R., Timms, N. E., Van Riessen, A., Smith, A. M., Lambrinidis, D., Nunes, L. J., et al. (2016). Individual particle morphology, coatings, and impurities of black carbon aerosols in antarctic ice and tropical rainfall. *Geophysical Research Letters*, 43(22):11–875.

Ferrero, L., Ritter, C., Cappelletti, D., Moroni, B., Močnik, G., Mazzola, M., Lupi, A., Becagli, S., Traversi, R., Cataldi, M., et al. (2019). Aerosol optical properties in the arctic: The role of aerosol chemistry and dust composition in a closure experiment between lidar and tethered balloon vertical profiles. *Science of the total environment*, 686:452–467.

Field, J. P., Belnap, J., Breshears, D. D., Neff, J. C., Okin, G. S., Whicker, J. J., Painter, T. H., Ravi, S., Reheis, M. C., and Reynolds, R. L. (2010). The ecology of dust. *Frontiers in Ecology and the Environment*, 8(8):423–430.

Formenti, P., Schütz, L., Balkanski, Y., Desboeufs, K., Ebert, M., Kandler, K., Petzold, A., Scheuvens, D., Weinbruch, S., and Zhang, D. (2011). Recent progress in understanding physical and chemical properties of african and asian mineral dust. *Atmospheric Chemistry and Physics*, 11(16):8231–8256.

Gabor, D. (1948). A new microscopic principle. *nature*, 161:777–778.

Gabor, D. (1949). Microscopy by reconstructed wave-fronts. *Proceedings of the Royal Society of London. Series A. Mathematical and Physical Sciences*, 197(1051):454–487.

Ghan, S. J. and Zaveri, R. A. (2007). Parameterization of optical properties for hydrated internally mixed aerosol. *Journal of Geophysical Research: Atmospheres*, 112(D10).

Goodman, J. W. (2005). Introduction to fourier optics, roberts & co. *Publishers, Englewood, Colorado*.

Hansen, J. and Nazarenko, L. (2004). Soot climate forcing via snow and ice albedos. *Proceedings of the national academy of sciences*, 101(2):423–428.

Haywood, J. and Boucher, O. (2000). Estimates of the direct and indirect radiative forcing due to tropospheric aerosols: A review. *Reviews of geophysics*, 38(4):513–543.

Hinds, W. C. (1999). *Aerosol technology: properties, behavior, and measurement*

of airborne particles. John Wiley & Sons.

Hoham, R. W. and Remias, D. (2020). Snow and glacial algae: a review1. *Journal of Phycology*, 56(2):264–282.

Horvath, H. (2009). Gustav mie and the scattering and absorption of light by particles: Historic developments and basics. *Journal of Quantitative Spectroscopy and Radiative Transfer*, 110(11):787–799.

Huang, Y., Adebiyi, A. A., Formenti, P., and Kok, J. F. (2021). Linking the different diameter types of aspherical desert dust indicates that models underestimate coarse dust emission. *Geophysical Research Letters*, 48(6):e2020GL092054.

Huang, Y., Kok, J. F., Kandler, K., Lindqvist, H., Nousiainen, T., Sakai, T., Adebiyi, A., and Jokinen, O. (2020). Climate models and remote sensing retrievals neglect substantial desert dust asphericity. *Geophysical Research Letters*, 47(6):e2019GL086592.

Ito, A. and Wagai, R. (2017). Global distribution of clay-size minerals on land surface for biogeochemical and climatological studies. *Scientific data*, 4(1):1–11.

Jähne, B. (1995). Concepts, algorithms, and scientific applications. *Digital Image Processing, 3rd ed.; Springer: New York, NY, USA*.

Javidi, B., Moon, I., and Anand, A. (2017). Automated disease identification with 3d optical imaging. In *2017 16th Workshop on Information Optics (WIO)*, pages 1–2. IEEE.

Jenk, T. M., Szidat, S., Schwikowski, M., Gäggeler, H. W., Brütsch, S., Wacker, L., Synal, H.-A., and Saurer, M. (2006). Radiocarbon analysis in an alpine ice core: record of anthropogenic and biogenic contributions to carbonaceous aerosols in the past (1650–1940). *Atmospheric Chemistry and Physics*, 6(12):5381–5390.

Kahn, A. (1957). Studies on the size and shape of clay particles in aqueous suspension. *Clays and Clay Minerals*, 6(1):220–236.

Kahnert, M., Nousiainen, T., Lindqvist, H., and Ebert, M. (2012). Optical properties of light absorbing carbon aggregates mixed with sulfate: assessment of different model geometries for climate forcing calculations. *Optics express*, 20(9):10042–10058.

Kahnert, M., Nousiainen, T., and Räisänen, P. (2007). Mie simulations as an error source in mineral aerosol radiative forcing calculations. *Quarterly Journal of the Royal Meteorological Society: A journal of the atmospheric sciences, applied meteorology and physical oceanography*, 133(623):299–307.

Kärcher, B., Möhler, O., DeMott, P. J., Pechtl, S., and Yu, F. (2007). Insights into the role of soot aerosols in cirrus cloud formation. *Atmospheric Chemistry and Physics Discussions*, 7(3):7843–7905.

Kasimbeg, P. N., Cheong, F. C., Ruffner, D. B., Blusewicz, J. M., and Philips, L. A. (2019). Holographic characterization of protein aggregates in the presence of silicone oil and surfactants. *Journal of pharmaceutical sciences*, 108(1):155–161.

Kaufman, Y. J. and Koren, I. (2006). Smoke and pollution aerosol effect on cloud cover. *Science*, 313(5787):655–658.

Kaufmann, P. R., Federer, U., Hutterli, M. A., Bigler, M., Schupbach, S., Ruth, U., Schmitt, J., and Stocker, T. F. (2008). An improved continuous flow analysis system for high-resolution field measurements on ice cores. *Environmental science & technology*, 42(21):8044–8050.

Kemper, B. and Von Bally, G. (2008). Digital holographic microscopy for live cell applications and technical inspection. *Applied optics*, 47(4):A52–A61.

Kemppinen, O., Laning, J. C., Mersmann, R. D., Videen, G., and Berg, M. J. (2020). Imaging atmospheric aerosol particles from a uav with digital holography. *Scientific reports*, 10(1):1–12.

Kinnan, M. K. and Chumanov, G. (2010). Plasmon coupling in two-dimensional arrays of silver nanoparticles: Ii. effect of the particle size and interparticle distance. *The Journal of Physical Chemistry C*, 114(16):7496–7501.

Kohfeld, K. E. and Harrison, S. P. (2001). Dirtmap: the geological record of dust. *Earth-Science Reviews*, 54(1-3):81–114.

Kok, J. F., Parteli, E. J., Michaels, T. I., and Karam, D. B. (2012). The physics of wind-blown sand and dust. *Reports on progress in Physics*, 75(10):106901.

Kok, J. F., Ridley, D. A., Zhou, Q., Miller, R. L., Zhao, C., Heald, C. L., Ward, D. S., Albani, S., and Haustein, K. (2017). Smaller desert dust cooling effect estimated from analysis of dust size and abundance. *Nature Geoscience*, 10(4):274–278.

Kreis, T. (1996). *Holographic interferometry: principles and methods*. Wiley-VCH.

Kreuzer, H. J., Pomerleau, N., Blagrave, K., and Jericho, M. H. (1999). Digital inline holography with numerical reconstruction. In *Interferometry'99: Techniques and Technologies*, volume 3744, pages 65–74. International Society for Optics and Photonics.

Krishnatreya, B. J. and Grier, D. G. (2014). Fast feature identification for holographic tracking: The orientation alignment transform. *Optics Express*, 22(11):12773–12778.

Kühn, J., Charrière, F., Colomb, T., Cuche, E., Montfort, F., Emery, Y., Marquet, P., and Depeursinge, C. (2008). Axial sub-nanometer accuracy in digital holographic microscopy. *Measurement Science and Technology*, 19(7):074007.

Kylling, A., Groot Zwaaftink, C., and Stohl, A. (2018). Mineral dust instantaneous radiative forcing in the arctic. *Geophysical Research Letters*, 45(9):4290–4298.

Lambert, F., Bigler, M., Steffensen, J. P., Hutterli, M., and Fischer, H. (2012). Centennial mineral dust variability in high-resolution ice core data from dome c, antarctica. *Climate of the Past*, 8(2):609–623.

Lambert, F., Delmonte, B., Petit, J.-R., Bigler, M., Kaufmann, P. R., Hutterli, M. A., Stocker, T. F., Ruth, U., Steffensen, J. P., and Maggi, V. (2008). Dust-climate couplings over the past 800,000 years from the epica dome c ice core. *Nature*, 452(7187):616–619.

Lambert, F., Kug, J., Park, R., Mahowald, N., Winckler, G., Abe-Ouchi, A., O'ishi, R., Takemura, T., and Lee, J. (2013). The role of mineral-dust aerosols in polar temperature amplification. *Nature Climate Change*, 3(5):487–491.

Latychevskaia, T. and Fink, H.-W. (2015). Practical algorithms for simulation and reconstruction of digital in-line holograms. *Applied optics*, 54(9):2424–2434.

Lawrence, C. R. and Neff, J. C. (2009). The contemporary physical and chemical flux of aeolian dust: A synthesis of direct measurements of dust deposition. *Chemical Geology*, 267(1-2):46–63.

Lee, J., Brook, E., Bertler, N., Buizert, C., Baisden, T., Blunier, T., Ciobanu, V., Conway, H., Dahl-Jensen, D., Fudge, T., et al. (2018). An 83 000 year old ice core from roosevelt island, ross sea, antarctica, clim. past discuss.

Lee, S.-H. and Grier, D. G. (2007). Holographic microscopy of holographically trapped three-dimensional structures. *Optics Express*, 15(4):1505–1512.

Lee, S.-H., Roichman, Y., Yi, G.-R., Kim, S.-H., Yang, S.-M., Van Blaaderen, A., Van Oostrum, P., and Grier, D. G. (2007). Characterizing and tracking single colloidal particles with video holographic microscopy. *Optics express*, 15(26):18275–18282.

Liebling, M., Blu, T., and Unser, M. (2004). Complex-wave retrieval from a single off-axis hologram. *JOSA A*, 21(3):367–377.

Lohmann, U. and Feichter, J. (2005). Global indirect aerosol effects: a review. *Atmospheric Chemistry and Physics*, 5(3):715–737.

Lunga, D. D., Müller, W., Rasmussen, S. O., Svensson, A., and Vallelonga, P. (2017). Calibrated cryo-cell uv-la-icpms elemental concentrations from the ngrip ice core reveal abrupt, sub-annual variability in dust across the gi-21.2 interstadial period. *The Cryosphere*, 11(3):1297–1309.

Maffezzoli, N., Vallelonga, P., Spolaor, A., Barbante, C., Edwards, R., Saiz-Lopez, A., Kjær, H. A., Simonsen, M., and Vinther, B. (2017). 125,000 year arctic sea ice variability from the renland ice core. In *EGU General Assembly Conference Abstracts*, volume 19, page 10478.

Maher, B., Prospero, J., Mackie, D., Gaiero, D., Hesse, P. P., and Balkanski, Y. (2010). Global connections between aeolian dust, climate and ocean biogeochemistry at the present day and at the last glacial maximum. *Earth-Science Reviews*, 99(1-2):61–97.

Mahowald, N., Albani, S., Kok, J. F., Engelstaeder, S., Scanza, R., Ward, D. S., and Flanner, M. G. (2014). The size distribution of desert dust aerosols and its impact on the earth system. *Aeolian Research*, 15:53–71.

Mahowald, N. M., Engelstaedter, S., Luo, C., Sealy, A., Artaxo, P., Benitez-Nelson, C., Bonnet, S., Chen, Y., Chuang, P. Y., Cohen, D. D., Dulac, F., Herut, B., Johansen, A. M., Kubilay, N., Losno, R., Maenhaut, W., Paytan, A., Prospero, J. M., Shank, L. M., and Siefert, R. L. (2009). Atmospheric iron deposition: global distribution, variability, and human perturbations. *Annual Review of Marine Science*, 1(1):245–278.

Mariani, F., Bernardoni, V., Riccobono, F., Vecchi, R., Valli, G., Sanvito, T., Paroli, B., Pullia, A., and Potenza, M. A. C. (2017). Single particle extinction and scattering allows novel optical characterization of aerosols. *Journal of Nanoparticle Research*, 19(8):291.

Marks, F. (1987). Marine aerosols and whitecaps in the north atlantic and greenland sea regions. *Deutsche Hydrografische Zeitschrift*, 40(2):71–79.

Martínez-Garcia, A., Rosell-Melé, A., Jaccard, S. L., Geibert, W., Sigman, D. M., and Haug, G. H. (2011). Southern ocean dust–climate coupling over the past four million years. *Nature*, 476(7360):312–315.

Massabò, D., Caponi, L., Bernardoni, V., Bove, M., Brotto, P., Calzolai, G., Cassola, F., Chiari, M., Fedi, M., Fermo, P., et al. (2015). Multi-wavelength optical determination of black and brown carbon in atmospheric aerosols. *Atmospheric*

Environment, 108:1–12.

Mauro, B. D., Garzonio, R., Baccolo, G., Gilardoni, S., Rossini, M., and Colombo, R. (2021). Light-absorbing particles in snow and ice: A brief journey across latitudes. In *Springer Series in Light Scattering*, pages 1–29. Springer.

Mauro, B. D., Garzonio, R., Rossini, M., Filippa, G., Pogliotti, P., Galvagno, M., di Cella, U. M., Migliavacca, M., Baccolo, G., Clemenza, M., et al. (2019). Saharan dust events in the european alps: role on snowmelt and geochemical characterization. *The Cryosphere*, 13(a):1147–1165.

McTainsh, G., Lynch, A., and Burgess, R. (1990). Wind erosion in eastern australia. *Soil Research*, 28(2):323–339.

Meng, Z., Yang, P., Kattawar, G. W., Bi, L., Liou, K., and Laszlo, I. (2010). Single-scattering properties of tri-axial ellipsoidal mineral dust aerosols: A database for application to radiative transfer calculations. *Journal of Aerosol Science*, 41(5):501–512.

Miller, R., Cakmur, R., Perlwitz, J., Geogdzhayev, I., Ginoux, P., Koch, D., Kohfeld, K., Prigent, C., Ruedy, R., Schmidt, G., et al. (2006). Mineral dust aerosols in the nasa goddard institute for space sciences modele atmospheric general circulation model. *Journal of Geophysical Research: Atmospheres*, 111(D6).

Mishchenko, M., Lacis, A., Carlson, B., and Travis, L. (1995). Nonsphericity of dust-like tropospheric aerosols: Implications for aerosol remote sensing and climate modeling. *Geophysical Research Letters*, 22(9):1077–1080.

Mishchenko, M. I., Travis, L. D., and Mackowski, D. W. (1996). T-matrix computations of light scattering by nonspherical particles: A review. *Journal of Quantitative Spectroscopy and Radiative Transfer*, 55(5):535–575.

Moosmüller, H., Engelbrecht, J. P., Skiba, M., Frey, G., Chakrabarty, R. K., and Arnott, W. P. (2012). Single scattering albedo of fine mineral dust aerosols controlled by iron concentration. *Journal of Geophysical Research: Atmospheres*, 117(D11).

Nadeau, J., Cho, Y. B., El-Kholy, M., Bedrossian, M., Rider, S., Lindensmith, C., and Wallace, J. K. (2016). Holographic microscopy for 3d tracking of bacteria. In *Quantitative Phase Imaging II*, volume 9718, page 97182B. International Society for Optics and Photonics.

Newton, R. G. (1976). Optical theorem and beyond. *American Journal of Physics*, 44(7):639–642.

Nousiainen, T. (2009). Optical modeling of mineral dust particles: A review.

Journal of Quantitative Spectroscopy and Radiative Transfer, 110(14-16):1261–1279.

Otto, S., Trautmann, T., and Wendisch, M. (2011). On realistic size equivalence and shape of spheroidal saharan mineral dust particles applied in solar and thermal radiative transfer calculations. *Atmospheric Chemistry and Physics*, 11(9):4469–4490.

Paleari, C. I., Delmonte, B., Andò, S., Garzanti, E., Petit, J. R., and Maggi, V. (2019). Aeolian dust provenance in central east antarctica during the holocene: Environmental constraints from single-grain raman spectroscopy. *Geophysical Research Letters*, 46(16):9968–9979.

Parola, A., Piazza, R., and Degiorgio, V. (2014). Optical extinction, refractive index, and multiple scattering for suspensions of interacting colloidal particles. *The Journal of chemical physics*, 141(12):124902.

Petit, J.-R. and Delmonte, B. (2009). A model for large glacial–interglacial climate-induced changes in dust and sea salt concentrations in deep ice cores (central antarctica): palaeoclimatic implications and prospects for refining ice core chronologies. *Tellus B: Chemical and Physical Meteorology*, 61(5):768–790.

Petit, J.-R., Jouzel, J., Raynaud, D., Barkov, N. I., Barnola, J.-M., Basile, I., Bender, M., Chappellaz, J., Davis, M., Delaygue, G., et al. (1999). Climate and atmospheric history of the past 420,000 years from the vostok ice core, antarctica. *Nature*, 399(6735):429–436.

Philips, L. A., Ruffner, D. B., Cheong, F. C., Blusewicz, J. M., Kasimbeg, P., Waisi, B., McCutcheon, J. R., and Grier, D. G. (2017). Holographic characterization of contaminants in water: Differentiation of suspended particles in heterogeneous dispersions. *Water research*, 122:431–439.

Pöschl, U. (2005). Atmospheric aerosols: composition, transformation, climate and health effects. *Angewandte Chemie International Edition*, 44(46):7520–7540.

Potenza, M., Albani, S., Delmonte, B., Villa, S., Sanvito, T., Paroli, B., Pullia, A., Baccolo, G., Mahowald, N., and Maggi, V. (2016). Shape and size constraints on dust optical properties from the dome c ice core, antarctica. *Scientific reports*, 6(1):1–9.

Potenza, M., Cremonesi, L., Delmonte, B., Sanvito, T., Paroli, B., Pullia, A., Baccolo, G., and Maggi, V. (2017). Single-particle extinction and scattering method allows for detection and characterization of aggregates of aeolian dust grains in ice cores. *ACS Earth and Space Chemistry*, 1(5):261–269.

Potenza, M., Sabareesh, K., Carpineti, M., Alaimo, M., and Giglio, M. (2010). How to measure the optical thickness of scattering particles from the phase delay of scattered waves: application to turbid samples. *Physical review letters*, 105(19):193901.

Prospero, J. M., Ginoux, P., Torres, O., Nicholson, S. E., and Gill, T. E. (2002). Environmental characterization of global sources of atmospheric soil dust identified with the nimbus 7 total ozone mapping spectrometer (toms) absorbing aerosol product. *Reviews of geophysics*, 40(1):2–1.

Pu, Y. and Meng, H. (2003). Intrinsic aberrations due to mie scattering in particle holography. *JOSA A*, 20(10):1920–1932.

Rasmussen, S. O., Bigler, M., Blockley, S. P., Blunier, T., Buchardt, S. L., Clausen, H. B., Cvijanovic, I., Dahl-Jensen, D., Johnsen, S. J., Fischer, H., et al. (2014). A stratigraphic framework for abrupt climatic changes during the last glacial period based on three synchronized greenland ice-core records: refining and extending the intimate event stratigraphy. *Quaternary Science Reviews*, 106:14–28.

Ratcliffe, J. A. (1956). Some aspects of diffraction theory and their application to the ionosphere. *Reports on progress in physics*, 19(1):188.

Rea, D. K. and Hovan, S. A. (1995). Grain size distribution and depositional processes of the mineral component of abyssal sediments: Lessons from the north pacific. *Paleoceanography*, 10(2):251–258.

Redmond, H. E., Dial, K. D., and Thompson, J. E. (2010). Light scattering and absorption by wind blown dust: Theory, measurement, and recent data. *Aeolian Research*, 2(1):5–26.

Ruth, U., Barbante, C., Bigler, M., Delmonte, B., Fischer, H., Gabrielli, P., Gaspari, V., Kaufmann, P., Lambert, F., Maggi, V., et al. (2008). Proxies and measurement techniques for mineral dust in antarctic ice cores. *Environmental science & technology*, 42(15):5675–5681.

Ruth, U., Wagenbach, D., Steffensen, J. P., and Bigler, M. (2003). Continuous record of microparticle concentration and size distribution in the central greenland ngrip ice core during the last glacial period. *Journal of Geophysical Research: Atmospheres*, 108(D3).

Ryder, C. L., Highwood, E. J., Rosenberg, P. D., Trembath, J., Brooke, J. K., Bart, M., Dean, A., Crosier, J., Dorsey, J., Brindley, H., et al. (2013). Optical properties of saharan dust aerosol and contribution from the coarse mode as measured during the fennec 2011 aircraft campaign. *Atmospheric Chemistry*

and Physics, 13(1):303–325.

Schnars, U., Falldorf, C., Watson, J., and Jüptner, W. (2015). Digital holography. In *Digital Holography and Wavefront Sensing*, pages 39–68. Springer.

Schnars, U. and Jüptner, W. (1994). Direct recording of holograms by a ccd target and numerical reconstruction. *Applied optics*, 33(2):179–181.

Schulz, M., Balkanski, Y. J., Guelle, W., and Dulac, F. (1998). Role of aerosol size distribution and source location in a three-dimensional simulation of a saharan dust episode tested against satellite-derived optical thickness. *Journal of Geophysical Research: Atmospheres*, 103(D9):10579–10592.

Seinfeld, J. H. and Pandis, S. N. (2016). *Atmospheric chemistry and physics: from air pollution to climate change*. John Wiley & Sons.

Shao, Y. (2001). A model for mineral dust emission. *Journal of Geophysical Research: Atmospheres*, 106(D17):20239–20254.

Shao, Y., Raupach, M., and Findlater, P. (1993). Effect of saltation bombardment on the entrainment of dust by wind. *Journal of Geophysical Research: Atmospheres*, 98(D7):12719–12726.

Sheng, J., Malkiel, E., and Katz, J. (2006). Digital holographic microscope for measuring three-dimensional particle distributions and motions. *Applied optics*, 45(16):3893–3901.

Simonsen, M. F., Cremonesi, L., Baccolo, G., Bosch, S., Delmonte, B., Erhardt, T., Kjær, H. A., Potenza, M., Svensson, A., and Vallelonga, P. (2018). Particle shape accounts for instrumental discrepancy in ice core dust size distributions. *Climate of the Past*, 14(5):601–608.

Stocker, T. e. (2014). *Climate change 2013: the physical science basis: Working Group I contribution to the Fifth assessment report of the Intergovernmental Panel on Climate Change*. Cambridge University Press.

Stocker, T. F., Qin, D., Plattner, G.-K., Tignor, M., Allen, S. K., Boschung, J., Nauels, A., Xia, Y., Bex, V., Midgley, P. M., et al. (2013). Climate change 2013: The physical science basis. *Contribution of working group I to the fifth assessment report of the intergovernmental panel on climate change*, 1535.

Tegen, I. and Lacis, A. A. (1996). Modeling of particle size distribution and its influence on the radiative properties of mineral dust aerosol. *Journal of Geophysical Research: Atmospheres*, 101(D14):19237–19244.

Tegen, I. and Schepanski, K. (2009). The global distribution of mineral dust.

In *IOP Conference Series: Earth and Environmental Science*, volume 7, page 012001. IOP Publishing.

Tesson, S. V., Skjøth, C. A., Šantl-Temkiv, T., and Löndahl, J. (2016). Airborne microalgae: Insights, opportunities, and challenges. *Appl. Environ. Microbiol.*, 82(7):1978–1991.

Textor, C., Schulz, M., Guibert, S., Kinne, S., Balkanski, Y., Bauer, S., Berntsen, T., Berglen, T., Boucher, O., Chin, M., et al. (2006). Analysis and quantification of the diversities of aerosol life cycles within aerocom. *Atmospheric Chemistry and Physics*, 6(7):1777–1813.

Tsoar, H. and Pye, K. (1987). Dust transport and the question of desert loess formation. *Sedimentology*, 34(1):139–153.

Van de Hulst, H. (1957). *Light scattering by small particles (Courier Corporation)*. Dover Publications, Inc.: New York, NY, USA.

Van de Hulst, H. C. (1981). *Light scattering by small particles*. Courier Corporation.

Vecchi, R., Bernardoni, V., Paganelli, C., and Valli, G. (2014). A filter-based light-absorption measurement with polar photometer: Effects of sampling artefacts from organic carbon. *Journal of Aerosol Science*, 70:15–25.

Villa, S., Sanvito, T., Paroli, B., Pullia, A., Delmonte, B., and Potenza, M. (2016). Measuring shape and size of micrometric particles from the analysis of the forward scattered field. *Journal of Applied Physics*, 119(22):224901.

Vora, P., Trivedi, V., Mahajan, S., Patel, N. R., Joglekar, M., Chhaniwal, V., Moradi, A.-R., Javidi, B., and Anand, A. (2017). Wide field of view common-path lateral-shearing digital holographic interference microscope. *Journal of biomedical optics*, 22(12):126001.

Weidler, P. G. and Friedrich, F. (2007). Determination of the refractive index of particles in the clay and sub-micrometer size range. *American Mineralogist*, 92(7):1130–1132.

Winstrup, M., Vallelonga, P., Kjær, H. A., Fudge, T. J., Lee, J. E., Riis, M. H., Edwards, R., Bertler, N. A., Blunier, T., Brook, E. J., et al. (2019). A 2700-year annual timescale and accumulation history for an ice core from roosevelt island, west antarctica. *Climate of the Past*, 15(2):751–779.

Wiscombe, W. J. (1980). Improved mie scattering algorithms. *Applied optics*, 19(9):1505–1509.

Wolff, E., Barbante, C., Becagli, S., Bigler, M., Boutron, C., Castellano, E., De An-

gelis, M., Federer, U., Fischer, H., Fundel, F., et al. (2010). Changes in environment over the last 800,000 years from chemical analysis of the epica dome c ice core. *Quaternary Science Reviews*, 29(1-2):285–295.

Xu, W., Jericho, M., Meinertzhagen, I., and Kreuzer, H. (2002). Digital in-line holography of microspheres. *Applied optics*, 41(25):5367–5375.

Yang, B., Tang, L., Li, C., Shao, Y., Tao, S., and Yang, L. (2010). An ice-core record of vegetation and climate changes in the central tibetan plateau during the last 550 years. *Chinese Science Bulletin*, 55(12):1169–1177.

Yang, W., Kostinski, A. B., and Shaw, R. A. (2006). Phase signature for particle detection with digital in-line holography. *Optics letters*, 31(10):1399–1401.

Yurkin, M. A. and Hoekstra, A. G. (2011). The discrete-dipole-approximation code adda: capabilities and known limitations. *Journal of Quantitative Spectroscopy and Radiative Transfer*, 112(13):2234–2247.

Zender, C. S., Miller, R., and Tegen, I. (2004). Quantifying mineral dust mass budgets: Terminology, constraints, and current estimates. *Eos, Transactions American Geophysical Union*, 85(48):509–512.

Zhang, T. and Yamaguchi, I. (1998). Three-dimensional microscopy with phase-shifting digital holography. *Optics letters*, 23(15):1221–1223.

Acknowledgements

I would like to acknowledge my advisors, Prof. Marco Potenza and Dr. Barbara Delmonte, for their precious support and advice during these years, but also for their kindness and patience.

My deepest gratitude to all my old and new colleagues Federica, Llorenç, Mirko, and Luca, for their participation in both my personal and work life. Thanks for the volleyball matches, the heel lessons and the coffee @Fabrizia. Special thanks go to my office mate Llorenç for the great effort he has put into our common projects and for the recurring snacks time. His support has been invaluable.

I wish all the best to the EuroCold Lab., special to Claudio, Serena, and Sofia for their contribution to this work and for sharing with me their Coulter data.

Per ultimo ringrazio la mia famiglia, loro che sono tutto per me.